

December 2016

Durability of Mechanically Loaded, Freeze Thawed Concrete Determined By Water Absorption

Brian Daniel Mitchell

University of Wisconsin-Milwaukee

Follow this and additional works at: <https://dc.uwm.edu/etd>

 Part of the [Civil Engineering Commons](#)

Recommended Citation

Mitchell, Brian Daniel, "Durability of Mechanically Loaded, Freeze Thawed Concrete Determined By Water Absorption" (2016).
Theses and Dissertations. 1390.
<https://dc.uwm.edu/etd/1390>

This Thesis is brought to you for free and open access by UWM Digital Commons. It has been accepted for inclusion in Theses and Dissertations by an authorized administrator of UWM Digital Commons. For more information, please contact open-access@uwm.edu.

DURABILITY OF MECHANICALLY LOADED, FREEZE THAWED CONCRETE
DETERMINED BY WATER ABSORPTION

by
Brian Mitchell

A Thesis Submitted in
Partial Fulfillment of the
Requirements for the Degree of

Master of Science
in Engineering

at
The University of Wisconsin-Milwaukee
December 2016

ABSTRACT

DURABILITY OF MECHANICALLY LOADED, FREEZE THAWED CONCRETE DETERMINED BY WATER ABSORPTION

by

Brian Mitchell

The University of Wisconsin-Milwaukee, 2016
Under the Supervision of Dr. Jian Zhao

The design of concrete bridges is primarily focused on strength characteristics. However, it is often the case that durability characteristics, specifically early deterioration of the bridge deck, requires expensive repairs before the designed service life of the bridge can come to term. Lin et al. (2012) identified the development of microcracks as a possible source of this early deterioration. He proposed that these microcracks propagated due to high local compressive stress induced by overweight trucks. The resulting permeability increase caused by the propagation of these microcracks is not significant enough to cause the kind of early deterioration of bridge deck observed in the field. However, the combined effect of mechanical loading and F/T can cause much more severe microcrack development, and thereby, deterioration of concrete.

Currently there are very few efficient ways of measuring the deterioration of concrete bridge decks. Standard tests are available for concrete samples, including ASTM C215 (dynamic modulus), ASTM C1202: Rapid Chloride Ion Penetration (RCIP), and Electrical Surface Resistivity (ESR). Alternatively, water absorption, measured by ASTM C642, can be used to determine the deterioration of concrete. The benefits of using water absorption to measure concrete durability include; relatively quick test periods, and no requirements on sample dimensions; thus, lending itself more to field testing of concrete cores extracted from bridge deck.

There is precedence correlating water absorption to the durability of concrete. Lin et al. (2012) observed that water absorption was directly proportional to the amount of charge passed in RCIP tests. There were several concerns with this study, therefore, the claim that water absorption correlated to the durability of concrete required further validation.

In this study, mechanically loaded, F/T concrete cylinders were subjected to a variety of tests including; dynamic modulus, water absorption, and ESR. An inversely proportional relationship was found between absorption and ESR with a coefficient of determination (R^2) of 63.5%. This strong relationship very clearly provides supporting evidence to help validate the original conclusion proposed by Lin et al. (2012), that water absorption directly relates the durability of concrete.

© Copyright by Brian Mitchell 2016
All Rights Reserved

To

The almighty God, in recognition for your many blessings;

“For in union with Christ you have become rich in all things, including all speech and all knowledge” (Corinthians 1:5);

my Brother, Mother, Father, and Grandmother;

and my Grandparents in Heaven, you all live on in my thoughts and in my actions.

TABLE OF CONTENTS

1.	Introduction.....	1
1.1	Concrete Bridge Deck.....	1
1.2	Deterioration.....	1
1.3	Measuring Deterioration.....	3
1.4	Purpose.....	3
1.5	Objectives:.....	4
1.6	Experimental Program.....	5
1.7	Organization.....	7
2	Literature Review.....	9
2.1	Impact of Overweight Vehicles (With Heavy Axle Loads) On Bridge Deck Deterioration; by Lin et al.....	9
2.1.1	Introduction.....	9
2.1.2	Experimental Program.....	10
2.1.3	RCIP.....	11
2.1.4	Microcracks.....	12
2.1.5	Water Absorption.....	12
2.2	Quantitative Microstructural Investigation of Deteriorated Reinforced Concrete Bridge Deck; by Elzafranay et al.....	16
2.2.1	Introduction.....	16
2.2.2	Experimental Program.....	16
2.2.3	Microscopy.....	17
2.2.4	Results.....	18
2.3	The Effect of Mechanical Stress on Permeability of Concrete: A Review; by Hoseini et al.....	21
2.3.1	Introduction.....	21
2.3.2	Permeability.....	21
2.3.3	Microcracks.....	22
2.3.4	Loading.....	23
2.3.5	Fiber Reinforcement Concrete (FRC).....	24
2.3.6	Conclusion.....	24

2.4	Electrical Resistivity of Concrete; Concepts, Applications, and Measurement Techniques by Layssi et al.	28
2.4.1	Introduction	28
2.4.2	RCIP.....	28
2.4.3	ESR.....	29
2.4.4	Conclusion.....	30
3	Experimental Program	32
3.1	Introduction	32
3.2	Objectives	33
3.3	Specimen Design	33
3.4	Dynamic Modulus.....	34
3.5	Water Absorption.....	37
3.5.1	Oven-Dried State.....	37
3.5.2	Saturated After Immersion State	38
3.5.3	Saturated After Boiling State	38
3.5.4	Immersed Apparent State.....	39
3.6	Electric Resistivity	39
4	Data Analysis	47
4.1	Dynamic Modulus.....	47
4.2	Water Absorption.....	49
4.3	Electric Resistivity	51
5	Conclusion	67
5.1	Summary	67
5.2	Results	68
5.3	Further Research	69
6	References.....	71
7	Appendix.....	72
7.1	ESR Figures	72
7.2	Disk Sample Figures	80

LIST OF FIGURES

Figure 2-1: Overweight vehicle causing visible deflections in bridge (Lin et al., 2012, p. 23).	14
Figure 2-2: Corrected charge passed through samples with various levels	14
Figure 2-3: Lin et al. (2012) summary of experiment results (Lin et al., 2012, p. 55)	15
Figure 2-4: Sub-Regions I, II, and III along with approximate locations of.....	20
Figure 2-5: Details of Test Plan (Elzafrany et al., 2005, p. 161).	20
Figure 2-6: Spatial (3D) measurements for all Sub-Regions	20
Figure 2-7: Effect of load levels on permeability under compression.....	26
Figure 2-8: Relation between water permeability and crack opening	26
Figure 2-9: Effect of stress on the relative permeability of plain concrete	27
Figure 2-10: Effects of applied stress on permeability (Hoseini et al., 2009, p. 217)	27
Figure 2-11: Impedance is a complex number that can be represented as.....	31
Figure 2-12: Relationship between ESR and chloride penetration.....	31
Figure 2-13: Relationship between electrical conductivity and chloride.....	31
Figure 3-1: ASTM C215 Transverse Mode (ASTM C215, p. 3)	41
Figure 3-2: Transverse frequency testing ASTM C215.....	41
Figure 3-3: Oven-dried concrete samples being placed in a stainless-steel container.....	42
Figure 3-4: Designation of each cut number per cylinder.	42
Figure 3-5: Oven-dried concrete samples sitting inside stainless-steel containers.....	43
Figure 3-6: Mass of suspended concrete samples submerged in water per ASTM C642.....	44
Figure 3-7: Schematic view and concept of the test setup (Giatec Scientific, p. 7)	44
Figure 3-8: Surf TM testing apparatus.....	45
Figure 3-9: Relationship between ESR and chloride penetration. (Giatec Scientific, p. 5).....	45
Figure 3-10: Cutting concrete cylinder samples with water-cooled diamond saw.....	46
Figure 3-11: Epoxied samples in preparation for proposed RCIP testing	46
Figure 4-1: Average Peak Frequency (Hz) recorded per sample according to ASTM C215.....	53
Figure 4-2: Dynamic Modulus per concrete cylinder sample calculated per ASTM C215.....	53
Figure 4-3: PV calculated per concrete sample according to ASTM C642.....	54
Figure 4-4: Oven-dried mass (A), saturated mass after immersion (B), saturated mass	54
Figure 4-5: Immersed apparent mass (D) for cylindrical samples.	55
Figure 4-6: Average resistivity of each cylindrical sample calculated per Equation 4-6.	55
Figure 4-7: Holistic comparison between PV results obtained from ASTM C642 for water	56
Figure 4-8: Comparison between PV results obtained from ASTM C642 for water absorption	56
Figure 4-9: Consolidated data comparing PV obtained from ASTM C64,.....	57
Figure 4-10: Consolidated data for comparison of the average surface resistivity and the	57
Figure 7-1: Electric Resistivity of sample C-06.....	72
Figure 7-2: Electric Resistivity of sample C-11	73
Figure 7-3: Electric Resistivity of sample C-14.....	73
Figure 7-4: Electric Resistivity of sample C-15.....	74
Figure 7-5: Electric Resistivity of sample C-16.....	74
Figure 7-6: Electric Resistivity of sample C-17.....	75

Figure 7-7: Electric Resistivity of sample C-21	75
Figure 7-8: Electric Resistivity of sample C-22.....	76
Figure 7-9: Electric Resistivity of sample C-28.....	76
Figure 7-10: Electric Resistivity of sample C-29.....	77
Figure 7-11: Electric Resistivity of sample C-30.....	77
Figure 7-12: Electric Resistivity of sample C-34.....	78
Figure 7-13: Electric Resistivity of sample C-35.....	78
Figure 7-14: Electric Resistivity of sample C-40:.....	79
Figure 7-15: Electric Resistivity of sample C-42.....	79
Figure 7-16: D-1B	80
Figure 7-17: D-2B	81
Figure 7-18: D-3B	81
Figure 7-19: D-4B	82
Figure 7-20: D-5B	82
Figure 7-21: D-6B	83
Figure 7-22: D-7B	83
Figure 7-23: D-8B	84
Figure 7-24: D-9B	84
Figure 7-25: D-1C	85
Figure 7-26: D-2C	85
Figure 7-27: D-3C	86
Figure 7-28: D-4C	86
Figure 7-29: D-5C	87
Figure 7-30: D-6C	87
Figure 7-31: D-7C	88
Figure 7-32: D-8C	88
Figure 7-33: D-9C	89
Figure 7-34: D-1D.....	89
Figure 7-35: D-2D.....	90
Figure 7-36: D-3D.....	90
Figure 7-37: D-4D.....	91
Figure 7-38: D-5D.....	91
Figure 7-39: D-6D.....	92
Figure 7-40: D-7D.....	92
Figure 7-41: D-8D.....	93
Figure 7-42: D-1E	93
Figure 7-43: D-2E	94
Figure 7-44: D-3E	94
Figure 7-45: D-4E	95
Figure 7-46: D-5E	95
Figure 7-47: D-6E	96
Figure 7-48: D-7E	96
Figure 7-49: D-8E	97
Figure 7-50: D-9E	97

Figure 7-51: D-1F.....	98
Figure 7-52: D-2F.....	98
Figure 7-53: D-3F.....	99
Figure 7-54: D-4F.....	99
Figure 7-55: D-5F.....	100
Figure 7-56: D-6F.....	100
Figure 7-57: D-7F.....	101
Figure 7-58: D-8F.....	101
Figure 7-59: D-9F.....	102
Figure 7-60: D-1G.....	102
Figure 7-61: D-2G.....	103
Figure 7-62: D-4G.....	103
Figure 7-63: D-5G.....	104
Figure 7-64: D-6G.....	104
Figure 7-65: D-7G.....	105
Figure 7-66: D-8G.....	105
Figure 7-67: D-9G.....	106
Figure 7-68: D-1H.....	106
Figure 7-69: D-2H.....	107
Figure 7-70: D-3H.....	107
Figure 7-71: D-4H.....	108
Figure 7-72: D-5H.....	108
Figure 7-73: D-6H.....	109
Figure 7-74: D-7H.....	109
Figure 7-75: D-8H.....	110
Figure 7-76: D-9H.....	110
Figure 7-77: D06-1.....	111
Figure 7-78: D06-2.....	111
Figure 7-79: D06-3.....	112
Figure 7-80: D06-4.....	112
Figure 7-81: D11-1.....	113
Figure 7-82: D11-2.....	113
Figure 7-83: D11-3.....	114
Figure 7-84: D11-4.....	114
Figure 7-85: D14-1.....	115
Figure 7-86: D14-2.....	115
Figure 7-87: D14-3.....	116
Figure 7-88: D14-4.....	116
Figure 7-89: D15-1.....	117
Figure 7-90: D15-2.....	117
Figure 7-91: D15-3.....	118
Figure 7-92: D15-4.....	118
Figure 7-93: D16-1.....	119
Figure 7-94: D16-2.....	119

Figure 7-95: D16-3	120
Figure 7-96: D16-4	120
Figure 7-97: D17-1	121
Figure 7-98: D17-2	121
Figure 7-99: D17-3	122
Figure 7-100: D17-4	122
Figure 7-101: D21-1	123
Figure 7-102: D21-2	123
Figure 7-103: D21-3	124
Figure 7-104: D21-4	124
Figure 7-105: D22-1	125
Figure 7-106: D22-2	125
Figure 7-107: D22-3	126
Figure 7-108: D22-4	126
Figure 7-109: D28-1	127
Figure 7-110: D28-2	127
Figure 7-111: D28-3	128
Figure 7-112: D28-4	128
Figure 7-113: D29-1	129
Figure 7-114: D29-2	129
Figure 7-115: D29-3	130
Figure 7-116: D29-4	130
Figure 7-117: D30-1	131
Figure 7-118: D30-2	131
Figure 7-119: D30-3	132
Figure 7-120: D30-4	132
Figure 7-121: D34-1	133
Figure 7-122: D34-2	133
Figure 7-123: D34-3	134
Figure 7-124: D35-1	134
Figure 7-125: D35-2	135
Figure 7-126: D35-3	135
Figure 7-127: D35-4	136
Figure 7-128: D40-1	136
Figure 7-129: D40-2	137
Figure 7-130: D40-3	137
Figure 7-131: D40-4	138
Figure 7-132: D42-1	138
Figure 7-133: D42-2	139
Figure 7-134: D42-3	139
Figure 7-135: D42-4	140

LIST OF TABLES

Table 4-1: Holistic data for dynamic modulus results obtained from ASTM C215.....	58
Table 4-2: Consolidated data for dynamic modulus results obtained from ASTM C215.....	58
Table 4-3: Results for the cylinders tested per ASTM C642; Standard Test.....	59
Table 4-4: Results for the cylinders tested per ASTM C642; Standard Test Method for.....	59
Table 4-5: Results for the disks tested per ASTM C642; Standard Test Method for Density,	61
Table 4-6: Result for the disks tested per ASTM C642; Standard Test Method for Density,.....	64
Table 4-7: Results of the Surf TM testing. Average ESR (KΩ/cm), average surface	64

LIST OF ABBREVIATIONS

ACI	American Concrete Institute
CFIRE	National Center for Freight & Infrastructure Research & Education
COD	Crack Opening Displacement
ESEM	Environmental scanning electron microscopy
ESR	Electrical Surface Resistivity
FA	Fly Ash
FRC	Fiber Reinforced Concrete
F/T	Freeze Thaw
HSC	High Strength Concrete
ITZ	Interfacial Transition Zone
NWC	Normal Weight Concrete
PV	Percent Volume of Permeable Voids
R ²	Coefficient of Determination
RCIP	Rapid Chloride Ion Penetration
SCM	Scanning Electronic Microscopic
WisDOT	Wisconsin Department of Transportation

ACKNOWLEDGEMENTS

In recognition of your unwavering support, guidance, generous financial contributions, and outstanding character, the author would like to extend his deepest gratitude to Dr. Jian Zhao.

Thank you to the University of Wisconsin Milwaukee Department of Civil Engineering for their generous financial support.

Thank you to the University of Wisconsin Milwaukee American Society of Civil Engineers (UWM-ASCE), especially to Brady Mathisen, Paul Schindelholz, Alyssa Walker and Joseph Behmke, for your assistance, donated materials, and equipment.

Thank you to John Condon and all the others at the UWM Machine Shop for donating materials and aiding in the fabrication of necessary testing equipment.

Special thanks to (arranged alphabetically by last name):

- Baghdassar Ayedian for inspiration, guidance, and encouragement.
- Dr. Benjamin Church for allowing access to your lab space and equipment.
- Zeqian Li for your friendship and many hours of assistance in the lab.
- Dr. Lin for sharing his test information and concrete samples.
- Dr. Yue Liu for providing financial support by honoring me with a Teaching Assistant position under his tutelage.
- Dr. Konstantin Sobolev for allowing access to the concrete lab, dynamic modulus testing equipment and the electric surface resistivity testing equipment.
- Dr. Habib Tabatabaia for allowing access to your lab space and equipment.

- Dr. Hani Titi for allowing access to your lab space and to the RCIP testing equipment.
- All University of Wisconsin Milwaukee staff, especially Clayton Cloutier, Tina Current, Mahmoud Dakwar, Azam Nabizade Darabi, Jennie Klumpp, Marina Kozhukhova, Peng Li, Hua Liu, Chantele Mallett, Asadollah Khoddam Mohammadi, Brett Peters, Rahim Reshadi, Shirley Sondej, Elisabeth Warras, Saeed Yazdani, Lin Yin, and for all of those not mentioned, thank you so much for your support, patience, and cooperation.

1. Introduction

1.1 Concrete Bridge Deck

The design of concrete bridges is primarily focused on strength characteristics. However, it is often the case that durability characteristics, specifically early deterioration of the bridge deck, requires expensive repairs before the designed service life of the bridge can come to term. In fact, a large number of bridges are afflicted by early deterioration of bridge deck (Elzafraney et al., 2005, p. 159). Lin et al. (2012) identified the development of microcracks as a possible source of this early deterioration. He proposed that these microcracks propagated due to high local compressive stress induced by overweight trucks. This idea, however, has not yet been generally accepted. Currently, overweight trucks are permitted on U.S. highways and bridges. For the state of Wisconsin, for example, such vehicles are allowed if the overweight trucks follow a designated route and apply for a permit with varying costs allocated by weight. The permit fee can be as small as \$20 for overweight vehicles weighing 0 through 90,000 pounds, or as high as \$84 plus \$10 for each additional 10,000 pounds for overweight vehicles weighing 150,001 pounds or more (WisDOT, 2005, p. 1). Overweight trucks, such as the one seen in Figure 2-1, can cause visible deflections within the bridge superstructure. Surely, such a large deflection must have some sort of deleterious effects on the concrete.

1.2 Deterioration

Through finite element analysis, Lin et al. (2012) determined that the local compressive stresses caused by simulated overweight trucks increased to as much as $0.4f'_c$. For concrete under uniaxial compression, stress levels between 0.3 through 0.5 percent of f'_c are high enough to cause extension of microcracks in the interfacial transition zone (ITZ) (Mehta et al., 2006, p. 68). It is

known that the ITZ contributes to the permeability of concrete, however, with the onset of microcrack development, this contribution becomes even greater. The permeability of concrete is a concern because for most of the mechanisms responsible for the degradation of concrete (e.g. corrosion of reinforcing steel, cracking due to shrinkage, F/T, scaling, and chemical attack) water is either the primary cause or the primary medium by which aggressive agents (such as chloride or sulfate ions) are transported into the concrete (Yang et al., 2006, p. 424) (Mehta et al., 2006, p. 121). The increase in permeability, due to the propagation of microcracks resulting from compressive stresses ranging from 0.3 to 0.5 percent of $f'c$, is not significant enough to cause the kind of early deterioration of bridge deck observed in the field. However, the combined effect of mechanical loading and F/T can cause much more severe microcrack development, and thereby, deterioration of concrete. As temperature decreases, ice crystals (formed from free water in the voids of saturated concrete) start to expand within the pore network increasing hydraulic pressure (Lin et al., 2012, p. 2). After repeated cycles of F/T this pressure increase further opens and propagates microcracks leading to increased connectivity of the pore network. These microcracks serve as an avenue and facilitate transport of liquids and other aggressive chemicals such as chloride ions which lead to deterioration.

There have been numerous studies involving several deleterious mechanisms on the durability of concrete bridge deck; (ElSafty et al., 2013, p. 79); Arezoumandi (2015); (Rhee et al., 2009, p. 2)); (Shiotani et al., 2012); and Ishida, 2016 (2016). However, very few evaluate the damage to bridge deck caused by the combined effect of compressive stresses and F/T damage.

1.3 Measuring Deterioration

Currently there are very few efficient ways of measuring the deterioration of concrete bridge decks. Standard tests are available for concrete samples, including ASTM C215: Fundamental Transverse, Longitudinal, and Torsional Resonant Frequencies of Concrete Specimens (dynamic modulus); ASTM C1202 (RCIP); and ESR which can be used to measure the deterioration of concrete. However, a couple of these, namely RCIP and ESR, are not without disadvantages. The former requires at least 29 hours, between conditioning and testing, and causes permanent damage to the concrete microstructure (ASTM C1202, p.5). The later requires cylindrical concrete specimens that are 4" x 8". Therefore, testing of field specimen would be very difficult due to complication arising from coring a specimen from bridge deck that perfectly matches these dimensions (often the end will fracture). Additionally, the sample cannot contain any reinforcement as this would alter the results of the test. Alternatively, water absorption measured by ASTM C642: Density, Absorption, and Voids in Hardened Concrete, can be used to determine the deterioration of concrete. The benefits of using ASTM C642 to measure concrete durability include; relatively quick test periods, and no requirements on sample dimensions; thus, lending itself more to field testing of concrete cores extracted from bridge deck.

1.4 Purpose

There is precedence correlating water absorption to the durability of concrete. Lin et al. (2012) observed that water absorption was directly proportional to the amount of charge passed in RCIP tests (as measured by ASTM C1202). This relationship can be seen illustrated in Figure 2-2. In this study the combined effects of mechanical loading and F/T was evaluated on fifteen 4" x 8" concrete cylinders. The cylinders were subjected mechanical compressive stresses at various

percentages of $f'c$ and subsequently to various numbers of F/T cycles. However, there was some concerns identified with this study. One of the disagreements was that dynamic modulus, a known method for determining the degradation of concrete, was never measured. Another criticism was that the correlation between water absorption and concrete durability should have been further reinforced by comparing the results from a variety of well-establish tests that measure concrete durability, not just RCIP. Lastly, there was concern that water absorption was not measured per ASTM standards. Hence, for all the aforementioned concerns, the claim that water absorption correlates to the durability of concrete requires further validation.

1.5 Objectives:

The intent of this current study is to reevaluate water absorption as it relates to concrete durability. By adhering more closely to ASTM standards for testing and by including other concrete durability tests, the author hopes to substantiate the claim made by Lin et al. (2012). The claim that water absorption (ASTM C642) may be used as a more effective testing method to determine the durability of concrete. The objectives of this study are to;

1. Examine the conclusion of the previous study that water absorption is effective for testing concrete durability by showing it directly correlates with electric resistivity and dynamic modulus.
2. Lay a foundation for validating the relationship between water absorption and the durability of concrete, especially the concrete in bridge decks that are subjected to combined mechanical loading and F/T cycles.
3. Provide equations for others to check their own results of absorption for mechanically loaded F/T concrete.

4. Provide an array of water absorption test results for 2"x4" concrete disks to be compared with subsequently proposed ASTM C1202: RCIP testing on the same specimen.

1.6 Experimental Program

From the study by Lin et al. (2012) there remained fifteen 4" x 8" concrete cylinders. In the previous study, these cylinders were subjected to compressive stresses of varying percentages of $f'c$ along with varying numbers of F/T cycles. The specific stress and number of F/T cycles per sample is unknown and the study is therefore blind. The type of concrete used is the same for all the cylinders thus providing the control for the experiment. The benefit of having the test arranged in such a way is that there will be no bias when analyzing the results.

The cylinders were first tested for dynamic modulus using the contact driven forced resonance method (ASTM C215, p.1). The cylinders sat on top of soft rubber pads such that they were allowed to vibrate freely. A driving unit was placed halfway down the concrete specimen (longitudinally). An accelerometer was placed at the end of the specimen rotated 90° such that it was transverse to the driving unit. Vibrations from the driving unit were sent through the specimen at frequencies ranging from 1k through 10k hertz. The dynamic modulus was calculated using the peak frequency at which the cylinders resonated, as measured by the accelerometer, and indicated by the highest reading from a needle indicator.

The concrete specimens were tested for absorption per ASTM 642. The cylinders were oven-dried for a period of 24 hours. They were taken out of the oven and allowed to cool by natural heat loss to 25°C (77°F). The mass of the cylinders was recorded as the oven-dried mass (A). The process was repeated until successive values of A did not exceed 0.5% of the lesser value (ASTM C642, p.1). The cylinders were soaked in water for a period of 48 hours. The surface of each

sample was dried with paper towels to achieve a saturated surface dried state and the mass after immersion (B) was recorded. This process was repeated until successive values of B did not exceed 0.5% of the greater value. The cylinders were then boiled for five hours and subsequently cooled for no less than fourteen hours. The saturated after boiling mass (C) was recorded. The samples were placed in a metal basket suspended in water by a chain secured around the top plate of a scale. The mass of the samples was recorded as the immersed apparent mass (D). The percent volume of permeable voids (PV) was determined from the bulk-dry density and the apparent density as calculated by equations 10 and 13, respectively (ASTM C642, p.2). PV is the value considered to be the measure of absorption for the samples. Linear regression analysis was used to determine the relationship of each mass recorded at each saturation state (e.g. A, B, C, D) to the resulting PV and to determine general best fit equations. Others (doing similar research) may find the equations and figures from this analysis useful for checking the results of their own work. A degree of caution should be exercised, however, since the regression analysis was generated using a small number of samples.

The ESR of the concrete samples was determined using a SURFTM testing apparatus which consisted of a chamber and data acquisition system. Conductive gel was applied to the ends of the sixteen probes fitted around the circumference of the chamber in sets of four. The concrete cylinders, which were in a saturated surface dried condition, were placed inside the testing chamber. The data acquisition system was used to determine the electric surface resistance of the samples. The average surface resistivity was calculated by taking the average of 24 surface resistance measurements and multiplying by a geometrical factor.

The concrete cylinders were cut into four sections using a water-cooled diamond cutting saw. The cut number for each created disk is designated as seen in Figure 3-4. The 60 cut concrete

disks, along with 62 additional disks remaining from the previous study by Lin et al. (2012), were tested for absorption. The generated data will be compared to the results of subsequently proposed ASTM C1202: RCIP testing (which will utilize the same samples).

The results generated from the dynamic modulus, water absorption and ESR tests, using the cylinder samples, were compared and analyzed. When comparing ESR and absorption to dynamic modulus, no clear relationship could be determined. The distribution of dynamic modulus was rather scattered, as such is commonly observed from previous literature. However, an inversely proportional relationship was determined between absorption and ESR with R^2 equal to 63.5%. This strong relationship very clearly provides supporting evidence to help validate the original conclusion proposed by Lin et al. (2012) that water absorption directly relates the durability of concrete. This author hopes that water absorption can be used to measure the extent of damage caused to bridge deck from overweight vehicles. If the severity of damage is more well-known, hopefully some sort of policy change will be enacted.

It should be noted that the results generated for the cylindrical sample presented in this study should be met with a degree of caution due to the limited number of samples.

1.7 Organization

A brief literature review covering such topics as; the deterioration of bridge deck due to overweight vehicles; the analysis on the permeability of a bridge regarding macro and microcracks; the effect of load type and time of application on the permeability of concrete; and electrical surface resistivity of concrete relating to durability; is provided in Chapter 2. The experimental program including, concrete samples tested, and detailed descriptions of each test conducted, is outlined in Chapter 3. Chapter 4 contains data obtained from each test, along with tables and figures

which analyze said data. Chapter 5; briefly reaffirms the purpose and objectives of the study; presents all major conclusions; and indicates further research that could be pursued by others. Chapter 7, the appendix, displays raw data collected during testing along with pictures of each disk sample.

2 Literature Review

2.1 Impact of Overweight Vehicles (With Heavy Axle Loads) On Bridge Deck Deterioration; by Lin et al.

2.1.1 Introduction

The impact of combined F/T and mechanical loading on the durability of concrete was evaluated in a recent study by Lin et al. (2012). To evaluate the effects of this combined action air-entrained concrete cylinders were cast which consisted of “eight groups of three 100x200mm (4”x8”) cylinders” (Lin et al., 2012, vii). The cylinders were subjected to compressive stresses equal to 40 through 80 percent of the measured 28-day compressive strength (Lin et al., 2012, vii). After being subjected to varying compressive loads, the cylinders were exposed to 300 F/T cycles following a procedure similar to ASTM C666 (Lin et al., 2012, vii). Because “concrete durability is closely related to its water and chloride permeability (Lin et al., 2012, p. 9), the chloride permeability of the samples was evaluated using ASTM 1202. The study found that there was a strong correlation between water absorption and RCIP. However, the water absorption tests which had been conducted for the study, did not follow ASTM C642. Therefore, the conclusion that water absorption tests (ASTM C642) can provide similar results regarding the deterioration of concrete under combined mechanical loading and F/T cycles needs further verification.

Only compressive stresses induced by overweight truck loads were considered since the impact of tensile stresses has been studied extensively in literature. This work differs from others in literature because it looks at the effects of combined mechanical loading and F/T action on the deterioration of concrete. Furthermore, unlike other studies which focus on permeability increase resulting from one or more macrocracks, this study looks at an increase in permeability as a result of several distributed microcracks.

2.1.2 Experimental Program

In this study, Wisconsin Department of Transportation (WisDOT) specified air entrained Grade A-FA concrete was tested (Lin et al., 2012, p. 44). The water to cement ratio (w/c) was 0.4 and the amount of fly ash (FA) was 30 percent by weight of cement (Lin et al., 2012, p. 25). The proportion of total cementitious material to coarse and fine aggregate was 1:3.55 and 1:1.9 by weight, respectively (Lin et al., 2012, p. 52). ASTM standard tests C143 and C231 were used to measure the fresh concrete properties of the concrete mixture. Using ASTM C231 the air content of the fresh concrete was found to be 7.8%. The slump, measured according to ASTM 143, was found to be 6 in. (Lin et al., 2012, p. 25). After 28 days of curing in saturated lime water, the compressive strength was measured to be 27.1 MPa (3931 psi). At 120 days the compressive strength was found to be 38.7 MPa (5600 psi) which demonstrates the later strength development of concrete mixtures incorporating fly ash (Lin et al., 2012, p. 45).

A total of twenty-four cylinders were cast and divided into eight groups of three cylinders. Of these cylinders, three were kept in air after 28 days of curing in saturated lime water. Samples cut from these cylinders were designated RNW (Lin et al., 2012, p. 25). Another group of three cylinders, designated as RW, were kept in water after 28 days. This was done to measure the effects that extended curing would have on the remaining cylinders. The rest of the cylinders, designated RD, had additional curing time since the hydration process would have continued while the cylinders were fully saturated for F/T testing (Lin et al., 2012, p. 25). To serve as a reference, all but three of the RD cylinders were subjected to predetermine varying compressive loads. All of the RD samples were exposed to 300 F/T cycles (Lin et al., 2012, p. 25). The compressive loads ranged from “40 through 80 percent of the measured ultimate compressive load” (Lin et al., 2012, p. 45).

It should be noted that 80 percent of the measured ultimate compressive load may seem high at first. However, the study was measuring the effects of compressive loads resulting from overweight vehicles on bridge deck. In such a case, the design for loading “assumes that the concrete is loaded beyond the strain corresponding to the peak stress (f'_c)” (Lin et al., 2012, p. 45). The study did not consider one important aspect of deck deterioration – the repeated truck loading.

2.1.3 RCIP

The effects of combined mechanical and F/T action were measured by rapid chloride ion penetration. Two 50 mm (2 in.) thick samples were sliced from the interior of the concrete cylinders (Lin et al., 2012, vii). Samples sliced from the RW and RNW cylinders, those not subjected to loads and F/T cycles, were also tested to serve as a reference (Lin et al., 2012, vii). Results indicated that the “chloride permeability of the concrete samples increased significantly with an increase in the applied compressive loads” (Lin et al., 2012, vii). The highest increase in average passing charge, 55%, could be seen between the D60 and the RD samples. When comparing to the reference samples, the highest increase of 93% could be observed between the D50 and RNW samples (Lin et al., 2012, vii). When comparing the results obtained from RCIP and absorption, an interesting correlation emerged. “A strong relationship was identified between the chloride permeability and the water absorption” (Lin et al., 2012, vii), both of which are highly influenced by the propagation of microcracks. It should be noted that the measurement of water absorption in this study did not completely follow the related ASTM standards; hence the conclusion may need to be further verified.

2.1.4 Microcracks

The authors made a hypothesis that the principal mechanism responsible for the observed increase in chloride permeability was the propagation of microcracks (Lin et al., 2012, vii). Higher compressive loads caused more extensive microcrack networks facilitating transport (Lin et al., 2012, vii). “These passageways were further opened and interconnected during the F/T cycles due to an increase in hydraulic pressure” (Lin et al., 2012, vii). The formation and expansion of ice crystals within the void space of the concrete was responsible for the increase in hydraulic pressure (Lin et al., 2012, vii).

The hypothesis that microcrack facilitated an increase in chloride permeability “was confirmed by the scanning electronic microscopic (SEM) images of the loaded and unloaded specimens” (Lin et al., 2012, vii). Images revealed the through-thickness microcracks which facilitated the transit of chloride ions in the loaded specimen (Lin et al., 2012, vii). For example, the SEM images for sample D40 displayed through cracks which acted as passageways for chloride ions (Lin et al., 2012, p. 127). “As a result, the average value of charge passed allowed by D40 samples had an increase of 10 percent compared with RD samples” (Lin et al., 2012, p. 127).

2.1.5 Water Absorption

In this study water absorption was used to indirectly measure the amount of microcracks and air voids present within the concrete (Lin et al., 2012, p. 209). In general, the water absorption of the concrete specimen increased with an increase in the applied load (Lin et al., 2012, p. 129). A great example of this can be seen with the RW specimens, which were cured in water. These samples had the least water absorption which corresponds to their low charge passed in RCPT (Lin

et al., 2012, p. 129). Unlike the microstructure of the RW samples, the RNW samples, which were cured in air, were not able to develop such as dense of a microstructure. The water absorption of RNW specimens was high corresponding to increased charge passed (when compared with RW specimens) (Lin et al., 2012, p. 129).

While measuring the water absorption, “a strong relationship was identified between the chloride permeability and the water absorption (Lin et al., 2012, vii). This relationship between the measured passing charge and the measured water absorption can be seen from the linear trendline in Figure 2-2 (Lin et al., 2012, p. 129). Therefore, the study proposed that water absorption could be used as a viable alternative to determining the durability of concrete (Lin et al., 2012, p. 190), especially for concrete samples obtained from the field to evaluate the bridge deck conditions.



Figure 2-1: Overweight vehicle causing visible deflections in bridge (Lin et al., 2012, p. 23).

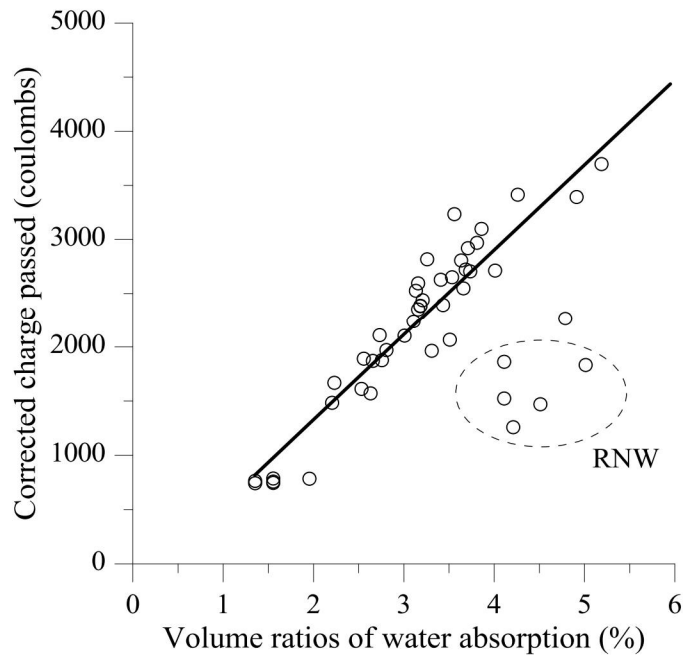


Figure 2-2: Corrected charge passed through samples with various levels of microcracks (Lin et al., 2012, p. 126)

Test No.	Preloading ⁺ (MPa)	F/T		Water absorption	Charge passed in RCPT (coulombs)	
		F/T (cycles)	Weight loss (%)	Volume ratio (%)	Charge passed	Average charge passed ⁺⁺
RW-1	0	0	-	1.4	698	714.83 (5%)
RW-2				1.6	772	
RW-3				1.6	710	
RW-4				1.4	664	
RW-5				1.6	746	
RW-6				2.0	699	
RNW-1	0	0	-	4.5	1528	1629.17 (15%)
RNW-2				4.2	1293	
RNW-3				2.2	1464	
RNW-4				4.1	1625	
RNW-5				4.1	2021	
RNW-6				5.0	1844	
RD-1	0	300	0.25	3.0	2183	2030.80 (11%)
RD-2				2.7	2085	
RD-3			0.18	2.8	2100	
RD-4				3.5	2193	
RD-5			0.25	2.6	1593	
RD-6				-	-	
D40-1	10.9	300	0.08	2.5	1652	2232.33 (21%)
D40-2				2.2	1718	
D40-3	10.9		0.23	2.7	2309	
D40-4				2.6	2077	
D40-5	10.8		0.13	3.2	2856	
D40-6				3.4	2782	
D50-1	13.7	300	0.72	3.5	2804	2757.67 (25%)
D50-2				3.2	2401	
D50-3	13.7		1.01	4.8	2531	
D50-4				4.9	4197	
D50-5	13.6		0.42	3.2	2585	
D50-6				2.8	2028	
D60-1	16.2	300	1.23	3.1	2526	2842.33 (18%)
D60-2				3.7	3086	
D60-3	16.4		0.63	3.2	2391	
D60-4				3.1	2377	
D60-5	16.3		0.35	4.0	2848	
D60-6				3.6	3826	
D70-1	18.9	300	0.30	3.4	2581	3138.17 (25%)
D70-2				3.7	2970	
D70-3	19.0		0.33	5.2	4532	
D70-4				3.9	3612	
D70-5	19.0		1.89	3.3	2051	
D70-6				3.3	3083	
D80-1	21.7	300	0.56	4.3	3872	3044.33 (13%)
D80-2				3.8	3076	
D80-3	21.9		1.25	3.7	2743	
D80-4				3.7	2830	
D80-5	21.8		0.52	3.2	2631	
D80-6				3.6	3114	

Figure 2-3: Lin et al. (2012) summary of experiment results (Lin et al., 2012, p. 55)

2.2 Quantitative Microstructural Investigation of Deteriorated Reinforced Concrete Bridge Deck; by Elzafraney et al.

2.2.1 Introduction

The microstructure of an existing bridge over I-94 at exit 121 in Albion, Michigan was evaluated (Elzafraney et al., 2005, p. 159). At the time of the study the bridge was only 25 years old but was already showing signs of deterioration (Elzafraney et al., 2005, p. 159). This four-lane bridge, two in each direction, had “two internal supports and two abutments” (Elzafraney et al., 2005, p. 160). The concrete deck depth was 22.5 cm (9 in.) thick (Elzafraney et al., 2005, p. 160). Visual inspection of the bridge deck revealed close to 50 visible cracks with “widths that ranged from 10 to 20 mm (3/8-3/4 in.)” (Elzafraney et al., 2005, p. 160).

The bridge was divided up into three sections based on the visual deterioration (Elzafraney et al., 2005, p. 159). A total of 32 cores, 12.5 cm (5 in.) tall and 10 cm (4 in.) in diameter, were extracted from the bridge deck sections (Elzafraney et al., 2005, p. 160). Eighteen samples were tested for compressing (ASTM C39), splitting tension (ASTM C96), and chloride permeability (ASTM C1202) (Elzafraney et al., 2005, p. 160). Fifteen samples were used to analyze the microstructure of the concrete through images obtained by environmental scanning electron microscopy (ESEM) (Elzafraney et al., 2005, p. 161).

2.2.2 Experimental Program

The study began by dividing the bridge up into three sections based off of obvious visual difference in damage conditions” (Elzafraney et al., 2005, p. 159). These sections, ranging from most to least damaged, were Sub-Region I, Sub-Region II, and Sub-Region III, respectively. “A total of 32 cores of 10 cm (4 in.) diameter were extracted from the bridge deck (Elzafraney et al.,

2005, p. 160). Fourteen of the samples were taken from Sub-Region I; eleven from Sub-Region II; and seven from Sub-Region III (Elzafraney et al., 2005, p. 160). The cored samples were only 12.5 cm (5 in.) tall “in order to avoid any risk of cores falling through onto oncoming traffic below (Elzafraney et al., 2005, p. 160). For this reason, a more convenient way to evaluate the durability of field sample may be necessary, such as the water absorption tests proposed by Lin et al. (2012). A diagram displaying the approximate location of each sample, along with the Sub-Region and visible cracks can be seen in Figure 2-4.

Eighteen of the samples were tested for “compression (ASTM C39), splitting tension (ASTM C96), and permeability (ASTM C1202)” (Elzafraney et al., 2005, p. 161). Fifteen of the samples were set aside to analyze the microstructure of the concrete. These fifteen concrete cores were cut in two using a wet diamond concrete saw (Elzafraney et al., 2005, p. 161). One cut was made parallel to, and the other was cut perpendicular to the applied traffic load (Elzafraney et al., 2005, p. 161). These sections were further cut down to “75 mm x75 mm x 50 mm (3 in. x 3 in. x 2 in.) samples” so that the microstructure of the concrete could be analyzed using images obtained through environmental scanning electron microscopy (ESEM) (Elzafraney et al., 2005, p. 161). The test plan is further explained by Figure 2-5.

2.2.3 Microscopy

The cut sections were prepared through Wood’s metal impregnation to provided good contrast between microcracks and the body of concrete” (Elzafraney et al., 2005, p. 161). A total of 4,320 images were captured at a magnification of 125X to analyze the microstructure of the concrete (Elzafraney et al., 2005, p. 162). Qmac™ analysis software was used to automate the process of capturing images, processing data, and analyzing the images (Elzafraney et al., 2005,

p. 162). From this software, quantitative planar (2D) and spatial (3D) information on microcrack system was developed (Elzafraney et al., 2005, p. 162). The (2D) microcrack characteristics determined were “ length per unit area, perimeter per unit area, width per unit area, area fraction, spacing, tortuosity, angle of orientation, and degree of orientation” (Elzafraney et al., 2005, p. 162). The (3D) microcrack characteristics determined were “specific surface area, width, volume fraction, spacing, tortuosity, and degree of orientation” (Elzafraney et al., 2005, p. 162). The results for the spatial (3D) test parameters can be seen in Figure 2-6.

2.2.4 Results

It was found that there was a significant difference in the microstructure of concrete cores taken near or over visible cracks compared to cores taken far from cracks (Elzafraney et al., 2005, p. 164). These differences could be seen “in terms of microcrack length per unit area and area fraction” (Elzafraney et al., 2005, p. 164). This provided supporting evidence regarding the coalescence of microcracks leading to the formation of macrocracks near visible cracks (Elzafraney et al., 2005, p. 164). In fact, the spatial (3D) results were in general agreement with the planar (2D) measurements. This lends itself to the conclusion that “there is a direct relationship between visible damage (macrocracks) and internal damage (microcracks)” (Elzafraney et al., 2005, p. 167).

This study found that the mechanical properties of the concrete (compression and tensile splitting strengths) did not vary between visually determinable Sub-Regions (Elzafraney et al., 2005, p. 162). The permeability, however, was significantly different from one region to the next (Elzafraney et al., 2005, p. 162). It was found that permeability was “higher for Sub-Region I (severe level of damage) and lower for Sub-Region II (moderate level of damage) and Sub-Region

III” (low level of damage) (Elzafraney et al., 2005, p. 162). “The high permeability of Sub-Region I reflects the severe microcracking in this Sub-Region” (Elzafraney et al., 2005, p. 162). In fact, an increased in microcrack intensity was found to be “correlated with increased permeability values. This suggests that permeability is more sensitive to internal damage (microcracks) than mechanical strength. Thus, permeability tests provide more insights into concrete quality and health condition than is possible by only mechanical tests.” (Elzafraney et al., 2005, p. 167).

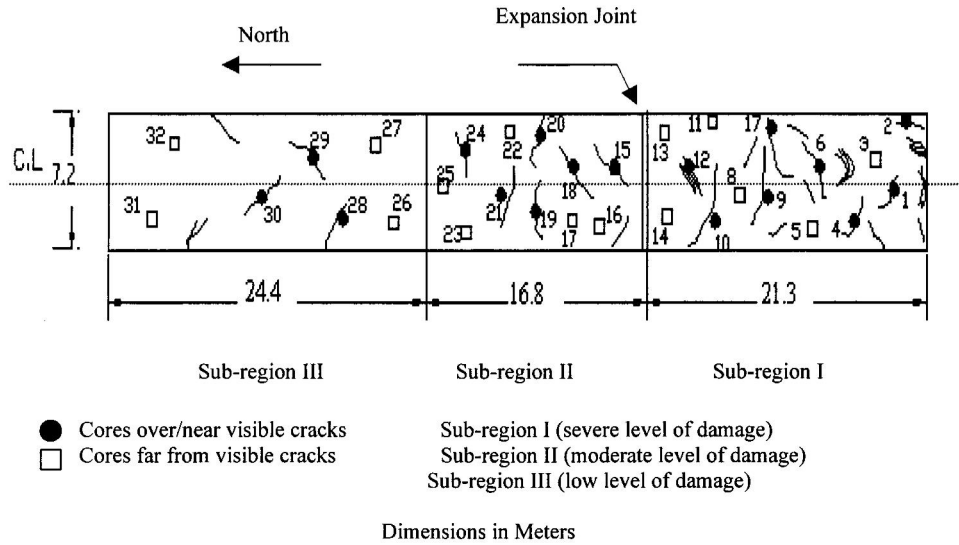


Figure 2-4: Sub-Regions I, II, and III along with approximate locations of samples cored and visible cracks (Elzafraney et al., 2005, p. 161).

Subregion number	Tests			
	Compression	Splitting tension	Permeability	Microstructural investigation
I	Core numbers 5 ^b and 12 ^a	Core numbers 3 ^b and 7 ^a	Core numbers 2 ^a , 10 ^a , and 11 ^b	Core numbers 1 ^a , 4 ^a , 6 ^a , 8 ^b , 9 ^a , 13 ^b , and 14 ^b
II	Core numbers 20 ^a and 25 ^b	Core numbers 17 ^b and 19 ^a	Core numbers 21 ^a and 23 ^b	Core numbers 15 ^a , 16 ^b , 18 ^a , 22 ^b , and 24 ^b
III	Core number 30 ^a	Core number 31 ^b	Core numbers 27 ^b and 29 ^a	Core numbers 26 ^b , 28 ^b , and 32 ^b

^aCores over/near visible cracks.

^bCores far from visible cracks.

Figure 2-5: Details of Test Plan (Elzafraney et al., 2005, p. 161).

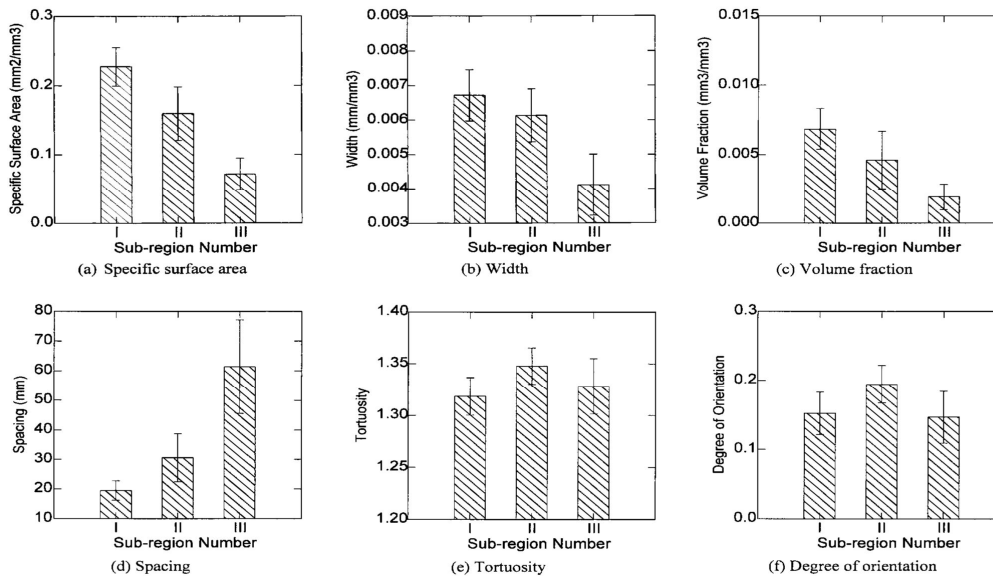


Figure 2-6: Spatial (3D) measurements for all Sub-Regions (means and standard errors): (a) specific surface area, (b) width, (c) volume fraction, (d) spacing, (e) tortuosity, and (f) degree of orientations (Elzafraney et al., 2005, p. 165).

2.3 The Effect of Mechanical Stress on Permeability of Concrete: A Review; by Hoseini et al.

2.3.1 Introduction

Hoseini et al. presented a culmination of several different studies relating to the permeability of concrete. The study looked at the “effect of loading type, crack dimensions, admixtures, and fiber reinforcement on the permeability of fluids in concrete under stress” (Hoseini et al., 2009, p. 213). Only induced stress, which was a result of the “direct application of mechanical loading,” was considered (Hoseini et al., 2009, p. 213). Other stresses, such as that resulting from shrinkage, thermal and creep effects, were outside the scope of the study (Hoseini et al., 2009, p. 213).

One of the principle motifs of this study was that loading, whether it be monotonic, cyclic, administered prior, or administered after, has a big impact on the measured permeability and by extension durability of the concrete. Furthermore, this study points out that it is not the immediate service loads that are of concern (Hoseini et al., 2009, p. 213). Instead, it is the long term loads which cause degradation of concrete by promoting the propagation and coalescence of microcracks (Hoseini et al., 2009, p. 213). This increases the interconnectivity of the pore network which facilitates ingress of liquids and chloride ions (Hoseini et al., 2009, p. 213).

2.3.2 Permeability

Permeability can be described as “the transport mechanism by bulk flow within a porous medium” (Hoseini et al., 2009, p. 214). The permeability of concrete is closely tied to the durability of concrete. Therefore, the properties of concrete are largely dependent upon “the number size and distribution of pores in the cement paste, the aggregates and the resultant interface” (Hoseini et al., 2009, p. 213). In this study the permeability of concrete was evaluated according to load

configuration (compression, tension, flexure) and the instance of permeability (measured under the application of a load or without).

2.3.3 Microcracks

Microcracks have a significant effect on the permeability of concrete. The propagation and coalescence of microcracks leads to a more developed and interconnected pore network, thus increasing permeability (Hoseini et al., 2009, p. 213). Studies have shown that for compressive loading less than 30% of ultimate, cracks are generally restricted to the aggregate-paste interface or the ITZ (Hoseini et al., 2009, p. 214). This results in little increase in permeability (Hoseini et al., 2009, p. 214). However, for loads approaching peak values, the microcracks start to extend out into the concrete matrix and permeability greatly increases (Hoseini et al., 2009, p. 214).

The study found that crack geometry, specifically the crack width and tortuosity, have a significant impact on permeability while crack length has little effect (Hoseini et al., 2009, p. 217). In fact, there is a relationship between crack width and permeability of concrete. “For cracks wider than 1 mm, permeability in concrete is proportional to the cube of the crack width (Mehta et al., 2006, p. 68). Hence, a specimen with several smaller cracks will be less permeable than that with a single large crack” (Hoseini et al., 2009, p. 217).

Several studies have tried to evaluate a threshold value for crack opening displacements (COD). In their study “Wang et al. reported a threshold value of 50 μm , while Aldea et al. found a threshold crack width of 100 μm for concrete specimens under load. In other related studies the threshold crack width was found to be twice as much (200 μm) for chloride permeability” (Hoseini et al., 2009, p. 217).

2.3.4 Loading

While the effects of transport mechanisms on the durability of concrete have been well studied, there is very little existing literature on how these mechanisms are affected by mechanical stress (Hoseini et al., 2009, p. 213). “The type of applied stress (compression, tension and flexure), the rate of loading and the load level (as a fraction of ultimate), all influence the crack generation and pattern (Hoseini et al., 2009, p. 214). Changing the crack pattern inevitably changes the permeability of the concrete (Hoseini et al., 2009, p. 214).

There have been a few studies which have investigated the effects of mechanical loading on permeability. Kermani et al. evaluated the permeability of concrete after the specimen were unloaded (Hoseini et al., 2009, p. 214). Based off their findings, a threshold stress level of approximately 40% of ultimate was proposed (Hoseini et al., 2009, p. 214). After this stress level has been reached the permeability of concrete was found to increase rapidly (Hoseini et al., 2009, p. 214). The study revealed that for lower levels of compressive loading, permeability was found to be constant or decrease slightly. This constant or slight drop in permeability was because of “consolidation or closing of voids and microcracks in concrete” (Hoseini et al., 2009, p. 216). In Figure 2-8 one can see further evidence of this consolidation. It was found that for threshold stresses up to 80% of the peak stress, the permeability of concrete was higher after removing the compressive load (Hoseini et al., 2009, p. 216). In fact, after removing the load permeability was found to remain constant for loads up to 70-80% of ultimate (Hoseini et al., 2009, p. 216). This is in direct contrast to the stress dependent behavior of permeability under load (Hoseini et al., 2009, p. 214).

Different studies have found other interesting effects that monotonic and cyclic loading have had on permeability. A study was conducted evaluating the chloride permeability of concrete

per AASHTO T277. This study found that concrete subjected to a monotonic compressive stress, even at ultimate, displayed only a marginal difference in chloride permeability (Hoseini et al., 2009, p. 217). However, under cyclic compressive loading, there was a distinguishable threshold stress at 50% of ultimate beyond which there was a significant increase in the chloride permeability (Hoseini et al., 2009, p. 217). Therefore, “cyclic loading was seen to lower the threshold value of stress” (Hoseini et al., 2009, p. 217).

2.3.5 Fiber Reinforcement Concrete (FRC)

As seen earlier, cracks have more of an influence on permeability when they propagate in the concrete matrix as opposed to the ITZ (Hoseini et al., 2009, p. 214). Recall that for cracks wider than 1 mm, permeability in concrete is proportional to the cube of the crack width (Hoseini et al., 2009, p. 217). Therefore, the use of FRC would be highly beneficial in reducing permeability since the bridged cracks would be smaller (Hoseini et al., 2009, p. 218). Even though FRC has higher unrecoverable deformation, the use of fibers reduces permeability (Hoseini et al., 2009, p. 218). “This is likely due to a change in the crack profile... whereby, instead of the appearance of a few large cracks, a multitude of closely spaced microcracks form” (Hoseini et al., 2009, p. 218).

2.3.6 Conclusion

The study concluded that under applied compressive stress there is a threshold value of 30% of ultimate strength, beyond which the permeability of concrete greatly increases (Hoseini et al., 2009, p. 219). Furthermore, for normal weight concrete (NWC) the permeability is strongly related to the matrix strength (Hoseini et al., 2009, p. 218). “This has to do with a slower crack recovery in normal strength concrete.... Compared to the highly linear stress-strain response of

high strength concrete (HSC) (Hoseini et al., 2009, p. 218). The use of fibers can reduce the permeability of concrete by bridging microcracks before the coalesce and interconnect. “Although the total crack width was far greater with ultra-high performance concrete (UHPC), the permeability was significantly reduced, since individual cracks were much finer in the UHPC than in the normal concrete” (Hoseini et al., 2009, p. 219). Cyclic loading leads to a significant increase in permeability compared to monotonic loading (Hoseini et al., 2009, p. 219). The COD threshold value ranges from 50-100 μm after which permeability greatly increases (Hoseini et al., 2009, p. 219). The permeability does reach a constant flow as the specimen approaches failure (Hoseini et al., 2009, p. 219). From Figure 2-8 it is clear that for a given COD, “concrete is less permeable when under load (Hoseini et al., 2009, p. 219).

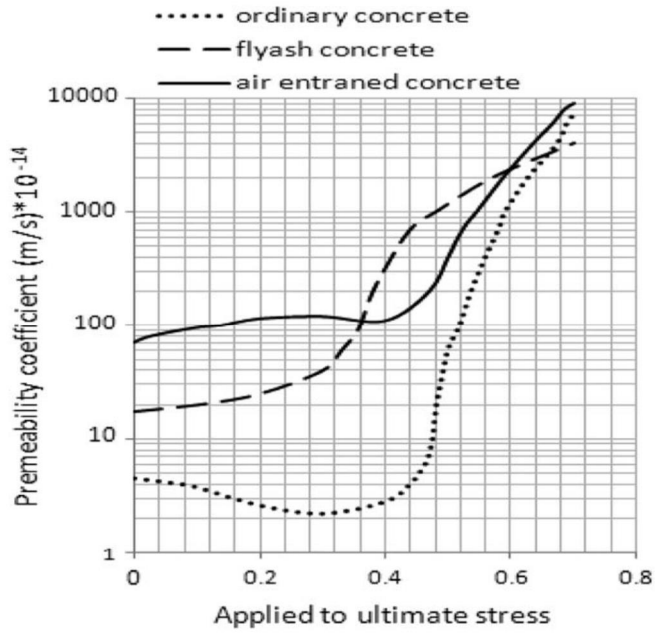


Figure 2-7: Effect of load levels on permeability under compression (Hoseini et al., 2009, p. 216)

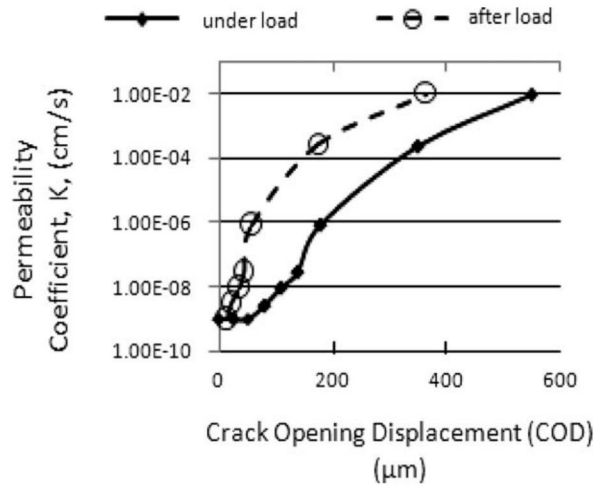


Figure 2-8: Relation between water permeability and crack opening displacement (Hoseini et al., 2009, p. 217)

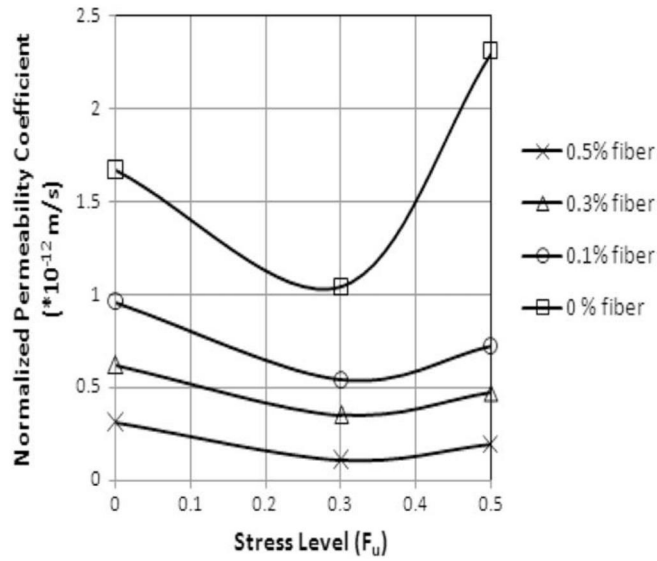


Figure 2-9: Effect of stress on the relative permeability of plain concrete and FRC. (Hoseini et al., 2009, p. 218)

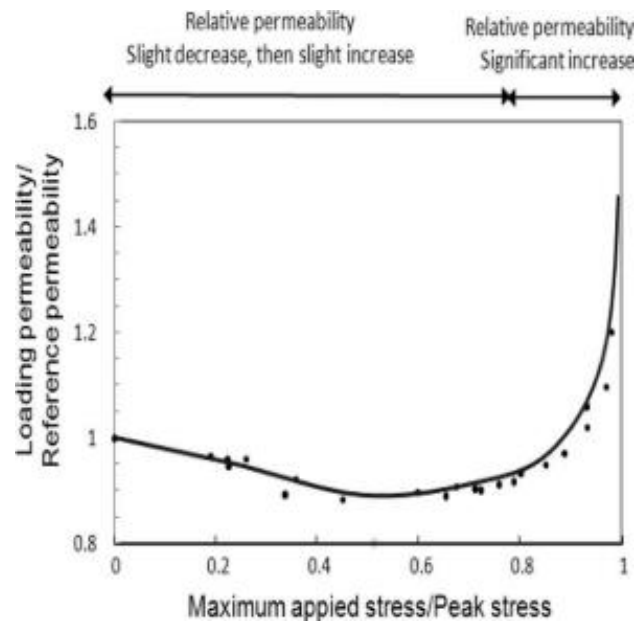


Figure 2-10: Effects of applied stress on permeability (Hoseini et al., 2009, p. 217)

$$J = \frac{k'}{\eta} \text{grad}(P)$$

Equation 2-1: Darcy's Law, where J is the volumetric flow rate (m/s), k' is the intrinsic permeability (m^2), η is the dynamic viscosity (kg/ms) and P is the pressure (Pa) (Hoseini et al., 2009, p. 214).

2.4 Electrical Resistivity of Concrete; Concepts, Applications, and Measurement Techniques by Layssi et al.

2.4.1 Introduction

This publication evaluates different approaches in determining the durability of concrete through measuring the ESR. Similar testing methods such as RCIP are briefly discussed. An ESR testing setup using the Wenner four-probe test configuration is proposed. An ESR test with such a configuration can be related to the chloride permeability by the Nernst-Einstein equation. It is well known that the durability of concrete is highly depended on its microstructure (Layssi et al., 2015, p. 41). Pore size distribution, interconnectivity, and tortuosity all have a big impact on permeability (Layssi et al., 2015, p. 41). ESR itself is also affected by pore size distribution and interconnectivity but additionally is sensitive to degree of saturation and temperature (Layssi et al., 2015, p. 43). Therefore samples should be conditioned prior to testing in a “surface dry (SSD)” state and temperature should be closely monitored (Layssi et al., 2015, p. 43).

2.4.2 RCIP

The standard test for RCIP, originally proposed by Whiting, measures the total electrical charge passed through a concrete specimen subjected to an applied voltage (Layssi et al., 2015, p. 41). By measuring the electrical charged passed, the test provides an indication of the chloride permeability and thus the durability of concrete. This testing method is rather inconvenient, however, since it requires a significant amount of time and damages the concrete sample (Layssi et al., 2015, p. 41). Furthermore, the results are more qualitative rather than quantitative. The amount of charge passed is related to the chloride permeability by Figure 2-12.

2.4.3 ESR

Instead, quantitative tests that measure the ESR and are related linearly to the chloride diffusion coefficient by the Nernst-Einstein equation (see Figure 2-13.), require far less time (Layssi et al., 2015, p. 41). The ESR of concrete is the ability to withstand the transfer of ions subjected to an electrical field (Layssi et al., 2015, p. 41). Measurements obtained from ESR are a reflection of the interconnectivity of the pore network (Layssi et al., 2015, p. 41). One needs to consider the capacitive properties of concrete and how it will affect the ESR measurements (Layssi et al., 2015, p. 42). If an AC circuit is used, then the effects of capacitance are no longer a concern, however, reactance is now introduced into the system (Layssi et al., 2015, p. 42). Reactance is a non-resistive opposition to current in an AC circuit (Layssi et al., 2015, p. 42). Therefore, one needs to consider the Impedance (Z) of the system. Impedance is the combined “opposition to current resulting from resistance (R) and reactance (X) (Layssi et al., 2015, p. 42). A geometric description of the reactance and impedance can be seen in Figure 2-11.

One commonly accepted ESR testing configuration is the Wenner probe method in which four electrodes are evenly spaced in a straight line (Layssi et al., 2015, p. 42). The two interior electrodes measure the potential (V) “created when the exterior electrodes apply an AC current to the concrete” (Layssi et al., 2015, p. 42). Such a probe configuration is highly sensitive to the surface conditions of the concrete (Layssi et al., 2015, p. 43). The degree of saturation and the presence of surface cracks can greatly impact the ESR results (Layssi et al., 2015, p. 43). It is therefore advisable to take the average of four probe set readings spaced evenly around the sample (Layssi et al., 2015, p. 43).

ESR measurements are also sensitive to temperature. This is because “the electric current flow in concrete is the result of ionic movement within the pore solution, and ionic mobility is

affected by temperature” (Layssi et al., 2015, p. 43). In general, an increase in ionic mobility and thus in electric resistivity, results from an increase in temperature (Layssi et al., 2015, p. 43). For a temperature difference of 1°C (1.8°F) the ESR of concrete can be off by 3% 1.8°F.

2.4.4 Conclusion

ESR testing methods, utilizing the four-point Wenner probe configuration, offer a more effective testing procedure to determine the durability of concrete by measuring chloride diffusion (Layssi et al., 2015, p. 42). The chloride diffusion coefficient is related to the ESR linearly by the Nernst-Einstein equation (Layssi et al., 2015, p. 41). Any “nonlinear relationship between electrical resistivity and RCP values is largely the result of changes in the temperature and properties of the pore solution during the RCP test.” (Layssi et al., 2015, p. 45) The condition of the sample surface, such as the presence of cracks and the degree of saturation, can have a big impact on the measured ESR (Layssi et al., 2015, p. 43).

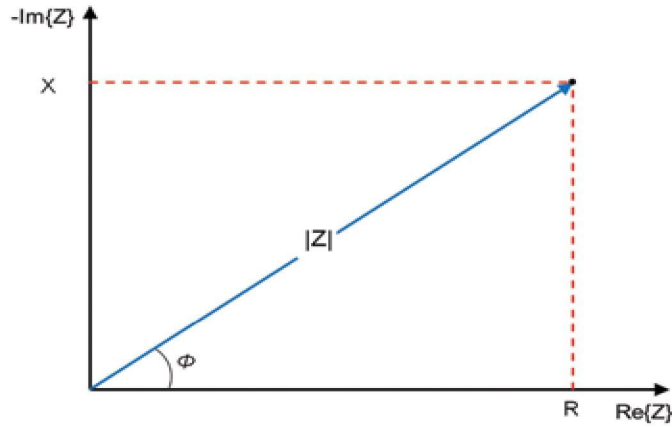


Figure 2-11: Impedance is a complex number that can be represented as the vector sum of resistance on the real axis and reactance on the negative imaginary axis.

Chloride Penetration	56-Day Rapid Chloride Penetrability Charge Passed as per ASTM C1202	28-Day Surface Resistivity**
	(Coulombs)	(kΩ.cm)
High	>4,000	<10
Moderate	2,000-4,000	10-15
Low	1,000-2,000	15-25
Very Low	100-1,000	25-200
Negligible	<100	>200

* Adapted from Kessler et al. 2005

** At 23 °C

Figure 2-12: Relationship between ESR and chloride penetration (Giatec Scientific, p. 5)

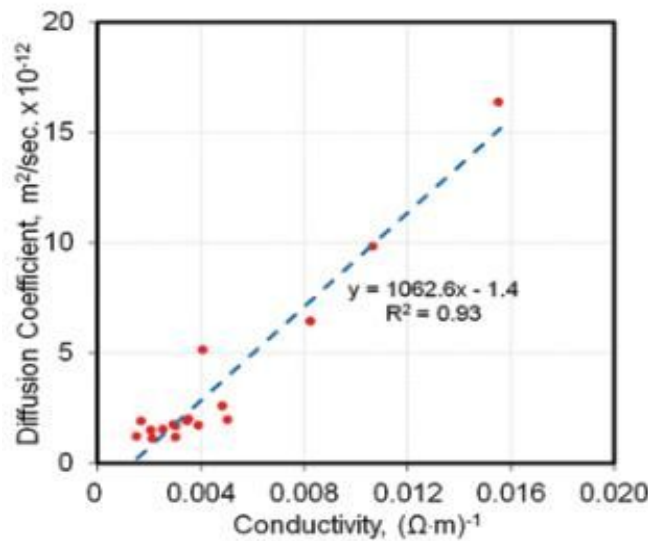


Figure 2-13: Relationship between electrical conductivity and chloride diffusion coefficient (Layssi et al., 2015, p. 45)

3 Experimental Program

3.1 Introduction

Much time and dedication of resources has been spent on understanding how to improve the durability of concrete. Despite our best efforts, however, concrete (such as that used for bridge deck) continues to deteriorate prior to reaching its designed service life. In a previous study, Lin et al. (2012) (see section 2.1) concluded that stress induced from mechanical compressive wheel loads from overweight vehicles combined with F/T action can cause early deterioration of bridge deck. The report by Lin et al. (2012) concluded that microcracks caused by these combined stresses created a pathway for harmful chloride ions to penetrate and cause early deterioration. Regarding this study there is concern in several key areas as subsequently listed

- Concrete samples were subjected to freeze thaw cycles. However, dynamic modulus, a known method for determine deterioration of concrete subjected to F/T, was never determined.
- The water absorption was not measured per ASTM C642. Hence the correlation between the water absorption and the concrete durability, as concluded by the researchers (see Figure 2-2), should be further examined.
- The research concluded that water absorption tests can be used to evaluate the durability of field concrete samples and thus serves as an indication of the deterioration of concrete bridge decks. This conclusion needs to be examined using more tests of concrete samples for a variety of well-established concrete durability measurements.

The intent of this current study is to reevaluate water absorption as it relates to concrete durability. By adhering more closely to ASTM standards for testing and by including other

concrete durability tests, the author hopes to substantiate the claim made by Lin et al. (2012). The claim that water absorption (ASTM C642) may be used as a more effective testing method to determine the durability of concrete.

3.2 Objectives

The objectives of the experimental program are to;

1. Examine the conclusion of the previous study that water absorption is effective for testing concrete durability by showing it directly correlates with electric resistivity and dynamic modulus.
2. Lay a foundation for validating the relationship between water absorption and the durability of concrete, especially the concrete in bridge decks that are subjected to combined mechanical loading and F/T cycles.
3. Provide equations for others to check their own results of absorption for mechanically loaded F/T concrete.
4. Provide an array of water absorption test results for 2"x4" concrete disks to be compared with subsequently proposed ASTM C1202: RCIP testing on the same specimen.

3.3 Specimen Design

From the previous study by Lin et al. (2012) there remained fifteen 8" x 4" concrete cylinders and sixty-two 2" x 4" concrete disks. These concrete samples had been subjected to compressive loading of approximately 40 percent of the measured 28-day strength, though the information on the exact loading levels is unknown. The cylinders and disks were created using an air entrained Grade A-FA concrete mixture as specified by WisDOT (Lin et al., 2012, p. 44). The w/c ratio for

the concrete was 0.4 and the total amount of FA used was 30% of the total cementitious material by weight (Lin et al., 2012, p. 25). Because the compressive stress which each specific sample was subjected to is unknown, the study; which focused on the verification of water absorption and the concrete durability represented by dynamic modulus and surface resistivity; is therefore blind. The study was designed as such to remove any possible bias that could impact the results.

The 2” tall concrete cylinders were separated into groups of nine and were labeled with a “D” denoting disk samples. These samples were labeled alphabetically ranging from B-H, and then numerically 1-9 (e.g. D-1B). These concrete samples were tested for water absorption according to ASTM C642. Later research is proposed to test the same samples for RCIP per ASTM C1202.

The 8” tall concrete cylinders retained their original designations which intermittently ranged from C-06 through C-42. These samples were tested for dynamic modulus (ASTM C215), water absorption (ASTM C642), and electric resistivity. At the conclusion of these tests, using a water-cooled diamond saw, the cylinders were cut down to 2” tall disks. These samples were designated with a D followed by the cylinder number from which they were cut and then by the cut number. The cut number ranged from 1 through 4 with 1 and 2 corresponding to the two interior cuts (see Figure 3-4). These samples were tested for water absorption (ASTM C642) and will join the other disks for RCIP testing to follow.

3.4 Dynamic Modulus

The dynamic modulus of the concrete samples was tested using the contact driven forced resonance method outlined in ASTM C215. The mass, length and cross sectional area were measured for all of the 8” tall concrete cylindrical specimen. With the length known, the approximate location for the supports could be determined as $0.224L$ from each end of the cylinder

(see Figure 3-1). The supports were soft rubber pads such that the concrete sample was allowed to vibrate freely (ASTM C215, p. 2). The electro-mechanical driving unit was placed at the top of the specimen, approximately half the length down longitudinally. The accelerometer was placed at the end of the specimen perpendicular to the driving unit (see Figure 3-2). The reason for such a configuration is because the vibrations are at maximum at the ends of the sample, approximately three fifths of the maximum at center, and zero at the nodal points (ASTM C215, p. 4). Petroleum jelly was used where the driving unit and the accelerometer were in contact with the concrete specimen (to ensure good contact and adequate vibration transmission). The specimen was subjected to vibrations at varying frequencies ranging from 1k to 10k hertz. A meter indicator was used in place of an oscilloscope to measure the output frequency. The frequency at which the needle on the meter indicator reached its peak value was recorded as the fundamental transverse frequency of the specimen (ASTM C215, p. 3). The samples were tested a second time so that an average peak frequency could be determined.

It should be mentioned that the dynamic modulus of samples; C-15, C-17, C-21, C-22, C-28, C-29, C-30, C-34, C-35, C-40, and C-42; were tested within a couple of days of each other in the month of July. Samples; C-06, C-11, C-14, and C-16; were tested later in the experimental program in the month of November. While all testing was conducted in climate controlled environments, the difference in time between tests is worth mentioning because ambient humidity has been known to affect the results of dynamic modulus testing.

To calculate the dynamic modulus, a correction factor T needed to be determined from ASTM C215 Table 1. The correction factor is dependent on the Poisson's ratio of the concrete. The concrete specimens were obtained from a previous study, Lin et al. (2012), in which the Poisson's ratio was never determined. Poisson's ratio could be determined by ASTM C469: Standard Test

Method for Static Modulus of Elasticity and Poisson's Ratio of Concrete in Compression. However, this would alter the microstructure of the samples because the standard requires the samples to be loaded to 40% of the ultimate load (ASTM C469, p. 4). For concrete under uniaxial compression, stress levels between 0.3 through 0.5 percent of f'_c are high enough to cause extension of microcracks in the ITZ (Mehta et al., 2006, p. 68). If the microstructure of the samples was altered, then making a comparison of durability results from one test standard to another would be nonsensical since permeability would increase. Therefore, instead of determining the Poisson's ratio of the concrete, the value was assumed to be 0.17. This is a reasonable assumption because for lower values of k/L the calculated correction factor T , and the resulting dynamic modulus, only varies by 2% for values of Poisson's ratio varying from 0.17 to 0.26 (the upper and lower values for Poisson's Ratio in ASTM C215 Table 1).

While collection data, it was observed that the testing apparatus did not always perform correctly, if the driving unit and the concrete specimen were too in contact, then the vibration from the driving unit sounded dull. However, if the driving unit was just barely in contact with the concrete specimen, then the sound of the vibration resonated with more of a buzzing noise. It was observed while testing a specimen for the second time, that if the driving unit sounded dull, then a peak frequency observed during the first test (when the driving unit was resonating) would not register on the needle indicator. Furthermore, for lower range frequencies (typically less than 2500 Hz) the driving unit would sound dull regardless of the contact condition with the concrete specimen. The lower range frequencies could still be tested by going to a higher frequency first, to obtain the right sound (typically 4000 Hz), and then by moving back down the frequency spectrum. The resonating sound would be carried down through the lower frequency ranges until

approximately 1600 Hz when the dull sound would return. These complications could be one source of error that resulted in the high standard deviation discussed later in section 4.

3.5 Water Absorption

3.5.1 Oven-Dried State

The absorption of the concrete specimens was evaluated per ASTM C642. The concrete specimens were oven-dried in stainless-steel containers at a temperature of 110°C (230°F) for a period of 24 hours (ASTM C642, p. 1). After 24 hours, the containers were taken out of the oven and the samples were temporarily removed from their containers. The bottoms of the stainless-steel containers were lined with 2” by 2” concrete cube spacers and approximately ¼” deep of Drierite™ indicator desiccant crystals (see Figure 3-3). The concrete specimen sat above the desiccant crystals on top of the concrete cube spacers. This was done to increase the amount of surface area of the samples exposed to air within the container so that they might stay dry and cool at a faster rate. Once the concrete specimens were placed back into the stainless-steel containers, the containers were covered with saran wrap. The saran wrap was secured underneath the lip of the containers with tape running along the containers perimeter (see Figure 3-5). After application, the saran wrap was visually inspected for punctures. Any holes in the saran wrap were quickly covered with tape. The purpose for the desiccant crystals and saran wrap was to ensure that the concrete specimen stayed in an oven-dried state, free from the influence of ambient humidity. A desiccator could have been used as recommended by the standard, however, this would have significantly slowed down the process because it would permit the testing of only a few samples at a time. The samples were cooled by natural heat loss, typically for eleven hours, to a final temperature ranging from 20°C to 25°C (68°F to 77°F) (ASTM C642, p. 1). The mass of the samples was recorded as the oven-dried mass (A) (ASTM C642, p. 1). This process was repeated

until the difference between successive values of mass were less than 0.5% of the lesser value (ASTM C642, p. 1).

3.5.2 Saturated After Immersion State

The concrete samples were temporarily taken out from their stainless-steel containers. The concrete cubes and Drierite™ desiccant crystals were removed and the containers were rinsed and whipped out. The samples were placed back into the stainless-steel containers and were covered with tap water. The samples sat submerged in the water for a period of 48 hours (ASTM C642, p. 1). The samples were removed individually from the containers and were blotted with paper towel to achieve a fully saturated surface dried condition. The mass of each sample was recorded as the saturated after immersion mass (B) (ASTM C642, p. 1). This process was repeated until the difference between successive values of mass were less than 0.5% of the larger value (ASTM C642, p. 1).

3.5.3 Saturated After Boiling State

The stainless-steel containers holding the concrete specimen were placed on an electric double burner and were boiled for a duration of five hours (ASTM C642, p. 1). During this period, the level of the water was checked approximately every twenty minutes to ensure the concrete samples remained fully submerged. If the water level was too close to the top surface of the concrete specimen, more water was added. The added water was first boiled from an additional heat source. The concrete specimen were “cooled by natural heat loss for not less than 14 hours to a final temperature of 20°C to 25°C” (68°F to 77° F) (ASTM C642, p. 1). The samples were blotted dry with paper towels and the mass was recorded as the saturated mass after boiling (C) (ASTM C642, p. 1).

3.5.4 Immersed Apparent State

The mass of the concrete samples immersed in water was determined. The concrete samples were individually placed into a metal basket suspended by a string in a large barrel of water. The string was secured, through a hole in the table above, around the top plate of the scale (see Figure 3-6). The mass was recorded as the immersed apparent mass (D) (ASTM C642, p. 1).

3.6 Electric Resistivity

ESR of the concrete samples was evaluated using a Giatec Surf^{ftm} testing apparatus consisting of a measuring device and a sample chamber (see Figure 3-8). This testing device uses the Wenner four electrode configuration with four evenly spaced electrodes in a straight line along the length of the sample (Giatec Scientific, p. 7). The two inner electrodes measure the electrical potential, V , created when AC current (I) flows from the exterior electrodes into the concrete (see Figure 3-7) (Giatec Scientific, p. 7). There are four sets of electrodes perpendicular to each other at 90° (Giatec Scientific, p. 9). The sample holder was designed to facilitate “eight measurements of resistivity around the test sample (while) also reducing the evaporation rate during the test (Giatec Scientific, p. 9). The ESR for a semi-infinite, homogeneous concrete is calculated by Equation 4-5, where a is the distance between the equally spaced electrodes (Giatec Scientific, p. 7).

The ends of the sixteen electrical probes were coated with a dab of conductive gel to aid in the transfer of applied voltage to the concrete specimen. Testing for ESR requires that the samples be conditioned such that they are in a fully saturated surface dry state. The concrete samples were already saturated from the absorption tests. The samples were blotted with paper towel before being placed into the testing apparatus. The top and bottom surface of the samples were aligned with the rubber supports (Giatec Scientific, p. 11). The top probes were put in contact with the

concrete specimen when the lid was tightly closed. Prior to testing, all the probes were visually examined for proper contact to the specimen. The test was then conducted using the SurfTM data monitoring software. The test was repeated three times for each sample. In between tests the concrete samples were taken out of the testing chamber, conductive gel was reapplied to each probe, and the specimen was slightly rotated before being placed back into the sample holder. An average was taken from the total 24 ESR measurements per concrete specimen (see Figure 7-1 through Figure 7-15).

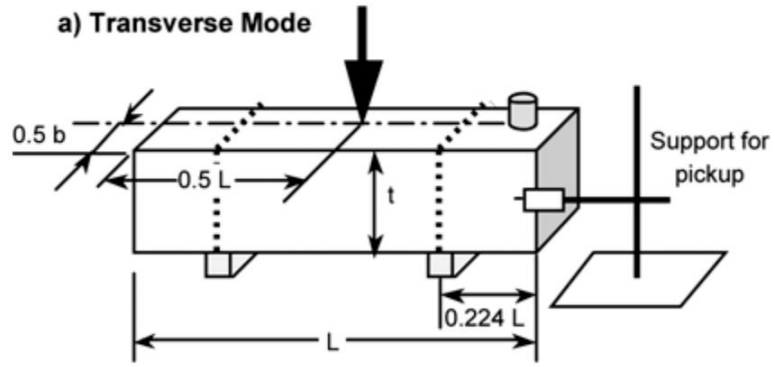


Figure 3-1: ASTM C215 Transverse Mode (ASTM C215, p. 3)

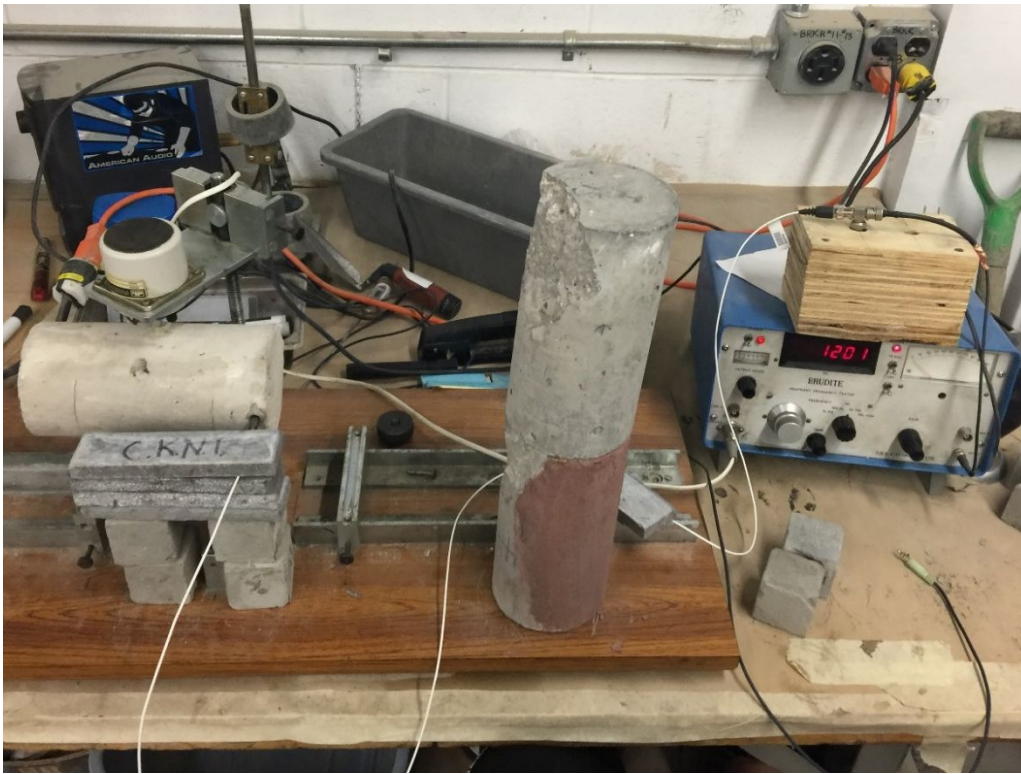


Figure 3-2: Transverse frequency testing ASTM C215.



Figure 3-3: Oven-dried concrete samples being placed in a stainless-steel container to cool above Drierite™ indicator desiccant crystals.

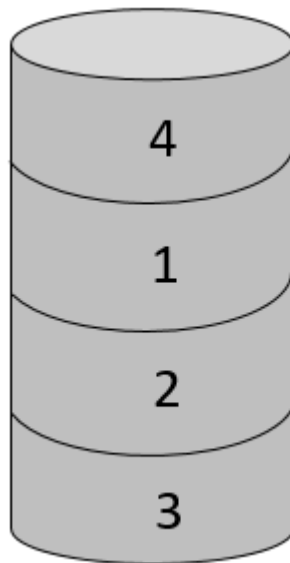


Figure 3-4: Designation of each cut number per cylinder.



Figure 3-5: Oven-dried concrete samples sitting inside stainless-steel containers sealed with saran wrap which was secured with tap underneath the lip of the containers.



Figure 3-6: Mass of suspended concrete samples submerged in water per ASTM C642.

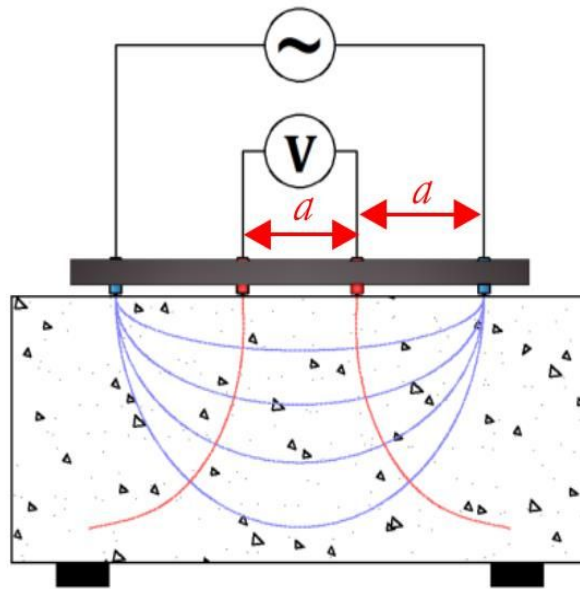


Figure 3-7: Schematic view and concept of the test setup (Giatec Scientific, p. 7)



Figure 3-8: Surf™ testing apparatus.

Chloride Penetration	56-Day Rapid Chloride Penetrability Charge Passed as per ASTM C1202	28-Day Surface Resistivity**
	(Coulombs)	(kΩ.cm)
High	>4,000	<10
Moderate	2,000-4,000	10-15
Low	1,000-2,000	15-25
Very Low	100-1,000	25-200
Negligible	<100	>200

* Adapted from Kessler et al. 2005

** At 23 °C

Figure 3-9: Relationship between ESR and chloride penetration. (Giatec Scientific, p. 5)



Figure 3-10: Cutting concrete cylinder samples with water-cooled diamond saw.



Figure 3-11: Epoxied samples in preparation for proposed RCIP testing

4 Data Analysis

4.1 Dynamic Modulus

Calculation of the dynamic modulus involves three variables, specifically; C , the geometrical correction factor (m^{-1}); M , the mass (kg); and n , the fundamental transverse frequency (Hz) (see Equation 4-1) (ASTM C215, p.5). The geometrical correction factor (C), as described by Equation 4-2, is dependent on the correction factor (T) (ASTM C215, p.5).

The correction factor (T) can be determined from Table 1 in ASTM C215, and is dependent on the Poisson's ratio of the concrete specimen (ASTM C215, p.6). The concrete specimens were obtained from a previous study, Lin et al. (2012), in which the Poisson's ratio was never determined. The Poisson's ratio could be determined by ASTM C469. However, this would alter the microstructure of the samples because the standard requires the samples to be loaded to 40 percent of the $f'c$ (ASTM C469, p. 4). For stress levels between 30 to 50 percent of $f'c$, crack propagation is still considered stable, however, microcrack extension does occur solely within the ITZ (Mehta et al., 2006, p. 68). Propagation does not yet extend into the cement matrix until stress levels of 50 to 75% $f'c$ (Mehta et al., 2006, p. 68). Therefore, loading the samples to 40 percent of $f'c$, as recommended by the standard, would increase the permeability locally around the ITZ. Altering the microstructure of the samples in such a way would make any comparison between the results from one test standard to another nonsensical because permeability would increase. Therefore, instead of determining the Poisson's ratio of the concrete, the value was assumed to be 0.17. This is a reasonable assumption because for lower values of k/L the calculated correction factor T , and the resulting dynamic modulus, only varies by 2% for values or Poisson's ratio varying from 0.17 to 0.26 (the upper and lower values for Poisson's Ratio in ASTM C215 Table 1).

Evaluating the average peak frequencies two of the values obtained, specifically that for C-28 and C-40, can be considered outliers since their values are higher than 2345 Hz. This threshold was found by calculating the third quartile plus 1.5 times the interquartile range. These values cannot be dismissed, however, solely based off the peak frequencies. Recall that the compressive stress and number of F/T cycles applied to each sample during the study by Lin et al. (2012) is unknown. Therefore, it is possible that the peak frequencies for these samples were higher because they may have been subjected to less compressive stress or F/T cycles (or both).

Some of the samples; C15, C28, C-29, C-40 and C-42; had average peak frequencies with significantly high standard deviations, as can be seen from Figure 4-1. These standard deviation ranged from 1301 to 2802 for samples C-15 and C-40, respectively. One possible cause for the high standard deviations, as previous discussed in section 3.4, could be attributed to the difficulties in using the fundamental transverse testing equipment. Alternatively, as recommended in ASTM C215, the use of a real-time graphic display, such as an oscilloscope, could have aided in finding more accurate results (ASTM C215, p. 2). It could be argued that the dynamic moduli for these samples are dismissible due to their extremely high standard deviations. Representing only the statistically sound data, the dynamic modulus results (see Table 4-1) have been consolidated as seen in Table 4-2. The remaining discussion regarding dynamic modulus results will be focus exclusively on this consolidated data.

Considering only the consolidated results, the average of the peak frequency was found to be 2230 Hz with a standard deviation of ± 486 Hz. The peak frequencies ranged from 1438 Hz to 3308 Hz as observed from samples C-34 and C-17, respectively. The dynamic moduli were calculated by Equation 4-1, where; n is the average peak frequency (Hz), M is the mass (kg), and C is a dimensional factor calculated by Equation 4-2; the results of which can be seen tabulated in Table

4-2. The average dynamic modulus was 5.24E06 KPa with a standard deviation of $\pm 2.18E06$ KPa and a range of 2.06E06 KPa through 9.17E06 KPa for samples C-34 and C-17, respectively. Such a large variance in average peak frequency and dynamic modulus can most likely be attributed to the variability in applied compressive stresses and F/T cycles which the samples were subjected to during the study by Lin et al. (2012).

A comparison between the consolidated data for dynamic modulus and PV can be seen in Figure 4-9. In this figure the distribution of data and R^2 indicate an extremely weak relationship between dynamic modulus and PV. A trendline has been generated, however, to do the large variation in data the accuracy of such a trendline is not highly reassuring. The trendline shows that the two variables are directly proportional which cannot possibly be the case. One would expect that as the percent of permeable voids increases, that the dynamic modulus would decrease. As the volume of the pore network increases from microcrack interconnectivity, the dynamic modulus should decrease. It is possible the sample size was not large enough to develop an accurate depiction on the behavior of these two variables in relation to each other. Such is also the case for the comparison between the average surface resistivity and the dynamic modulus (see Figure 4-10). Here again, a large variation in data does not provide a very reassuring relationship between the two parameters.

4.2 Water Absorption

PV was calculated from the mass of each concrete specimen under four different saturation states; oven-dried, saturated after immersion, saturated after boiling, and immersed apparent. The mass of the cylinders and disks for each saturation state can be seen in Table 4-3 and Table 4-5, respectively. The calculated values for; the absorption after immersion (%) (ASTM C642 Eqn. 8),

absorption after immersion and boiling (%) (ASTM C642 Eqn. 9), bulk dry density (Mg/m³) (ASTM C642 Eqn. 10), bulk density after immersion (Mg/m³) (ASTM C642 Eqn. 11), bulk density after immersion and boiling (Mg/m³) (ASTM C642 Eqn. 12), apparent density (Mg/m³) (ASTM C642 Eqn. 13), and PV (ASTM C642 Eqn. 14); can be seen for the cylinders and disks in Table 4-4 and Table 4-6, respectively.

Evaluating the effects of mass at various saturation states on PV, some interesting observation can be made. For masses A, B, C, and D (see Figure 4-4 and Figure 4-5). PV decreases as the mass of the samples in each saturation state increases. Regression analysis was used to determine a line of best fit for each mass at their respective saturation state. The relationship between mass and PV is strongest when compared to the oven-dried mass (A) with R² equal to 85.4%. As the saturation levels of the cylindrical concrete specimen increase, the strength of R² decreases from; 59.6% for mass B, to 53.2% for mass C. There is a slight increase in the R² for the immersed apparent mass (D) at 60.4%. Therefore, PV is most dependent on mass A and D. Hopefully the regression analysis and general equations provided for the cylinder samples will serve others. The result obtained by others performing similar research of mechanically loaded, F/T concrete could be checked against the regression analysis and general equations. Note, caution should be exercised when comparing results since the population size of this group is rather small.

An example of the inversely proportional relationship between PV and mass can be seen with sample C-42. This specimen had the highest oven-dry mass at 3915.0 g and the lowest percent gain in absorption after immersion of 2.7%. Therefore, it makes sense that sample C-42 had the lowest PV at approximately 7.0%. Because the volume is constant across the cylinder samples, the density of C-42 would therefore be higher as well. In fact, C-42 does have the highest bulk-dry

density of 2.34 Mg/m³. This indicates that not only does C-42 have less voids, but possibly that the voids are less interconnected as reflected by its low absorption after immersion of 2.7%.

It should be mentioned that after four successive attempts to dry samples; D11-1, D14-2, D15-1, D15-2, D28-2, D34-2, D35-1, D42-1, and D42-2, per ASTM C642, the successive values for the oven-dry mass were not less than 0.5% as specified by the standard. The reason for such a long drying period is because the disks had been recently saturated. The source of the saturation was from the water used to cool the diamond cutting blade when the cylinder samples were cut and divided into the disk samples. The highest deviation from the 0.5% threshold value was 0.53% from disk samples; D15-2, D28-2, and D35-1. Due to time constraints, the last recorded oven-dried mass was designated as the mass value A for each sample. Had an additional 24 hours of oven drying been provided, as specified by the standard, the percent increase in mass would have been well below the threshold value of 0.5%. From experience, given an additional 24 hours, the mass would have been the same regardless. Therefore, these samples were moved onto the saturated after immersion stage in testing.

4.3 Electric Resistivity

Each concrete specimen was tested three times to determine the electrical surface resistance. Four sets of probes were orientated perpendicularly along the length of the specimen at 0°, 90°, 180°, and 270°. Each set of probes were arranged in a Wenner four electrode configuration and measured the potential drop in voltage along the concrete specimen (Giatec Scientific, p. 7). An average of the twenty-four surface resistance (R) measurements were calculated per specimen (see second column of Table 4-7). A geometrical factor (k) was applied to determine the average surface resistivity (ρ) (see Equation 4-6). For a 4" x 8" cylinder the geometrical factor, which is

dependent on probe spacing, was calculated to be 1.95. By multiplying the geometrical factor (k) by the surface resistance (R), the average surface resistivity (ρ) per concrete specimen was calculated. The calculated ρ -values per cylinder can be seen in the third column of Table 4-7 and in Figure 4-6.

The data generated in for each of the cylinder samples can be seen from Figure 7-1 through Figure 7-15 of the appendix. The average calculated resistivity was found to be 18.8 k Ω /cm with a standard deviation of ± 3.1 k Ω /cm. The values ranged from 15.0 k Ω /cm for sample C-14, and 25.7 for sample C-11. The average electrical resistivity is related to the chloride penetration by Figure 3-9, as determined by ASTM C1202. Here the electrical resistivity is divided into five categories relating to chloride penetration; high, moderate, low, very low, and negligible. It was found that all the cylinder samples had an equivalent chloride penetration ranging from moderate to high. This data provides a good indication of what chloride penetration values could be expected from the proposed RCIP testing on the disks cut from these cylinders. Assuming the behavior of each individual disk will reflect that of the cylinders from which they were cut, it is likely that the disk samples will have chloride penetration values of 2,000 to over 4000 coulombs.

Evaluating the relationship between ESR and PV we can see from Figure 4-7 that the two are inversely proportional. As PV decreases there would be less saturated pore space to carry the electrical charge, therefore, one would expect that the ESR would decrease. R^2 for the two variables was 31%. From Figure 4-7, two of the cylinder samples a very clearly outliers. Excluding these two samples, C-14 and C-42, the relationship becomes even stronger with R^2 equal to 63.5% (see Figure 4-8).

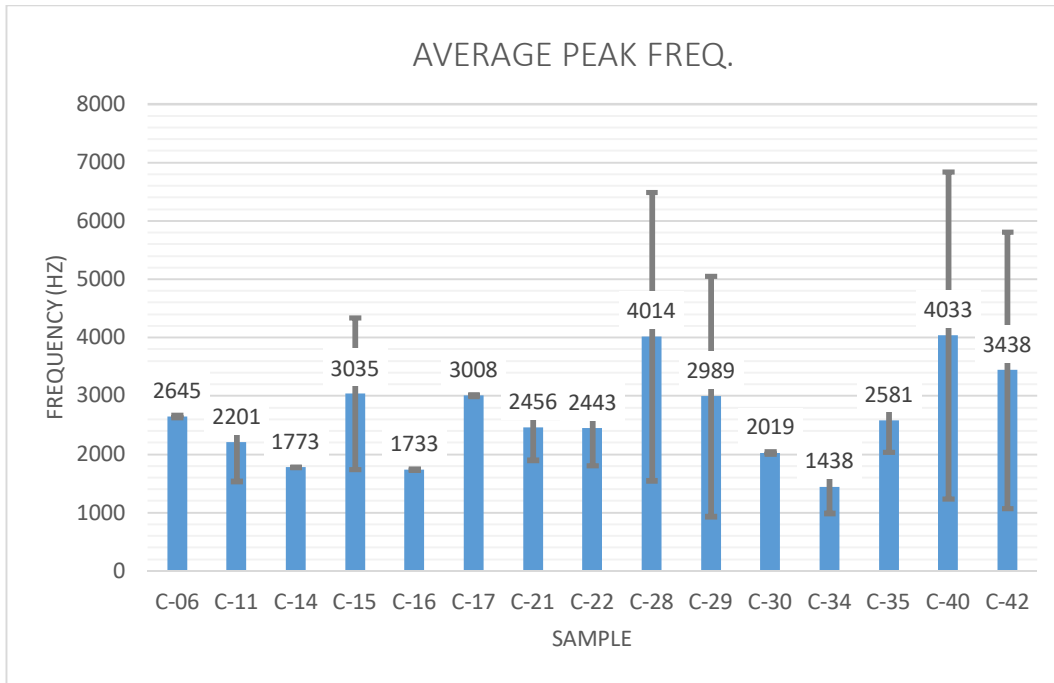


Figure 4-1: Average Peak Frequency (Hz) recorded per sample according to ASTM C215 with standard deviation error.

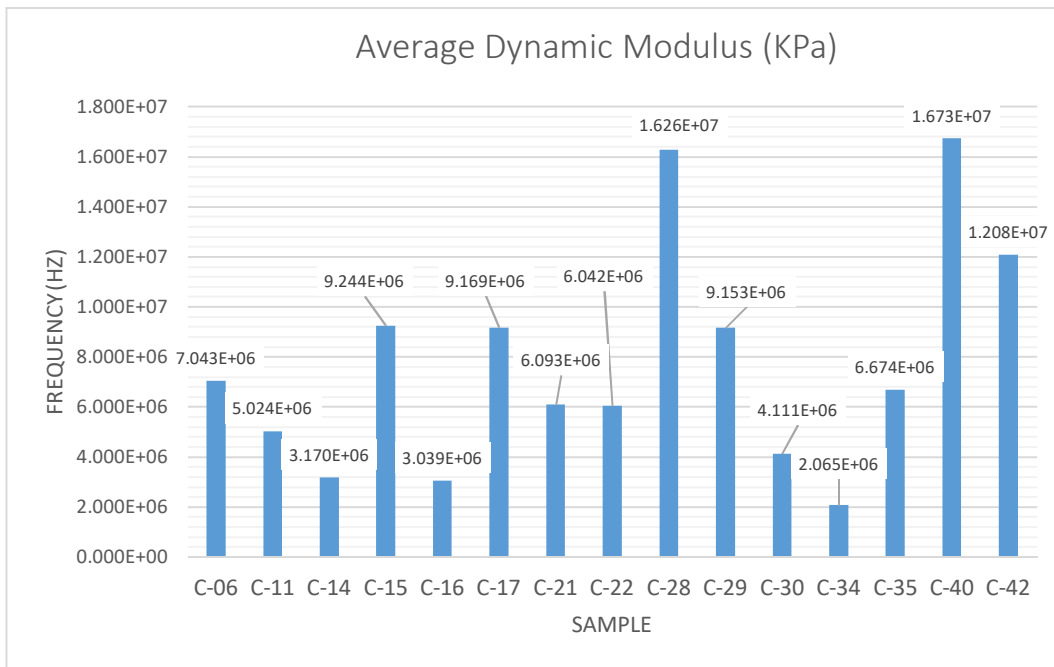


Figure 4-2: Dynamic Modulus per concrete cylinder sample calculated per ASTM C215.

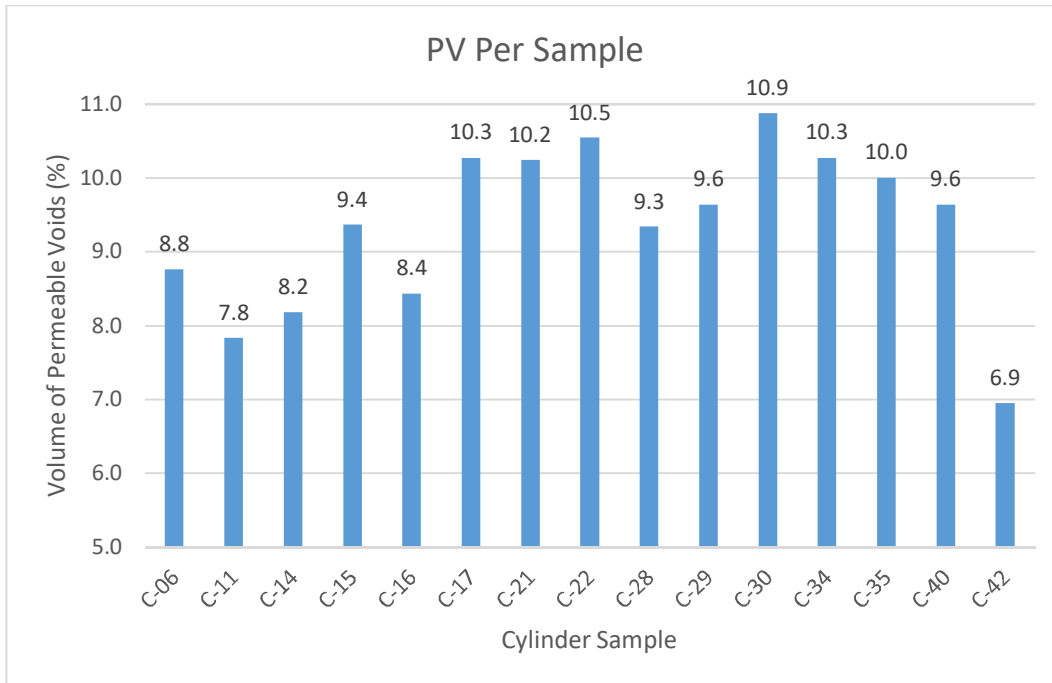


Figure 4-3: PV calculated per concrete sample according to ASTM C642.

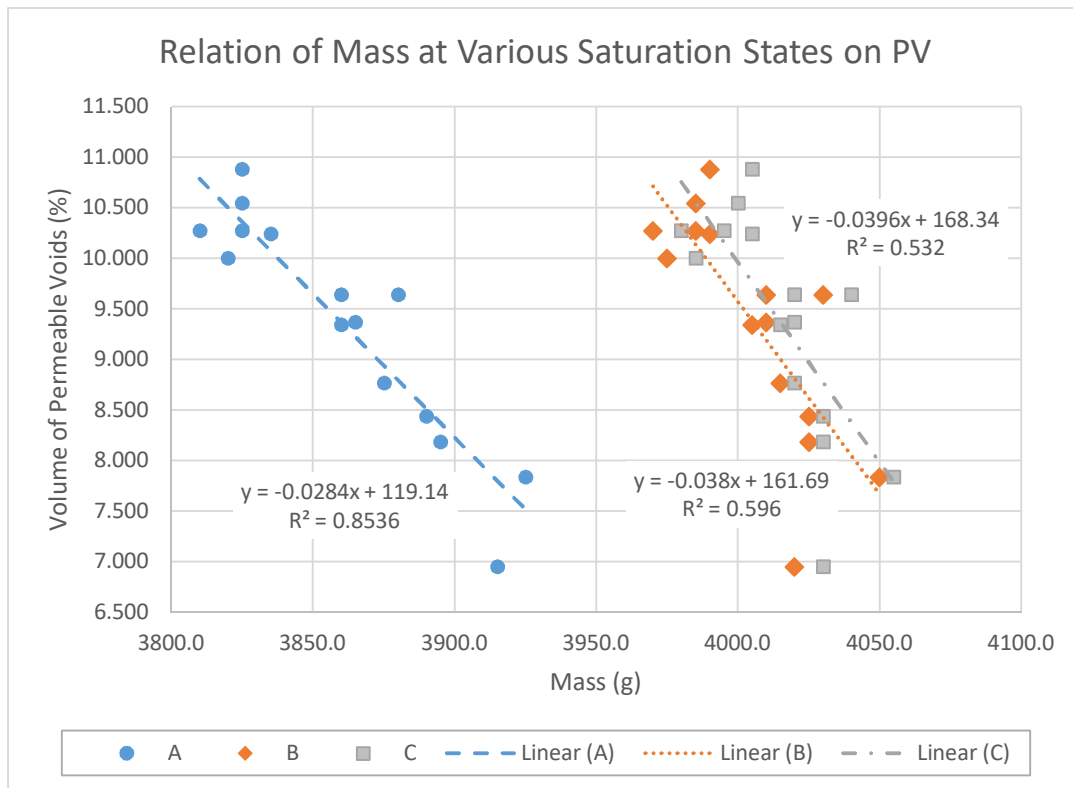


Figure 4-4: Oven-dried mass (A), saturated mass after immersion (B), saturated mass after boiling (C) for cylindrical samples.

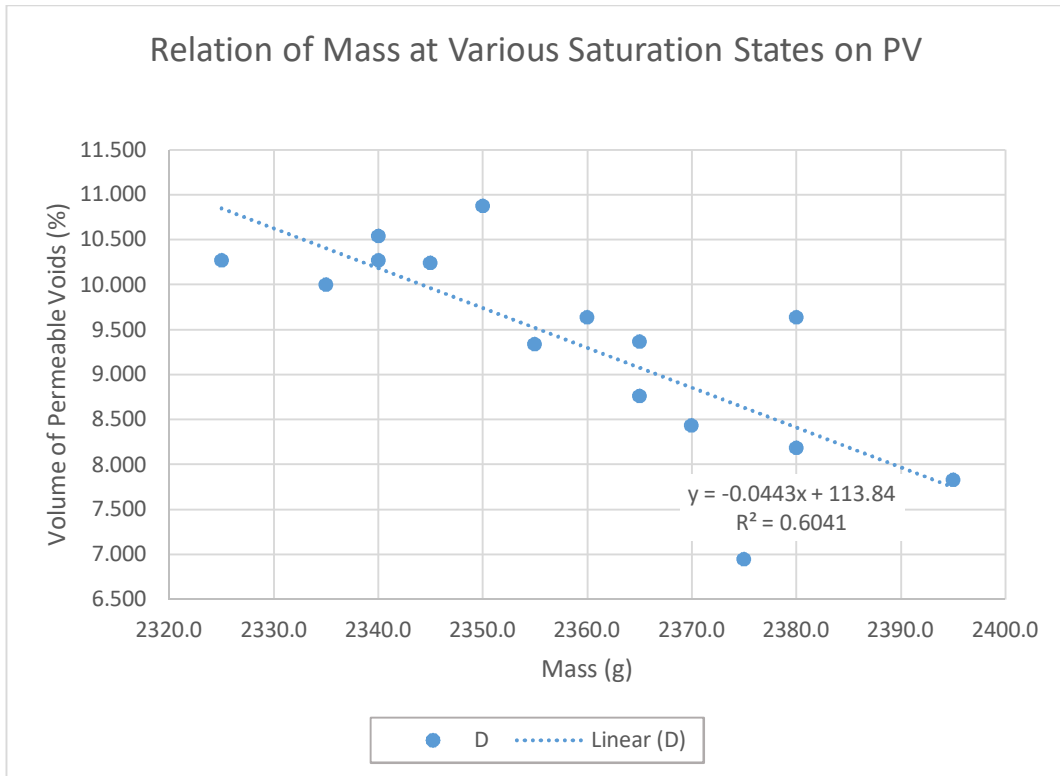


Figure 4-5: Immersed apparent mass (D) for cylindrical samples.

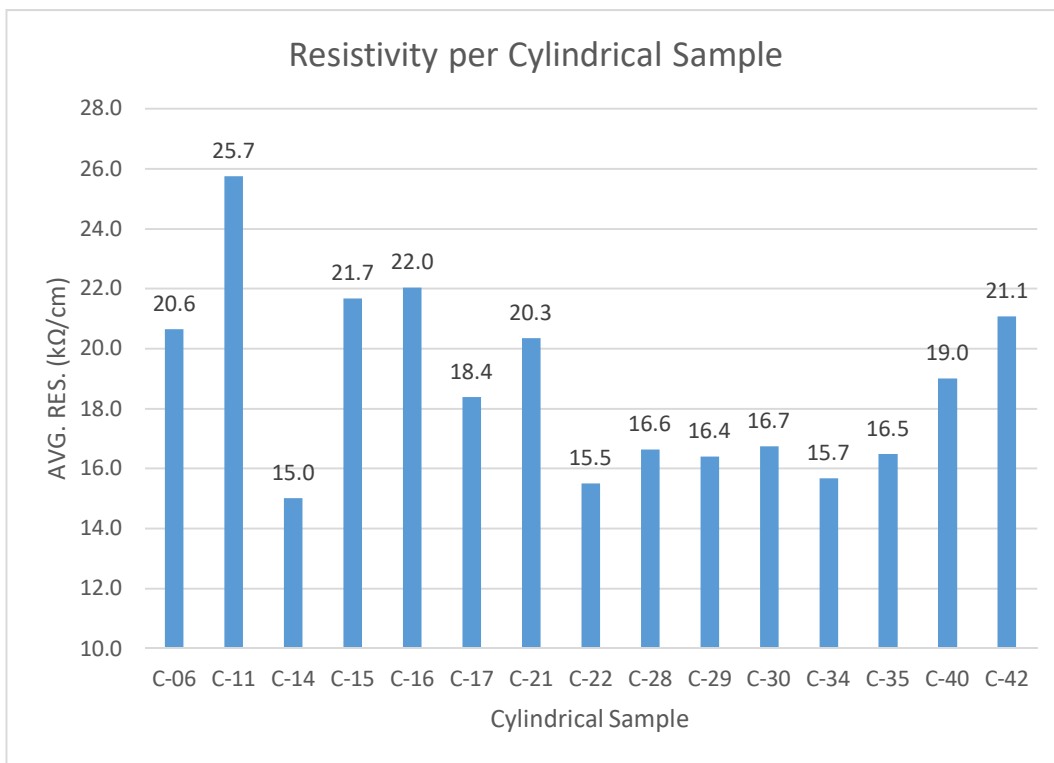


Figure 4-6: Average resistivity of each cylindrical sample calculated per Equation 4-6.

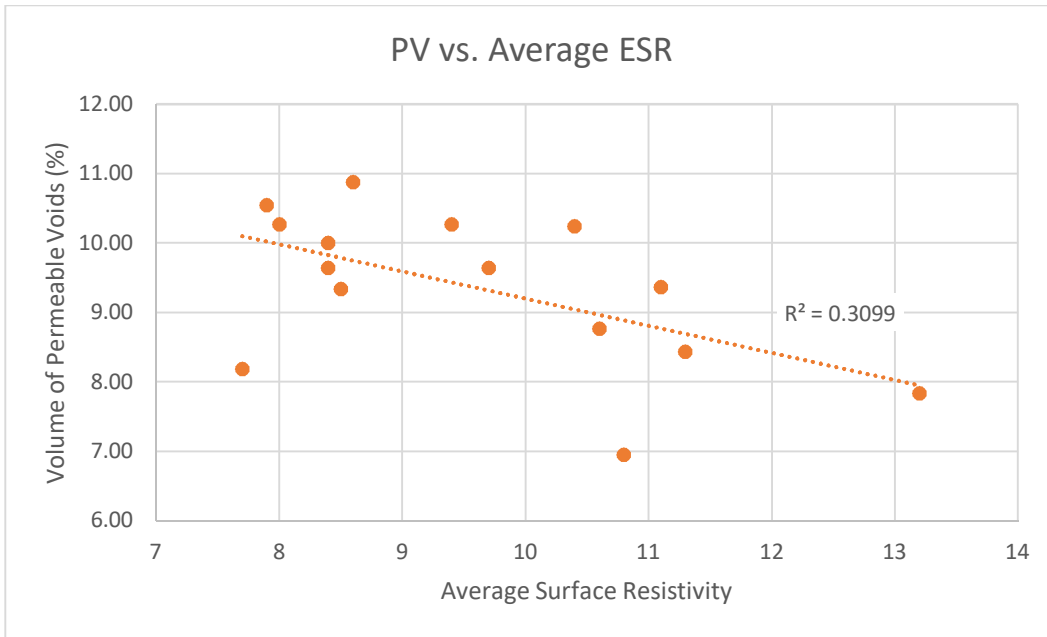


Figure 4-7: Holistic comparison between PV results obtained from ASTM C642 for water absorption and the average surface resistivity.

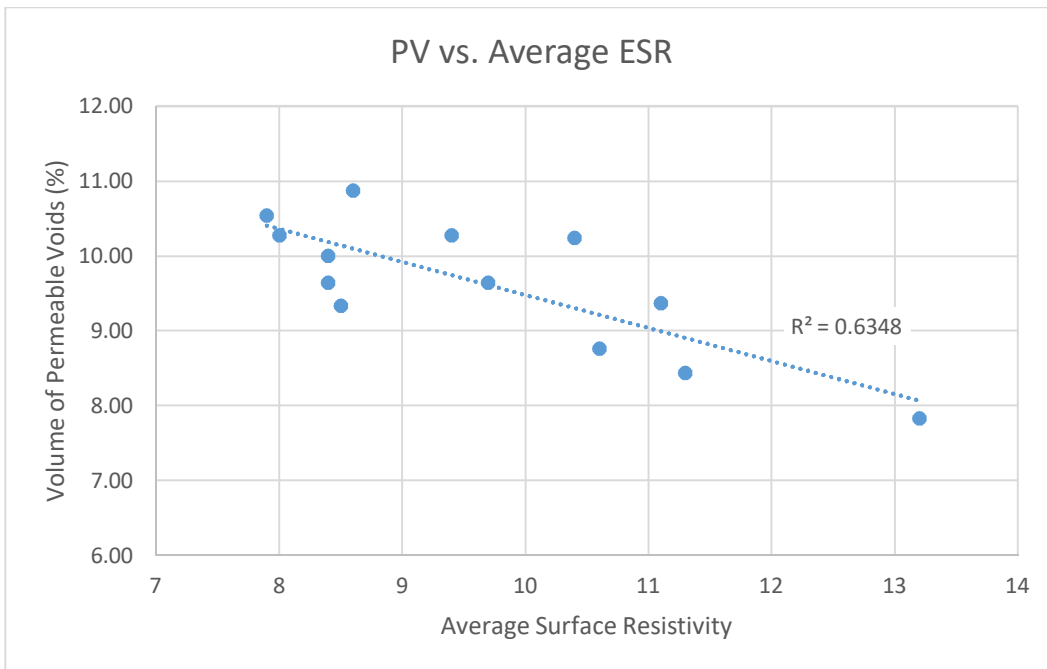


Figure 4-8: Comparison between PV results obtained from ASTM C642 for water absorption and the average surface resistivity, excluding two outliers.

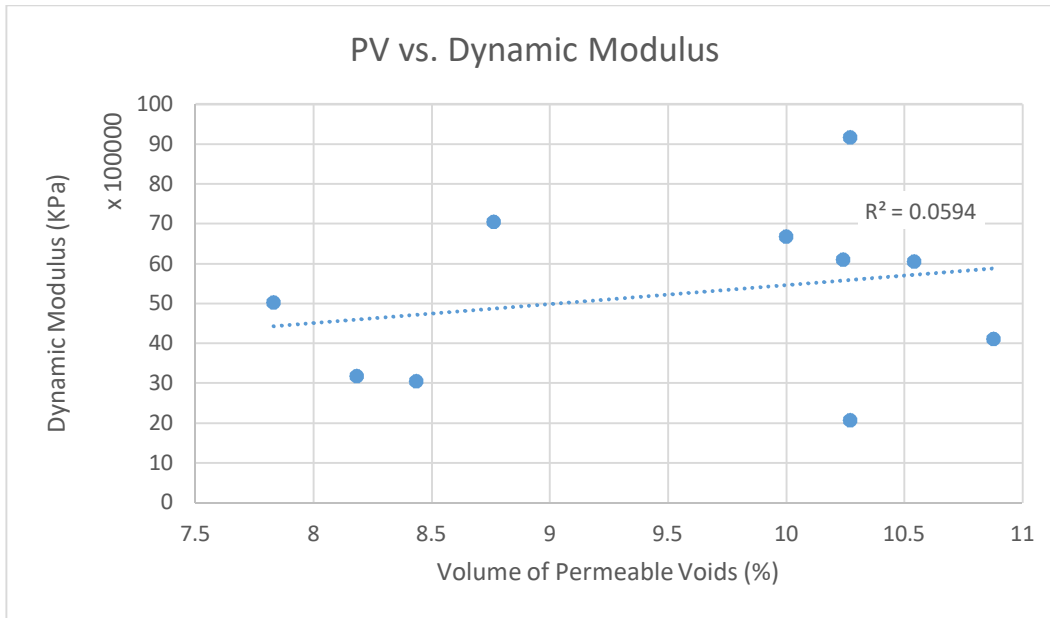


Figure 4-9: Consolidated data comparing PV obtained from ASTM C64, with the dynamic modulus obtained from ASTM C215

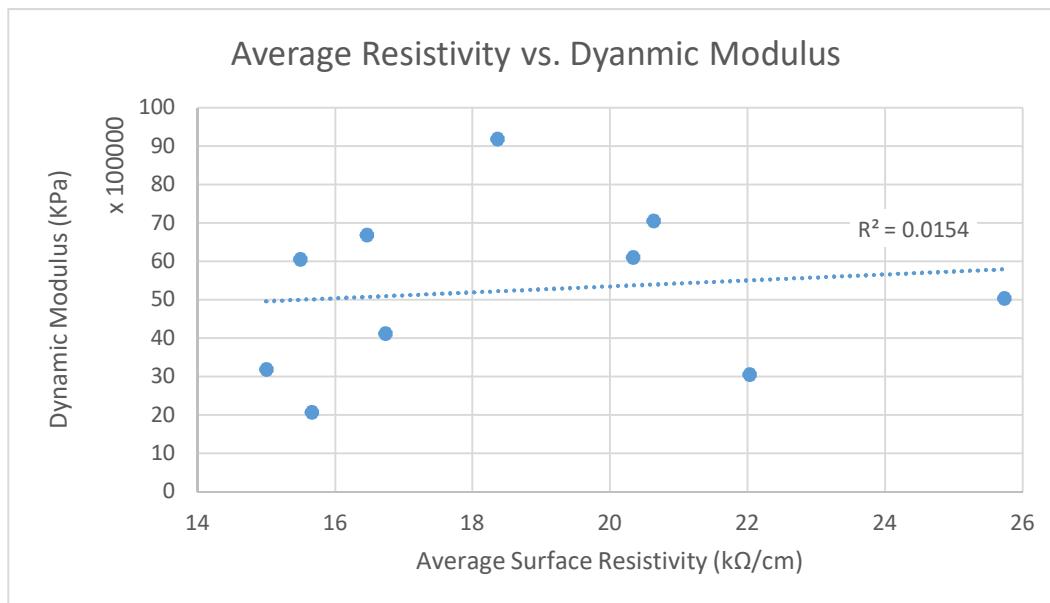


Figure 4-10: Consolidated data for comparison of the average surface resistivity and the dynamic modulus obtained from ASTM C215

Sample	M (kg.)	n (Hz)	L (m)	d (m)	K/L	T1	C1 (m ⁻¹)	E (ksi)	E (kPa)
C-06	3.858	2645	0.2032	0.1024	0.1260	2.129	260.878	1021.505	7.043E+06
C-11	3.914	2201	0.2032	0.1019	0.1254	2.118	264.943	728.610	5.024E+06
C-14	3.874	1773	0.2020	0.1021	0.1263	2.135	260.302	459.777	3.170E+06
C-15	3.893	3035	0.2019	0.1024	0.1268	2.142	257.856	1340.759	9.244E+06
C-16	3.883	1733	0.2020	0.1021	0.1263	2.134	260.514	440.769	3.039E+06
C-17	3.865	3008	0.2024	0.1020	0.1259	2.128	262.263	1329.891	9.169E+06
C-21	3.868	2456	0.2021	0.1020	0.1262	2.132	261.274	883.780	6.093E+06
C-22	3.868	2443	0.2027	0.1021	0.1260	2.128	261.822	876.354	6.042E+06
C-28	3.878	4014	0.2016	0.1020	0.1264	2.136	260.284	2358.212	1.626E+07
C-29	3.888	2989	0.2024	0.1018	0.1257	2.125	263.501	1327.523	9.153E+06
C-30	3.868	2019	0.2021	0.1021	0.1262	2.133	260.881	596.305	4.111E+06
C-34	3.846	1438	0.2016	0.1020	0.1265	2.137	259.746	299.445	2.065E+06
C-35	3.852	2581	0.2016	0.1020	0.1265	2.137	260.039	967.942	6.674E+06
C-40	3.906	4033	0.2021	0.1017	0.1258	2.126	263.301	2426.176	1.673E+07
C-42	3.903	3438	0.2011	0.1016	0.1263	2.134	261.851	1751.706	1.208E+07

Table 4-1: Holistic data for dynamic modulus results obtained from ASTM C215.

Sample	M (kg.)	n (Hz)	L (m)	d (m)	K/L	T1	C1 (m ⁻¹)	E (ksi)	E (kPa)
C-06	3.858	2645	0.203	0.1024	0.126	2.13	260.8775	1021.505482	7043032.07
C-11	3.914	2201	0.203	0.1019	0.125	2.12	264.9433	728.6096618	5023586.57
C-14	3.8741	1773	0.202	0.1021	0.126	2.13	260.3023	459.7771434	3170051.68
C-16	3.8827	1733	0.202	0.1021	0.126	2.13	260.5144	440.7688014	3038993.78
C-17	3.8653	3008	0.202	0.1020	0.126	2.13	262.2629	1329.891345	9169277.66
C-21	3.868	2456	0.202	0.1020	0.126	2.13	261.2744	883.7801733	6093449.54
C-22	3.8683	2443	0.203	0.1021	0.126	2.13	261.8216	876.3539926	6042247.83
C-30	3.868	2019	0.202	0.1021	0.126	2.13	260.8814	596.3045585	4111375.03
C-34	3.8457	1438	0.202	0.1020	0.127	2.14	259.7456	299.4451765	2064601.73
C-35	3.852	2581	0.202	0.1020	0.126	2.14	260.0391	967.9419189	6673724.32

Table 4-2: Consolidated data for dynamic modulus results obtained from ASTM C215.

SAMPLE	A (g)	B (g)	C (g)	D (g)
C-06	3875.0	4015.0	4020.0	2365.0
C-11	3925.0	4050.0	4055.0	2395.0
C-14	3895.0	4025.0	4030.0	2380.0
C-15	3865.0	4010.0	4020.0	2365.0
C-16	3890.0	4025.0	4030.0	2370.0
C-17	3825.0	3985.0	3995.0	2340.0
C-21	3835.0	3990.0	4005.0	2345.0
C-22	3825.0	3985.0	4000.0	2340.0
C-28	3860.0	4005.0	4015.0	2355.0
C-29	3860.0	4010.0	4020.0	2360.0
C-30	3825.0	3990.0	4005.0	2350.0
C-34	3810.0	3970.0	3980.0	2325.0
C-35	3820.0	3975.0	3985.0	2335.0
C-40	3880.0	4030.0	4040.0	2380.0
C-42	3915.0	4020.0	4030.0	2375.0

Table 4-3: Results for the cylinders tested per ASTM C642; Standard Test Method for Density, Absorption, and Voids in Hardened Concrete with; (A) the oven-dry mass, (B) the final surface-dry mass after immersion, (C) the soaked, boiled, surface-dried mass, (D) the apparent mass.

SAMPLE	Eqn.(8) (%)	Eqn.(9) (%)	$\frac{g1}{Eqn.(10)}$ (%)	Eqn.(11)	Eqn.(12)	$\frac{g2}{Eqn.(13)}$	Eqn.(14) (%)
C-06	3.613	3.742	2.341	2.426	2.429	2.566	8.761
C-11	3.185	3.312	2.364	2.440	2.443	2.565	7.831
C-14	3.338	3.466	2.361	2.439	2.442	2.571	8.182
C-15	3.752	4.010	2.335	2.423	2.429	2.577	9.366
C-16	3.470	3.599	2.343	2.425	2.428	2.559	8.434
C-17	4.183	4.444	2.3f11	2.408	2.414	2.576	10.272
C-21	4.042	4.433	2.310	2.404	2.413	2.574	10.241
C-22	4.183	4.575	2.304	2.401	2.410	2.576	10.542
C-28	3.756	4.016	2.325	2.413	2.419	2.565	9.337
C-29	3.886	4.145	2.325	2.416	2.422	2.573	9.639
C-30	4.314	4.706	2.311	2.411	2.420	2.593	10.876
C-34	4.199	4.462	2.302	2.399	2.405	2.566	10.272
C-35	4.058	4.319	2.315	2.409	2.415	2.572	10.000
C-40	3.866	4.124	2.337	2.428	2.434	2.587	9.639
C-42	2.682	2.937	2.366	2.429	2.435	2.542	6.949

Table 4-4: Results for the cylinders tested per ASTM C642; Standard Test Method for Density, Absorption, and Voids in Hardened Concrete with; Eqn. (8) absorption after immersion (%), Eqn. (9) absorption after immersion and boiling (%), Eqn. (10) bulk dry density (Mg/m³), Eqn. (11) bulk density after immersion (Mg/m³), Eqn. (12) bulk density after immersion and boiling (Mg/m³), Eqn. (13) apparent density (Mg/m³), and Eqn. (14) PV .

SAMPLE	A (g)	B (g)	C (g)	D (g)	SAMPLE	A (g)	B (g)	C (g)	D (g)
D-1B	870	905	910	525	D-8H	950	990	995	590
D-2B	895	930	940	545	D-9H	975	1015	1025	600
D-3B	835	865	870	510	D06-3	795	835	835	490
D-4B	870	915	920	525	D06-4	880	925	925	545
D-5B	890	920	925	540	D11-1	965	1015	1015	595
D-6B	865	905	910	525	D11-2	995	1040	1045	615
D-7B	890	930	935	545	D11-3	855	895	895	525
D-8B	975	1010	1015	595	D11-4	845	880	880	520
D-9B	920	955	960	560	D14-1	975	1025	1025	605
D-1C	875	910	920	535	D14-2	975	1025	1030	600
D-2C	945	975	985	575	D14-3	885	930	930	540
D-3C	860	895	905	520	D14-4	795	825	825	490
D-4C	905	935	945	550	D15-1	970	1015	1020	600
D-5C	920	950	955	550	D15-2	945	995	1000	580
D-6C	900	930	935	545	D15-3	855	890	895	525
D-7C	915	945	950	550	D15-4	845	875	880	520
D-8C	910	945	945	555	D16-1	960	1005	1010	590
D-9C	925	955	960	555	D16-2	975	1020	1020	600
D-1D	950	995	1005	585	D16-3	815	855	855	500
D-2D	945	990	995	585	D16-4	895	930	930	555
D-3D	925	980	985	575	D17-1	965	1010	1010	590
D-4D	840	875	880	525	D17-2	980	1025	1030	605
D-5D	900	935	940	555	D17-3	845	885	885	520
D-6D	950	990	995	590	D17-4	810	845	845	495
D-7D	980	1020	1030	605	D21-2	965	1010	1010	595
D-8D	970	1010	1015	600	D21-3	905	945	945	555
D-1E	895	935	945	545	D21-4	820	850	855	500
D-2E	880	915	920	535	D22-2	975	1020	1025	600
D-3E	870	910	915	520	D22-3	805	840	845	495
D-4E	915	960	965	555	D22-4	870	905	905	535
D-5E	880	920	925	530	D28-1	950	995	1000	585
D-6E	845	885	890	520	D28-2	950	1000	1005	590
D-7E	890	930	940	540	D28-3	895	930	935	545
D-8E	880	915	920	535	D28-4	790	820	820	485
D-9E	845	880	890	515	D29-1	980	1025	1030	605
D-1F	970	1010	1015	600	D29-2	970	1015	1020	600
D-2F	840	875	880	520	D29-3	830	870	870	510
D-3F	865	905	910	540	D29-4	840	875	880	515
D-4F	965	1005	1010	595	D30-1	935	980	985	580
D-5F	970	1010	1015	600	D30-2	975	1020	1025	600
D-6F	965	1010	1015	595	D30-3	800	845	845	490
D-7F	970	1010	1015	595	D30-4	890	930	930	550

D-8F	955	995	1000	590	D34-1	925	970	975	565
D-9F	935	970	975	575	D34-2	970	1015	1020	595
D-1G	870	905	910	530	D34-3	890	930	935	545
D-2G	855	895	905	525	D34-4	795	830	830	480
D-4G	895	930	940	550	D35-1	950	1000	1005	585
D-5G	895	930	940	545	D35-2	980	1025	1030	605
D-6G	860	895	905	525	D35-3	855	890	895	520
D-7G	900	935	940	545	D35-4	795	830	835	485
D-8G	870	905	915	525	D40-1	950	995	1000	585
D-9G	890	925	930	540	D40-2	985	1030	1035.5	610
D-1H	965	1010	1020	600	D40-3	840	880	885	510
D-2H	975	1015	1020	605	D40-4	865	900	905	525
D-3H	990	1025	1035	605	D42-1	975	1015	1020	605
D-4H	815	850	855	510	D42-2	985	1030	1030	610
D-5H	985	1020	1025	605	D42-3	850	890	895	515
D-6H	960	995	1000	585	D42-4	825	855	860	505
D-7H	985	1025	1030	610					

Table 4-5: Results for the disks tested per ASTM C642; Standard Test Method for Density, Absorption, and Voids in Hardened Concrete with; (A) the oven-dry mass, (B) the final surface-dry mass after immersion, (C) the soaked, boiled, surface-dried mass, (D) the apparent mass.

SAMPLE	g1			g2			Eqn.(14) (%)
	Eqn.(8) (%)	Eqn.(9) (%)	Eqn.(10) (%)	Eqn.(11)	Eqn.(12)	Eqn.(13)	
D-1B	4.023	4.598	2.260	2.351	2.364	2.522	10.390
D-2B	3.911	5.028	2.266	2.354	2.380	2.557	11.392
D-3B	3.593	4.192	2.319	2.403	2.417	2.569	9.722
D-4B	5.172	5.747	2.203	2.316	2.329	2.522	12.658
D-5B	3.371	3.933	2.312	2.390	2.403	2.543	9.091
D-6B	4.624	5.202	2.247	2.351	2.364	2.544	11.688
D-7B	4.494	5.056	2.282	2.385	2.397	2.580	11.538
D-8B	3.590	4.103	2.321	2.405	2.417	2.566	9.524
D-9B	3.804	4.348	2.300	2.388	2.400	2.556	10.000
D-1C	4.000	5.143	2.273	2.364	2.390	2.574	11.688
D-2C	3.175	4.233	2.305	2.378	2.402	2.554	9.756
D-3C	4.070	5.233	2.234	2.325	2.351	2.529	11.688
D-4C	3.315	4.420	2.291	2.367	2.392	2.549	10.127
D-5C	3.261	3.804	2.272	2.346	2.358	2.486	8.642
D-6C	3.333	3.889	2.308	2.385	2.397	2.535	8.974
D-7C	3.279	3.825	2.288	2.363	2.375	2.507	8.750
D-8C	3.846	3.846	2.333	2.423	2.423	2.563	8.974
D-9C	3.243	3.784	2.284	2.358	2.370	2.500	8.642
D-1D	4.737	5.789	2.262	2.369	2.393	2.603	13.095

D-2D	4.762	5.291	2.305	2.415	2.427	2.625	12.195
D-3D	5.946	6.486	2.256	2.390	2.402	2.643	14.634
D-4D	4.167	4.762	2.366	2.465	2.479	2.667	11.268
D-5D	3.889	4.444	2.338	2.429	2.442	2.609	10.390
D-6D	4.211	4.737	2.346	2.444	2.457	2.639	11.111
D-7D	4.082	5.102	2.306	2.400	2.424	2.613	11.765
D-8D	4.124	4.639	2.337	2.434	2.446	2.622	10.843
D-1E	4.469	5.587	2.238	2.338	2.363	2.557	12.500
D-2E	3.977	4.545	2.286	2.377	2.390	2.551	10.390
D-3E	4.598	5.172	2.203	2.304	2.316	2.486	11.392
D-4E	4.918	5.464	2.232	2.341	2.354	2.542	12.195
D-5E	4.545	5.114	2.228	2.329	2.342	2.514	11.392
D-6E	4.734	5.325	2.284	2.392	2.405	2.600	12.162
D-7E	4.494	5.618	2.225	2.325	2.350	2.543	12.500
D-8E	3.977	4.545	2.286	2.377	2.390	2.551	10.390
D-9E	4.142	5.325	2.253	2.347	2.373	2.561	12.000
D-1F	4.124	4.639	2.337	2.434	2.446	2.622	10.843
D-2F	4.167	4.762	2.333	2.431	2.444	2.625	11.111
D-3F	4.624	5.202	2.338	2.446	2.459	2.662	12.162
D-4F	4.145	4.663	2.325	2.422	2.434	2.608	10.843
D-5F	4.124	4.639	2.337	2.434	2.446	2.622	10.843
D-6F	4.663	5.181	2.298	2.405	2.417	2.608	11.905
D-7F	4.124	4.639	2.310	2.405	2.417	2.587	10.714
D-8F	4.188	4.712	2.329	2.427	2.439	2.616	10.976
D-9F	3.743	4.278	2.338	2.425	2.438	2.597	10.000
D-1G	4.023	4.598	2.289	2.382	2.395	2.559	10.526
D-2G	4.678	5.848	2.250	2.355	2.382	2.591	13.158
D-4G	3.911	5.028	2.295	2.385	2.410	2.594	11.538
D-5G	3.911	5.028	2.266	2.354	2.380	2.557	11.392
D-6G	4.070	5.233	2.263	2.355	2.382	2.567	11.842
D-7G	3.889	4.444	2.278	2.367	2.380	2.535	10.127
D-8G	4.023	5.172	2.231	2.321	2.346	2.522	11.538
D-9G	3.933	4.494	2.282	2.372	2.385	2.543	10.256
D-1H	4.663	5.699	2.298	2.405	2.429	2.644	13.095
D-2H	4.103	4.615	2.349	2.446	2.458	2.635	10.843
D-3H	3.535	4.545	2.302	2.384	2.407	2.571	10.465
D-4H	4.294	4.908	2.362	2.464	2.478	2.672	11.594
D-5H	3.553	4.061	2.345	2.429	2.440	2.592	9.524
D-6H	3.646	4.167	2.313	2.398	2.410	2.560	9.639
D-7H	4.061	4.569	2.345	2.440	2.452	2.627	10.714
D-8H	4.211	4.737	2.346	2.444	2.457	2.639	11.111
D-9H	4.103	5.128	2.294	2.388	2.412	2.600	11.765
D06-3	5.031	5.031	2.304	2.420	2.420	2.607	11.594

D06-4	5.114	5.114	2.316	2.434	2.434	2.627	11.842
D11-1	5.181	5.181	2.298	2.417	2.417	2.608	11.905
D11-2	4.523	5.025	2.314	2.419	2.430	2.618	11.628
D11-3	4.678	4.678	2.311	2.419	2.419	2.591	10.811
D11-4	4.142	4.142	2.347	2.444	2.444	2.600	9.722
D14-1	5.128	5.128	2.321	2.440	2.440	2.635	11.905
D14-2	5.128	5.641	2.267	2.384	2.395	2.600	12.791
D14-3	5.085	5.085	2.269	2.385	2.385	2.565	11.538
D14-4	3.774	3.774	2.373	2.463	2.463	2.607	8.955
D15-1	4.639	5.155	2.310	2.417	2.429	2.622	11.905
D15-2	5.291	5.820	2.250	2.369	2.381	2.589	13.095
D15-3	4.094	4.678	2.311	2.405	2.419	2.591	10.811
D15-4	3.550	4.142	2.347	2.431	2.444	2.600	9.722
D16-1	4.687	5.208	2.286	2.393	2.405	2.595	11.905
D16-2	4.615	4.615	2.321	2.429	2.429	2.600	10.714
D16-3	4.908	4.908	2.296	2.408	2.408	2.587	11.268
D16-4	3.911	3.911	2.387	2.480	2.480	2.632	9.333
D17-1	4.663	4.663	2.298	2.405	2.405	2.573	10.714
D17-2	4.592	5.102	2.306	2.412	2.424	2.613	11.765
D17-3	4.734	4.734	2.315	2.425	2.425	2.600	10.959
D17-4	4.321	4.321	2.314	2.414	2.414	2.571	10.000
D21-2	4.663	4.663	2.325	2.434	2.434	2.608	10.843
D21-3	4.420	4.420	2.321	2.423	2.423	2.586	10.256
D21-4	3.659	4.268	2.310	2.394	2.408	2.563	9.859
D22-2	4.615	5.128	2.294	2.400	2.412	2.600	11.765
D22-3	4.348	4.969	2.300	2.400	2.414	2.597	11.429
D22-4	4.023	4.023	2.351	2.446	2.446	2.597	9.459
D28-1	4.737	5.263	2.289	2.398	2.410	2.603	12.048
D28-2	5.263	5.789	2.289	2.410	2.422	2.639	13.253
D28-3	3.911	4.469	2.295	2.385	2.397	2.557	10.256
D28-4	3.797	3.797	2.358	2.448	2.448	2.590	8.955
D29-1	4.592	5.102	2.306	2.412	2.424	2.613	11.765
D29-2	4.639	5.155	2.310	2.417	2.429	2.622	11.905
D29-3	4.819	4.819	2.306	2.417	2.417	2.594	11.111
D29-4	4.167	4.762	2.301	2.397	2.411	2.585	10.959
D30-1	4.813	5.348	2.309	2.420	2.432	2.634	12.346
D30-2	4.615	5.128	2.294	2.400	2.412	2.600	11.765
D30-3	5.625	5.625	2.254	2.380	2.380	2.581	12.676
D30-4	4.494	4.494	2.342	2.447	2.447	2.618	10.526
D34-1	4.865	5.405	2.256	2.366	2.378	2.569	12.195
D34-2	4.639	5.155	2.282	2.388	2.400	2.587	11.765
D34-3	4.494	5.056	2.282	2.385	2.397	2.580	11.538
D34-4	4.403	4.403	2.271	2.371	2.371	2.524	10.000

D35-1	5.263	5.789	2.262	2.381	2.393	2.603	13.095
D35-2	4.592	5.102	2.306	2.412	2.424	2.613	11.765
D35-3	4.094	4.678	2.280	2.373	2.387	2.552	10.667
D35-4	4.403	5.031	2.271	2.371	2.386	2.565	11.429
D40-1	4.737	5.263	2.289	2.398	2.410	2.603	12.048
D40-2	4.569	5.127	2.315	2.421	2.434	2.627	11.868
D40-3	4.762	5.357	2.240	2.347	2.360	2.545	12.000
D40-4	4.046	4.624	2.276	2.368	2.382	2.544	10.526
D42-1	4.103	4.615	2.349	2.446	2.458	2.635	10.843
D42-2	4.569	4.569	2.345	2.452	2.452	2.627	10.714
D42-3	4.706	5.294	2.237	2.342	2.355	2.537	11.842
D42-4	3.636	4.242	2.324	2.408	2.423	2.578	9.859

Table 4-6: Result for the disks tested per ASTM C642; Standard Test Method for Density, Absorption, and Voids in Hardened Concrete with; Eqn. (8) absorption after immersion (%), Eqn. (9) absorption after immersion and boiling (%), Eqn. (10) bulk dry density (Mg/m³), Eqn. (11) bulk density after immersion (Mg/m³), Eqn. (12) bulk density after immersion and boiling (Mg/m³), Eqn. (13) apparent density (Mg/m³), and Eqn. (14) PV

SPECIMEN ID	AVG. SURFACE RES. (kΩ/cm)	AVG. RES. (kΩ/cm)	Chloride Penetration
C-06	10.6	20.63	Moderate
C-11	13.2	25.73	Moderate
C-14	7.7	15.00	High
C-15	11.1	21.67	Moderate
C-16	11.3	22.03	Moderate
C-17	9.4	18.37	High
C-21	10.4	20.33	Moderate
C-22	7.9	15.50	High
C-28	8.5	16.63	High
C-29	8.4	16.40	High
C-30	8.6	16.73	High
C-34	8.0	15.67	High
C-35	8.4	16.47	High
C-40	9.7	19.00	High
C-42	10.8	21.07	Moderate

Table 4-7: Results of the SurfTM testing. Average ESR (KΩ/cm), average surface resistance and corresponding chloride penetrability

$$\text{Dynamic } E = CMn^2$$

Equation 4-1: Formula for calculating the dynamic modulus (E); where C is the geometrical factor, M is the mass (kg), and n is the fundamental transverse frequency (Hz) (ASTM C215, p.5).

$$C = 1.6067 \frac{L^3 T}{d^4}$$

Equation 4-2: Geometrical correction factor (C); where L is the length of the specimen (m), T is the correction factor dependent on the radius of gyration (K), and d is the diameter (m) (ASTM C215, p.5).

$$K = d/4$$

Equation 4-3: Radius of gyration (K) for a cylinder; where d is the diameter (m) (ASTM C215, p.5).

$$PV(\%) = \left(\frac{g_2 - g_1}{g_2} \right) * 100$$

Equation 4-4: PV (ASTM C642)

$$\rho = 2\pi a \frac{V}{I}$$

Equation 4-5: ESR for semi-infinite, homogeneous concrete; where a is the distance between the equally spaced electrodes, V is the voltage, and I is the current (Giatec Scientific, p.7).

$$\rho = kR$$

Equation 4-6: Where ρ is the resistivity, k is the geometrical factor, and R is the measured resistance.

$$g_1 = \left(\frac{A}{C - D} \right) \rho$$

Equation 4-7: Bulk density-dry (g_1) where; A is the oven-dried mass (g), C is the saturated mass after boiling (g), D is the immersed apparent mass (g), and ρ is the density of water (g/cm^3)

$$g_2 = \left(\frac{A}{A - D} \right) \rho$$

Equation 4-8: Apparent density (g_2) where; A is the oven-dried mass (g), D is the immersed apparent mass (g), and ρ is the density of water (g/cm^3)

$$PV = \left(\frac{g_2 - g_1}{g_2} \right) \times 100$$

Equation 4-9: PV where; g_1 is the bulk density-dry, and g_2 is the apparent density per ASTM C642.

5 Conclusion

5.1 Summary

Currently there is no efficient way of measuring the deterioration of the concrete in bridge decks. The existing standard tests such as, ASTM C215, ASTM C1202, and ESR, are mainly for measuring the deterioration of concrete samples in laboratories. Meanwhile, some of these tests have disadvantages. Specifically, some tests take too long and cause permeant damage to the concrete, or make testing of field samples difficult. Alternatively, water absorption, which has been shown in Lin et al. (2012) to relate to the amount of charge passed in RCIP testing, could be used to determine the durability of concrete. Several concerns were identified with the previous study by Lin et al. (2012), therefore, the claim that water absorption is related to the durability of concrete, specifically mechanically loaded F/T concrete, needed further validation.

To provide supporting evidence for the relationship between water absorption and concrete durability, fifteen cylinders were tested for dynamic modulus, water absorption and ESR. These cylinders were previously exposed to compressive stresses of varying percentages of f'_c and varying numbers of F/T cycles. The specific compressive stresses and number of F/T cycles per sample is unknown and the study is therefore blind. Setting up the experiment in such a way eliminates any possible bias from the obtained results.

The cylinders tested for dynamic modulus using the contact driven forced resonance method (ASTM C215, 1). A driving unit forced vibrations ranging from 1k through 10k hertz through the samples. The vibrations were measured by an accelerometer which was mounted at the end of the samples. The dynamic modulus was calculated using the peak frequency at which the cylinders resonated, as indicated by the highest output reading on the needle indicator.

The concrete cylinders were tested for absorption per ASTM 642. The oven-dried mass (A) was determined after the samples were oven-dried for a period of 24 hours and sequentially cooled by natural heat loss to 25°C (77°F). The cylinders were soaked in water for a period of 48 hours after which the mass after immersion (B) was recorded. The cylinders were boiled for five hours and subsequently cooled for no less than fourteen hours. The saturated mass after boiling mass (C) was recorded. The samples were placed in a metal basket suspended in water by a chain secured around the top plate of a scale. The mass of the samples was recorded as the immersed apparent mass (D). PV was calculated from the bulk-dry density and the apparent density. Linear regression analysis was used to determine the relationship of each mass recorded at various saturation states (e.g. A, B, C, D) to the resulting PV and to determine general best fit equations.

The ESR of the concrete samples was determined using a SURF™ testing apparatus which consisted of a chamber and data acquisition system. The average surface resistivity was calculated by taking the average of 24 surface resistance measurements and multiplying by a geometrical factor.

5.2 Results

Based on the limited tests conducted in this study, the following observations can be made:

1. ASTM C1202 was not conducted on the samples, however, the results obtained from ESR testing can provide an indication of what results may be expected from RCIP tests, (related by table Figure 3-9). All the concrete cylinder samples had moderate to high chloride penetration.

2. A relationship between the dynamic modulus and ESR; and dynamic modulus and PV could not be determined. It is possible that a larger population size could more accurately reflect the behavior of these variables in relation to dynamic modulus.
3. Linear regression and general equations were generated (see Figure 4-4 and Figure 4-5) from the absorption tests. Others (researching mechanically loaded F/T concrete) may find this information useful to check their own preliminary results. Caution should be exercised, however, due to the small population size of the study.
4. The oven-dried mass (A) and the apparent mass (D) had the strongest relationship to PV as indicated by R^2 of 85.4% and 60.4%, respectively.
5. Excluding the two outliers, a very strong relationship, with R^2 equal to 63.5%, was identified between VP and ESR. This clearly reinforces the original claim made by Lin et al. (2012) that water absorption is related to concrete durability.

5.3 Further Research

The observations and conclusions from this study should be further verified in future studies. Specifically;

1. Absorption tests should be carried out on concrete extracted from actual bridge deck to further examine the effects of overweight vehicles on the early deterioration of bridge deck.
2. The relationship between ESR, dynamic modulus, and water absorption should be examined with a larger population size.
3. Water absorption should be compared to tests for RCIP, another generally accepted test for the durability of concrete.

The design of concrete bridges is primarily focused on strength characteristics. However, it is often the case that durability characteristics, specifically early deterioration of the bridge deck, requires expensive repairs before the designed service life of the bridge can come to term. Water absorption, which is relatively quicker and has no restrictions on specimen size, could be used to determine the damage to bridge deck cause by overweight vehicles. Hopefully, if more is known about the relationship between early bridge deck deterioration and overweight vehicles, then policy change regarding the cost of overweight vehicle permits could be enacted.

6 References

- Arezoumandi. (2015). Feasibility of crack free reinforced concrete bridge deck from materials composition perspective: a state of the art review. *Frontiers of Structural and Civil Engineering*, 9(1), 91–103. doi:10.1007/s11709-015-0274-1
- ASTM C215. *Standard Test Method for Fundamental Transverse, Longitudinal, and Torsional Resonant Frequencies of Concrete*. (ASTM C215).
- ASTM C469. *Standard Test Method for Static Modulus of Elasticity and Poisson's Ratio of Concrete in Compression*. (ASTM C469).
- ASTM C642. *Standard Test Method for Density, Absorption, and Voids in Hardened Concrete*. (ASTM C642).
- ElSafty et al. (2013). Investigation of Likelihood of Cracking in Reinforced Concrete Bridge Decks. *International Journal of Concrete Structures and Materials*, 7(1), 79–93. doi:10.1007/s40069-013-0034-3
- Elzafraney et al. (2005). Quantitative Microstructural Investigation of Deteriorated Reinforced Concrete Bridge Deck. *Journal of Materials in Civil Engineering*, 17(2), 159–167. doi:10.1061/(ASCE)0899-1561(2005)17:2(159)
- Giatec Scientific. Surf User Manual: Surface Resistivity of Concrete Using Weener Four-Electrode Method.
- Hoseini et al. (2009). The effect of mechanical stress on permeability of concrete: A review. *Cement and Concrete Composites*, 31(4), 213–220. doi:10.1016/j.cemconcomp.2009.02.003
- Ishida. (2016). Ecological Durability Design for RC Bridge Deck in Cold Regions, 1–9. Retrieved from https://www.researchgate.net/publication/310440380_ECOLOGICAL_DURABILITY_DESIGN_FOR_RC_BRIDGE_DECK_IN_COLD_REGIONS
- Layssi et al. (2015). Electrical Resistivity of Concrete: Concepts, Applications, and Measurement Techniques, 41–46.
- Lin et al. (2012). *Impact of Overweight Vehicles: With Heavy Axle Loads on Bridge Deck Deterioration*. Milwaukee, WI.
- Mehta et al. (Ed.). (2006). *Concrete: Microstructure, Properties, and Materials* (Third Edition): McGraw-Hill.
- Rhee et al. (2009). An Experimental Study for Improving the Durability of Concrete Bridge Decks, 1–11. Retrieved from https://www.researchgate.net/publication/299621044_AN_EXPERIMENTAL_STUDY_FOR_IMPROVING_THE_DURABILITY_OF_CONCRETE_BRIDGE_DECKS
- Shiotani et al. (2012). Damage Evaluation for Concrete Bridge Deck by Means of Stress Wave Techniques. *Journal of Bridge Engineering*, 17(6), 847–856. doi:10.1061/(ASCE)BE.1943-5592.0000373
- WisDOT. (2005). OVERSIZE/OVERWEIGHT SINGLE TRIP PERMIT INFORMATION. Retrieved from <http://wisconsindot.gov/Documents/formdocs/mv2600.pdf>
- Yang et al. (2006). Water Transport in Concrete Damaged by Tensile Loading and Freeze–Thaw Cycling. *Journal of Materials in Civil Engineering*, 18(3), 424–434. doi:10.1061/(ASCE)0899-1561(2006)18:3(424)

7 Appendix

7.1 ESR Figures

Test Description

Title: C-06

Date: 2016-11-20 - 21:18:57 PM

Test Method: ASTM WK378980

Operator: BDM

Source of Cylinder: C-06

Description:

Displayed Resistivity: kOhm.cm

Electrode Spacing: 3.8 cm - 1.5 inch

Cylinder Size: Cylinder 100 mm x 200 mm

Sample	CH 1 0 deg.	CH 2 90 deg.	CH 3 180 deg.	CH 4 270 deg.	CH 1 0 deg.	CH 2 90 deg.	CH 3 180 deg.	CH 4 270 deg.	Average
A	23.6	18.6	20.6	21.5	23.7	18.6	20.6	21.5	21.1
B	20.5	20.7	21.5	19.6	20.5	20.8	21.5	19.5	20.6
C	17.6	19.1	21	23.3	17.6	19.1	21	23.2	20.2

Average Resistivity: 20.6

20.63

Geometry Correction Conversion Factor: 1.95

Surface Resistivity: 10.6

Penetrability Based on Test: Moderate

Figure 7-1: Electric Resistivity of sample C-06

Test Description

Title: C-11

Date: 2016-11-08 - 16:19:47 PM

Test Method: ASTM WK378980

Operator: BDM

Source of Cylinder: C-11

Description:

Displayed Resistivity: kOhm.cm

Electrode Spacing: 3.8 cm - 1.5 inch

Cylinder Size: Cylinder 100 mm x 200 mm

Sample	CH 1 0 deg.	CH 2 90 deg.	CH 3 180 deg.	CH 4 270 deg.	CH 1 0 deg.	CH 2 90 deg.	CH 3 180 deg.	CH 4 270 deg.	Average
A	21.8	63.5	20.9	22.5	21.8	61.1	20.9	22.6	31.9
B	22.9	24.1	22.2	21.3	22.9	23.9	22.2	21.3	22.6
C	21.5	22.6	22.8	23.8	21.5	22.7	22.8	23.8	22.7
Average Resistivity: 25.7									25.73
Geometry Correction Conversion Factor: 1.95									
Surface Resistivity: 13.2									
Penetrability Based on Test: Moderate									

Figure 7-2: Electric Resistivity of sample C-11

Test Description

Title: C-14

Date: 2016-11-08 - 15:12:56 PM

Test Method: ASTM WK378980

Operator: BDM

Source of Cylinder: C-14

Description:

Displayed Resistivity: kOhm.cm

Electrode Spacing: 3.8 cm - 1.5 inch

Cylinder Size: Cylinder 100 mm x 200 mm

Sample	CH 1 0 deg.	CH 2 90 deg.	CH 3 180 deg.	CH 4 270 deg.	CH 1 0 deg.	CH 2 90 deg.	CH 3 180 deg.	CH 4 270 deg.	Average
A	17.4	14	13.9	13.3	17.5	14	13.9	13.3	14.7
B	15.2	14.9	15.2	16.3	15.2	15	15.1	16.3	15.4
C	15	15.2	14.1	15.3	15	15.2	14.1	15.3	14.9
Average Resistivity: 15.0									15.00
Geometry Correction Conversion Factor: 1.95									
Surface Resistivity: 7.7									
Penetrability Based on Test: High									

Figure 7-3: Electric Resistivity of sample C-14

Test Description

Title: C-15
Date: 2016-11-08 - 15:17:12 PM
Test Method: ASTM WK378980
Operator: BDM
Source of Cylinder: C-15
Description:

Displayed Resistivity: kOhm.cm
Electrode Spacing: 3.8 cm - 1.5 inch
Cylinder Size: Cylinder 100 mm x 200 mm

Sample	CH 1 0 deg.	CH 2 90 deg.	CH 3 180 deg.	CH 4 270 deg.	CH 1 0 deg.	CH 2 90 deg.	CH 3 180 deg.	CH 4 270 deg.	Average
A	19.6	23.8	18.4	25	19.5	23.7	18.5	25	21.7
B	22	22.1	20.4	22.2	21.9	22.1	20.4	22.2	21.7
C	22.5	18.6	24.5	20.8	22.5	18.6	24.5	20.9	21.6
Average Resistivity: 21.7									21.67
Geometry Correction Conversion Factor: 1.95									
Surface Resistivity: 11.1									
Penetrability Based on Test: Moderate									

Figure 7-4: Electric Resistivity of sample C-15

Test Description

Title: C-16
Date: 2016-11-20 - 21:28:51 PM
Test Method: ASTM WK378980
Operator: BDM
Source of Cylinder: C-16
Description:

Displayed Resistivity: kOhm.cm
Electrode Spacing: 3.8 cm - 1.5 inch
Cylinder Size: Cylinder 100 mm x 200 mm

Sample	CH 1 0 deg.	CH 2 90 deg.	CH 3 180 deg.	CH 4 270 deg.	CH 1 0 deg.	CH 2 90 deg.	CH 3 180 deg.	CH 4 270 deg.	Average
A	22.2	21.6	19.9	24.1	22.2	21.6	19.9	24.1	22
B	21.8	23.2	21.7	21.8	21.8	23.2	21.7	21.8	22.1
C	20.9	22.1	22.6	22.4	20.9	22	22.5	22.5	22
Average Resistivity: 22.0									22.03
Geometry Correction Conversion Factor: 1.95									
Surface Resistivity: 11.3									
Penetrability Based on Test: Moderate									

Figure 7-5: Electric Resistivity of sample C-16.

Test Description

Title: C-17
Date: 2016-11-23 - 09:21:42 AM
Test Method: ASTM WK378980
Operator: BDM
Source of Cylinder: C-17
Description:

Displayed Resistivity: kOhm.cm
Electrode Spacing: 3.8 cm - 1.5 inch
Cylinder Size: Cylinder 100 mm x 200 mm

Sample	CH 1 0 deg.	CH 2 90 deg.	CH 3 180 deg.	CH 4 270 deg.	CH 1 0 deg.	CH 2 90 deg.	CH 3 180 deg.	CH 4 270 deg.	Average
A	17.7	21.8	16	17.2	17.7	21.8	16	17.2	18.2
B	16.7	18.5	20	18.6	16.7	18.5	20	18.6	18.5
C	18.6	20.5	18.2	16.2	18.6	20.7	18.2	16.2	18.4
Average Resistivity: 18.3									18.37
Geometry Correction Conversion Factor: 1.95									
Surface Resistivity: 9.4									
Penetrability Based on Test: High									

Figure 7-6: Electric Resistivity of sample C-17

Test Description

Title: C-21
Date: 2016-11-08 - 16:24:13 PM
Test Method: ASTM WK378980
Operator: BDM
Source of Cylinder: C-21
Description:

Displayed Resistivity: kOhm.cm
Electrode Spacing: 3.8 cm - 1.5 inch
Cylinder Size: Cylinder 100 mm x 200 mm

Sample	CH 1 0 deg.	CH 2 90 deg.	CH 3 180 deg.	CH 4 270 deg.	CH 1 0 deg.	CH 2 90 deg.	CH 3 180 deg.	CH 4 270 deg.	Average
A	20.3	19.6	21.8	19.7	20.3	19.7	21.8	19.7	20.4
B	22.3	20.2	19.6	21.8	22.3	20.2	19.7	21.8	21
C	19.4	20.7	18.5	19.6	19.4	20.7	18.5	19.6	19.6
Average Resistivity: 20.3									20.33
Geometry Correction Conversion Factor: 1.95									
Surface Resistivity: 10.4									
Penetrability Based on Test: Moderate									

Figure 7-7: Electric Resistivity of sample C-21

Test Description

Title: C-22
Date: 2016-11-23 - 09:14:44 AM
Test Method: ASTM WK378980
Operator: BDM
Source of Cylinder: C-22
Description:

Displayed Resistivity: kOhm.cm
Electrode Spacing: 3.8 cm - 1.5 inch
Cylinder Size: Cylinder 100 mm x 200 mm

Sample	CH 1 0 deg.	CH 2 90 deg.	CH 3 180 deg.	CH 4 270 deg.	CH 1 0 deg.	CH 2 90 deg.	CH 3 180 deg.	CH 4 270 deg.	Average
A	15.1	16.6	15.2	16.1	15.1	16.7	15.2	16.1	15.8
B	14.8	15.7	13.8	14.9	14.8	15.8	13.8	14.8	14.8
C	16.1	15.3	16	16	16.1	15.3	16	16.1	15.9

Average Resistivity: 15.5
Geometry Correction Conversion Factor: 1.95
Surface Resistivity: 7.9
Penetrability Based on Test: High

Figure 7-8: Electric Resistivity of sample C-22

Test Description

Title: C-28
Date: 2016-11-25 - 14:32:10 PM
Test Method: ASTM WK378980
Operator: ZQL
Source of Cylinder: C-28
Description:

Displayed Resistivity: kOhm.cm
Electrode Spacing: 3.8 cm - 1.5 inch
Cylinder Size: Cylinder 100 mm x 200 mm

Sample	CH 1 0 deg.	CH 2 90 deg.	CH 3 180 deg.	CH 4 270 deg.	CH 1 0 deg.	CH 2 90 deg.	CH 3 180 deg.	CH 4 270 deg.	Average
A	17.9	16.2	16.5	16.4	17.9	16.2	16.5	16.4	16.8
B	16.2	17.1	16.7	17.2	16.2	17	16.8	17.2	16.8
C	15.9	17.2	15.8	16.2	15.9	17.2	15.8	16.2	16.3

Average Resistivity: 16.6
Geometry Correction Conversion Factor: 1.95
Surface Resistivity: 8.5
Penetrability Based on Test: High

Figure 7-9: Electric Resistivity of sample C-28

Test Description

Title: C-29

Date: 2016-11-23 - 09:08:43 AM

Test Method: ASTM WK378980

Operator: BDM

Source of Cylinder: C-29

Description:

Displayed Resistivity: kOhm.cm

Electrode Spacing: 3.8 cm - 1.5 inch

Cylinder Size: Cylinder 100 mm x 200 mm

Sample	CH 1 0 deg.	CH 2 90 deg.	CH 3 180 deg.	CH 4 270 deg.	CH 1 0 deg.	CH 2 90 deg.	CH 3 180 deg.	CH 4 270 deg.	Average
A	15.2	16.4	16.5	17	15.2	16.4	16.5	16.9	16.3
B	15.4	16.1	15.6	16.8	15.4	16.1	15.7	16.8	16
C	18.3	16.9	17	15.4	18.3	17	17	15.4	16.9
Average Resistivity: 16.4									16.4
Geometry Correction Conversion Factor: 1.95									
Surface Resistivity: 8.4									
Penetrability Based on Test: High									

Figure 7-10: Electric Resistivity of sample C-29

Test Description

Title: C-30

Date: 2016-11-08 - 15:07:40 PM

Test Method: ASTM WK378980

Operator: BDM

Source of Cylinder: C-30

Description:

Displayed Resistivity: kOhm.cm

Electrode Spacing: 3.8 cm - 1.5 inch

Cylinder Size: Cylinder 100 mm x 200 mm

Sample	CH 1 0 deg.	CH 2 90 deg.	CH 3 180 deg.	CH 4 270 deg.	CH 1 0 deg.	CH 2 90 deg.	CH 3 180 deg.	CH 4 270 deg.	Average
A	16.7	17	17	16.3	16.7	17	17	16.3	16.8
B	17.8	18.9	14.2	17	17.7	18.9	14.2	17	17
C	16.2	16.5	17	15.7	16.2	16.5	17	15.7	16.4
Average Resistivity: 16.7									16.73
Geometry Correction Conversion Factor: 1.95									
Surface Resistivity: 8.6									
Penetrability Based on Test: High									

Figure 7-11: Electric Resistivity of sample C-30

Test Description

Title: C-34

Date: 2016-11-25 - 14:40:40 PM

Test Method: ASTM WK378980

Operator:

Source of Cylinder: C-34

Description:

Displayed Resistivity: kOhm.cm

Electrode Spacing: 3.8 cm - 1.5 inch

Cylinder Size: Cylinder 100 mm x 200 mm

Sample	CH 1 0 deg.	CH 2 90 deg.	CH 3 180 deg.	CH 4 270 deg.	CH 1 0 deg.	CH 2 90 deg.	CH 3 180 deg.	CH 4 270 deg.	Average
A	16.5	17.3	15.6	15.2	16.5	17.3	15.7	15.3	16.2
B	15.8	15.9	16	15.3	15.8	15.9	16	15.3	15.8
C	14.7	14.8	15.9	14.7	14.8	14.8	15.9	14.7	15
Average Resistivity: 15.7									15.67
Geometry Correction Conversion Factor: 1.95									
Surface Resistivity: 8.0									
Penetrability Based on Test: High									

Figure 7-12: Electric Resistivity of sample C-34

Test Description

Title: C-35

Date: 2016-11-25 - 14:23:04 PM

Test Method: ASTM WK378980

Operator: ZQL

Source of Cylinder: C-35

Description:

Displayed Resistivity: kOhm.cm

Electrode Spacing: 3.8 cm - 1.5 inch

Cylinder Size: Cylinder 100 mm x 200 mm

Sample	CH 1 0 deg.	CH 2 90 deg.	CH 3 180 deg.	CH 4 270 deg.	CH 1 0 deg.	CH 2 90 deg.	CH 3 180 deg.	CH 4 270 deg.	Average
A	18.6	16.3	15.2	16.5	18.6	16.3	15.3	16.6	16.7
B	17.2	16.6	15	17	17.2	16.6	15	17	16.5
C	15.6	15.8	15.8	17.7	15.6	15.8	15.8	17.7	16.2
Average Resistivity: 16.5									16.47
Geometry Correction Conversion Factor: 1.95									
Surface Resistivity: 8.4									
Penetrability Based on Test: High									

Figure 7-13: Electric Resistivity of sample C-35

Test Description

Title: C-40
Date: 2016-11-08 - 15:21:33 PM
Test Method: ASTM WK378980
Operator: BDM
Source of Cylinder: C-40
Description:

Displayed Resistivity: kOhm.cm
Electrode Spacing: 3.8 cm - 1.5 inch
Cylinder Size: Cylinder 100 mm x 200 mm

Sample	CH 1 0 deg.	CH 2 90 deg.	CH 3 180 deg.	CH 4 270 deg.	CH 1 0 deg.	CH 2 90 deg.	CH 3 180 deg.	CH 4 270 deg.	Average
A	19	20.6	20.1	18.6	19	20.6	20.1	18.6	19.6
B	18.8	18.6	19.1	17.8	18.8	18.6	19.1	17.8	18.6
C	19.1	18.4	18.4	19.2	19.1	18.4	18.4	19.3	18.8
Average Resistivity: 19.0									19.00
Geometry Correction Conversion Factor: 1.95									
Surface Resistivity: 9.7									
Penetrability Based on Test: High									

Figure 7-14: Electric Resistivity of sample C-40:

Test Description

Title: C-42
Date: 2016-11-25 - 14:15:25 PM
Test Method: ASTM WK378980
Operator: ZQL
Source of Cylinder: C-42
Description:

Displayed Resistivity: kOhm.cm
Electrode Spacing: 3.8 cm - 1.5 inch
Cylinder Size: Cylinder 100 mm x 200 mm

Sample	CH 1 0 deg.	CH 2 90 deg.	CH 3 180 deg.	CH 4 270 deg.	CH 1 0 deg.	CH 2 90 deg.	CH 3 180 deg.	CH 4 270 deg.	Average
A	21.5	20.1	20.9	20	21.5	20.1	20.9	20.1	20.6
B	21.4	21.5	20.6	21.1	21.5	21.5	20.6	21.1	21.2
C	20.3	23.3	20.6	21.5	20.4	23	20.6	21.5	21.4
Average Resistivity: 21.1									21.07
Geometry Correction Conversion Factor: 1.95									
Surface Resistivity: 10.8									
Penetrability Based on Test: Moderate									

Figure 7-15: Electric Resistivity of sample C-42

7.2 Disk Sample Figures



Figure 7-16: D-1B



Figure 7-17: D-2B

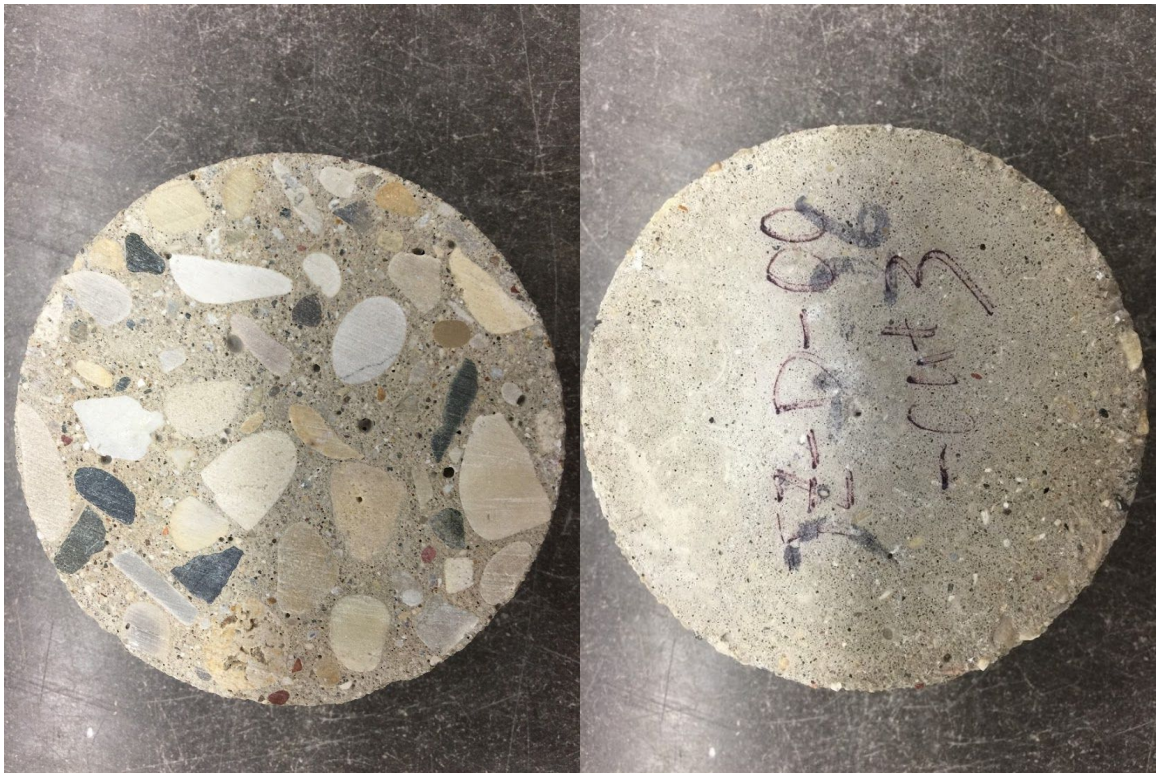


Figure 7-18: D-3B



Figure 7-19: D-4B



Figure 7-20: D-5B



Figure 7-21: D-6B



Figure 7-22: D-7B



Figure 7-23: D-8B



Figure 7-24: D-9B



Figure 7-25: D-1C



Figure 7-26: D-2C



Figure 7-27: D-3C

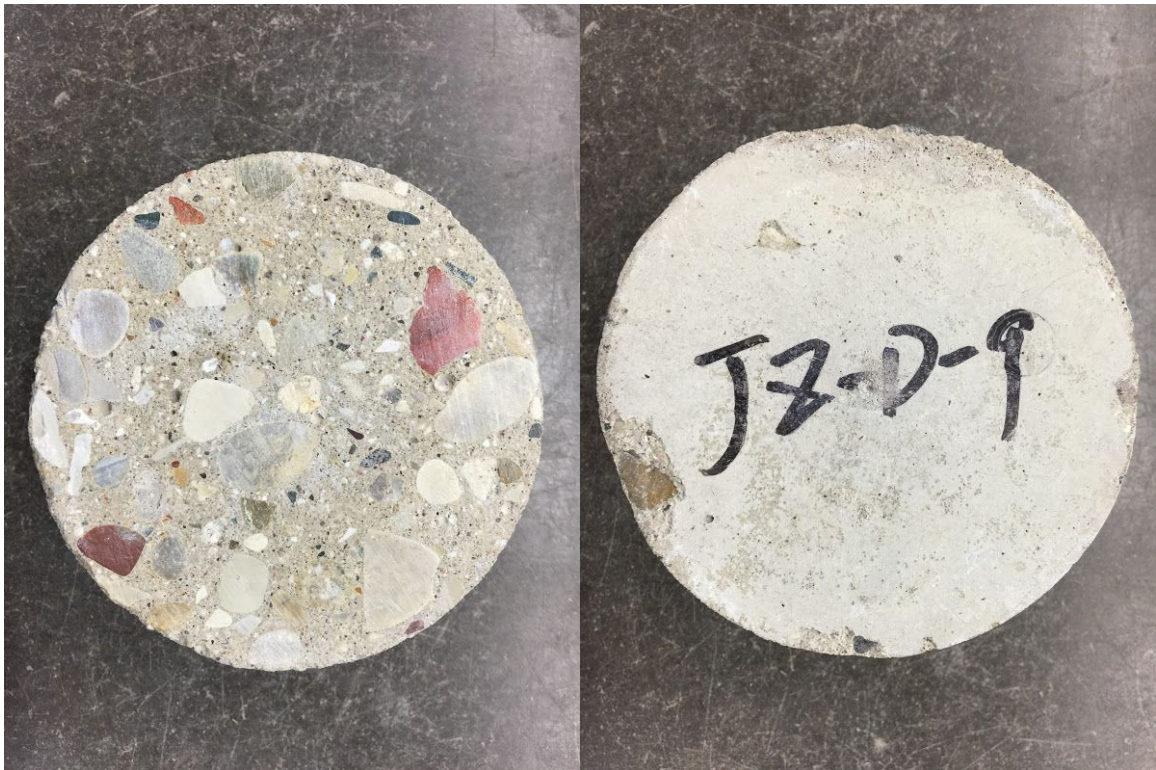


Figure 7-28: D-4C



Figure 7-29: D-5C

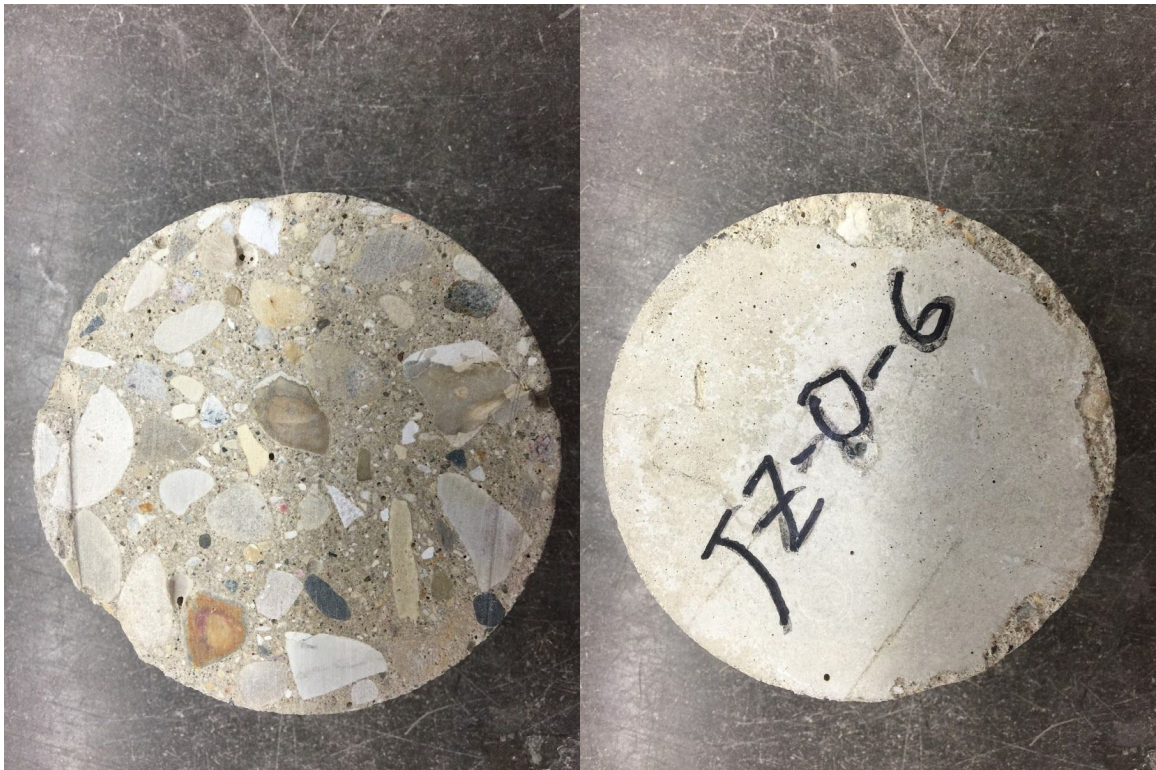


Figure 7-30: D-6C

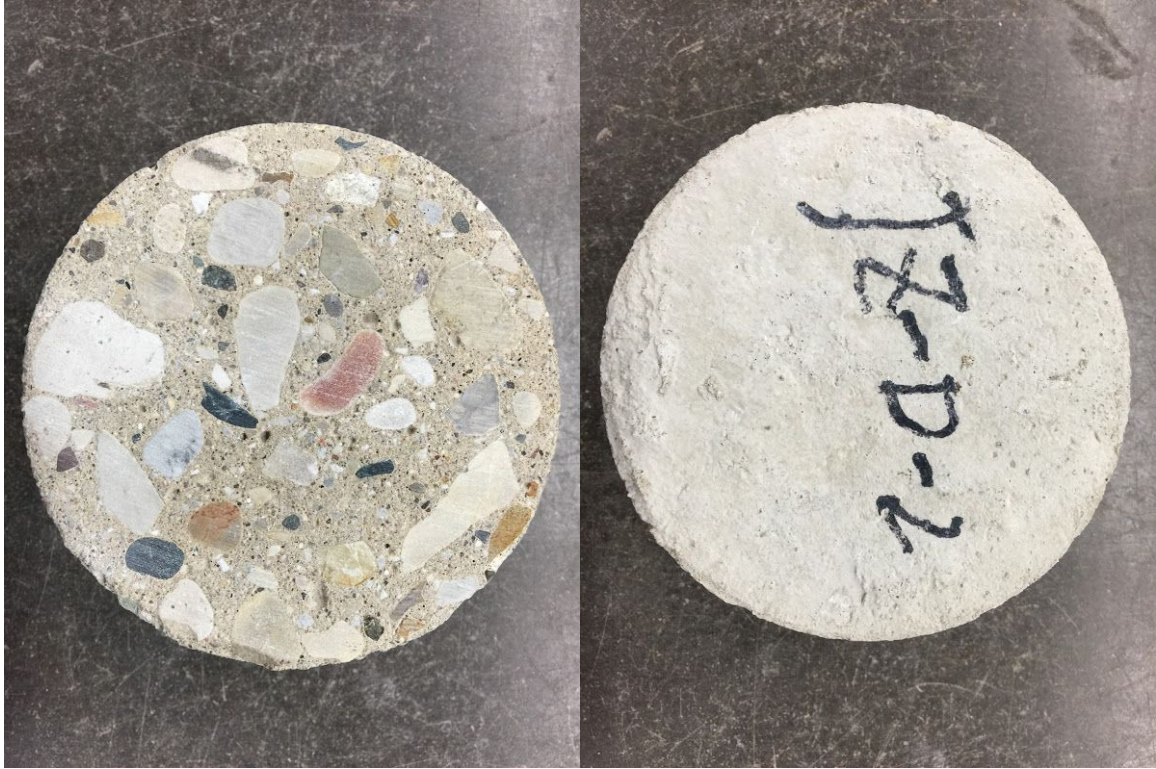


Figure 7-31: D-7C



Figure 7-32: D-8C



Figure 7-33: D-9C



Figure 7-34: D-1D



Figure 7-35: D-2D



Figure 7-36: D-3D



Figure 7-37: D-4D



Figure 7-38: D-5D

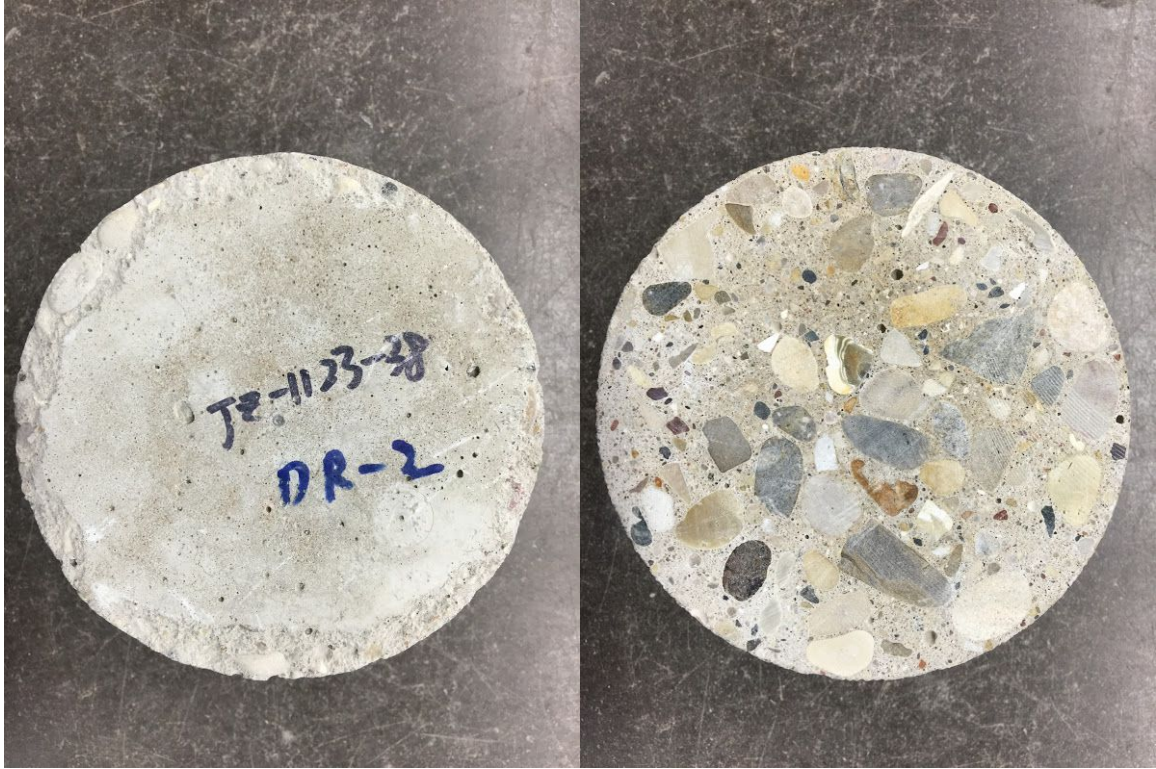


Figure 7-39: D-6D

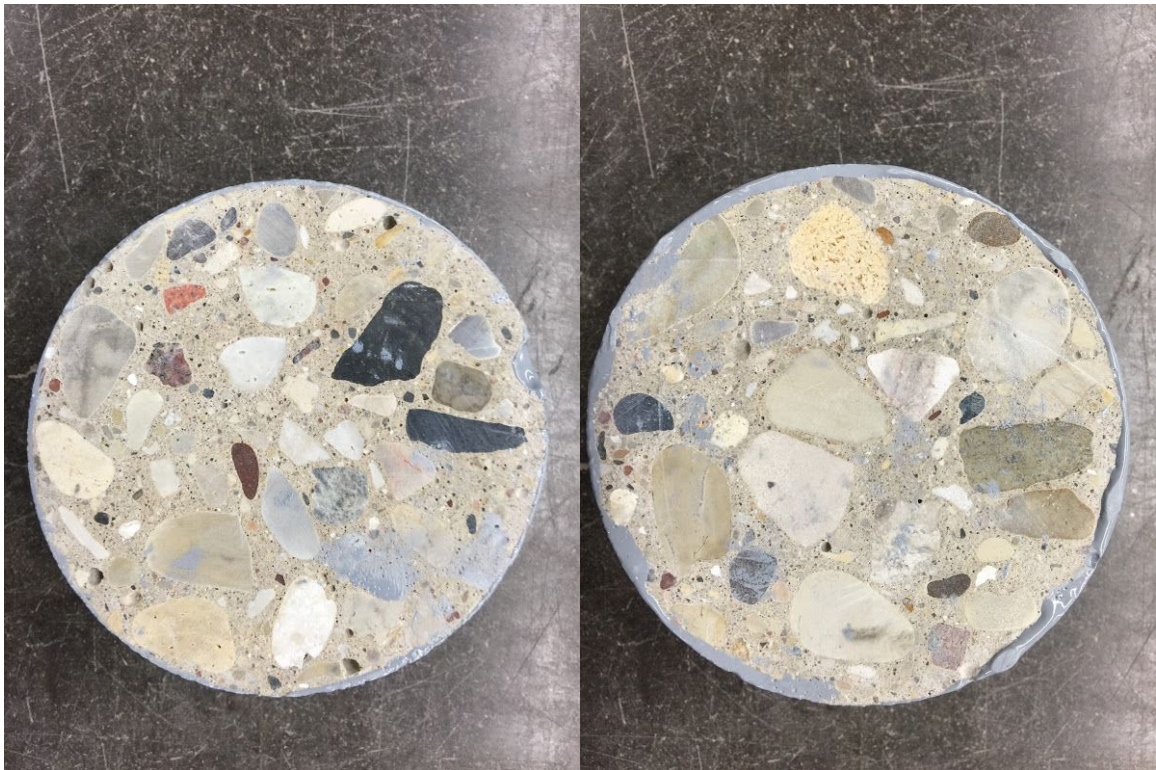


Figure 7-40: D-7D



Figure 7-41: D-8D



Figure 7-42: D-1E



Figure 7-43: D-2E

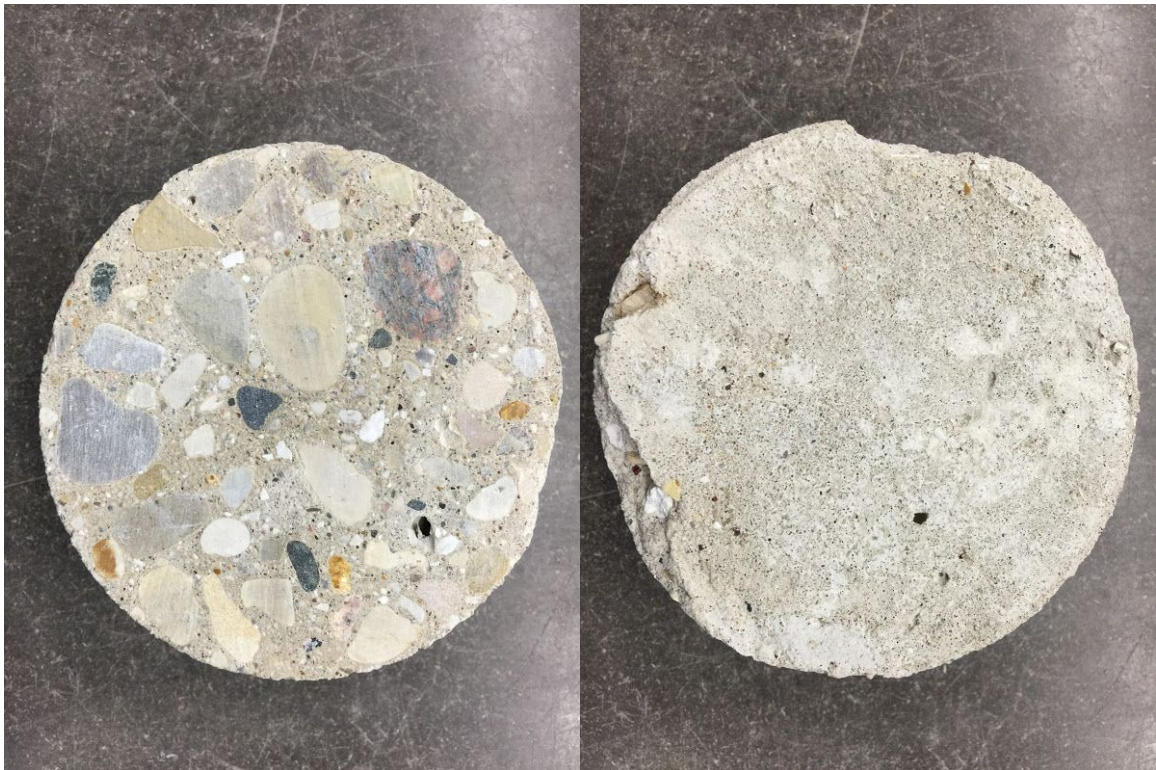


Figure 7-44: D-3E



Figure 7-45: D-4E



Figure 7-46: D-5E



Figure 7-47: D-6E



Figure 7-48: D-7E



Figure 7-49: D-8E

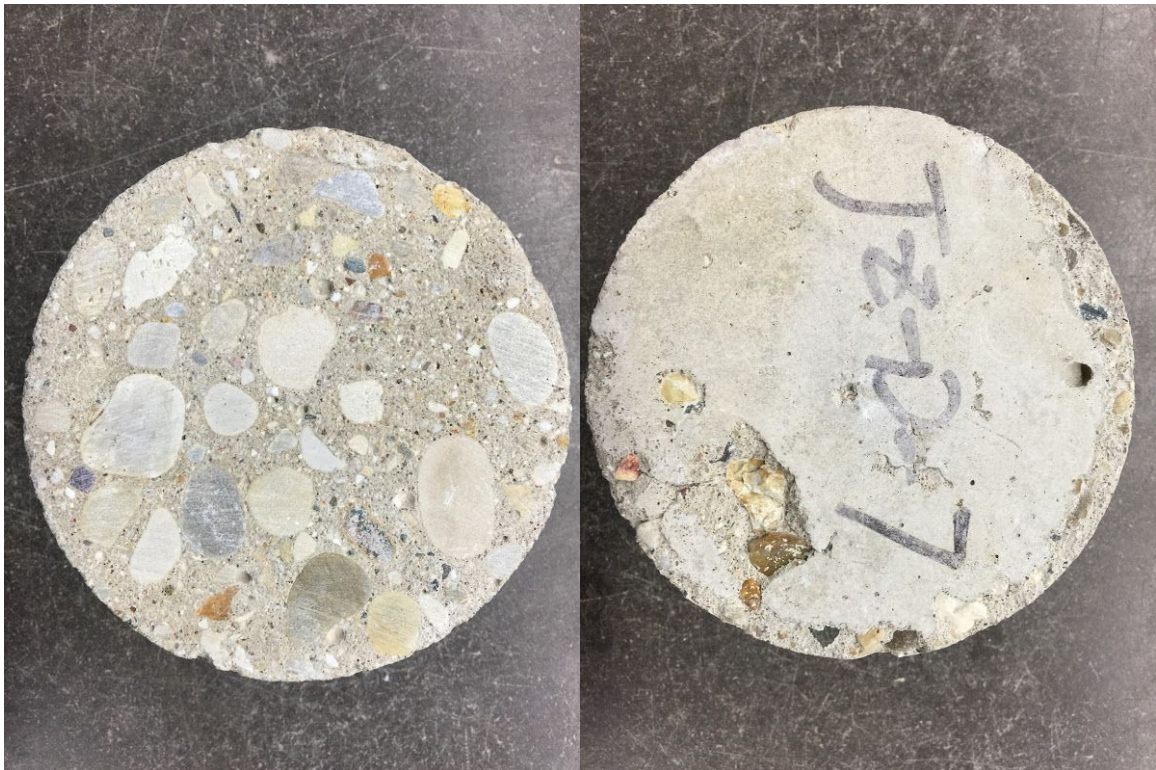


Figure 7-50: D-9E



Figure 7-51: D-1F



Figure 7-52: D-2F



Figure 7-53: D-3F

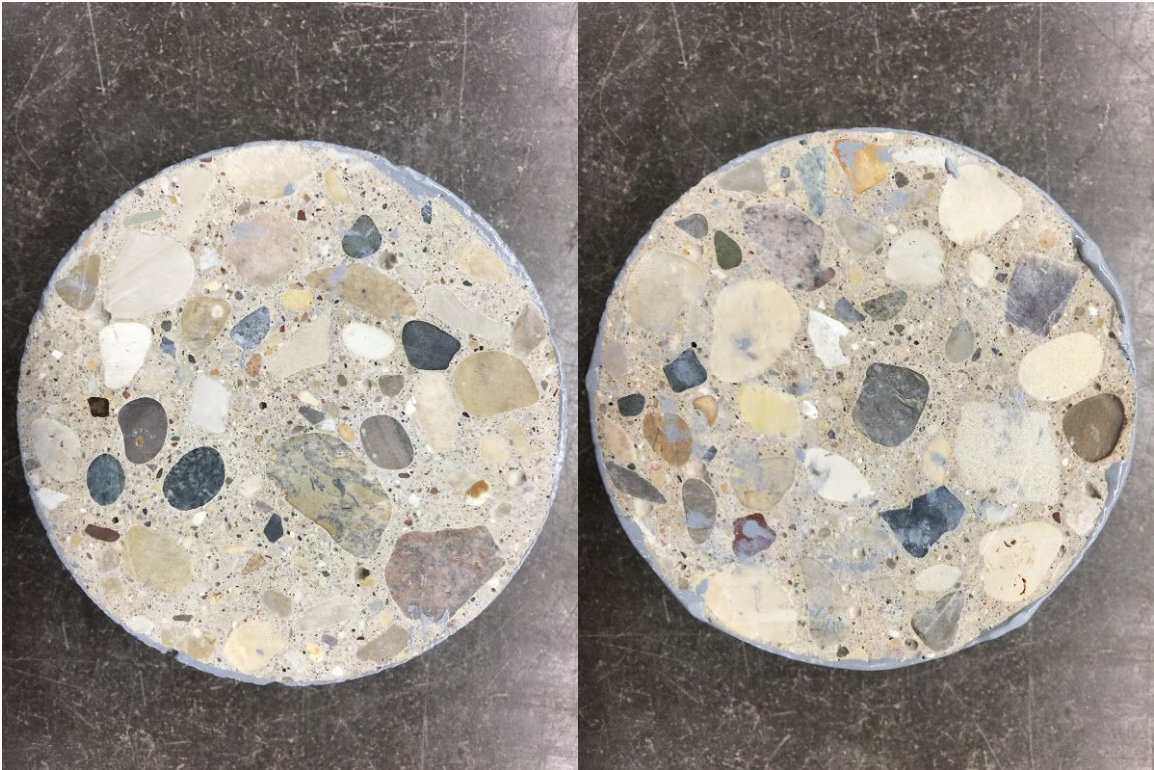


Figure 7-54: D-4F

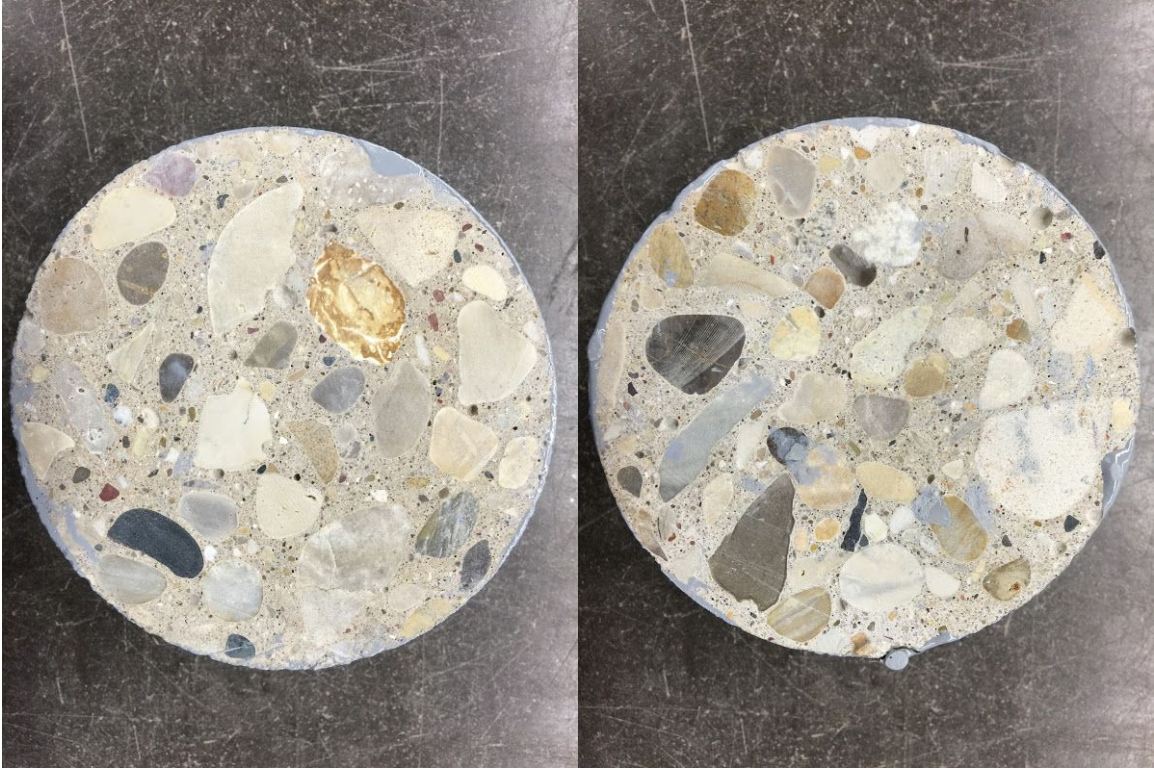


Figure 7-55: D-5F

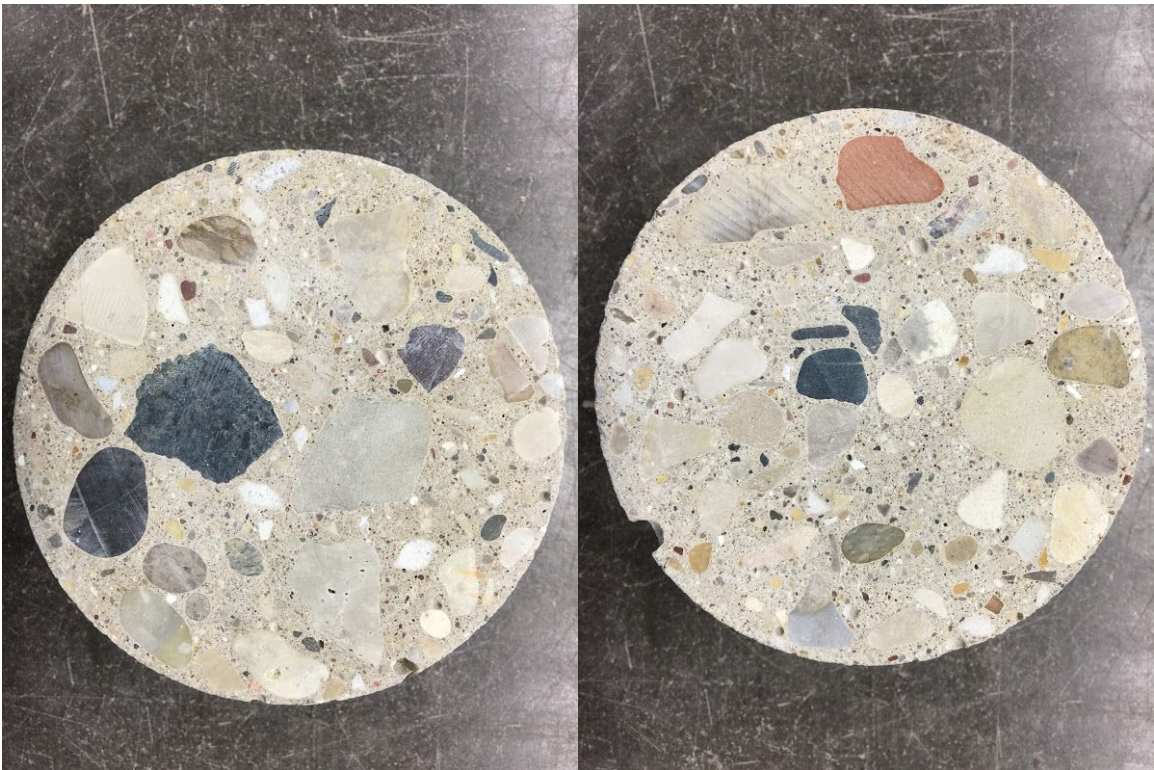


Figure 7-56: D-6F



Figure 7-57: D-7F

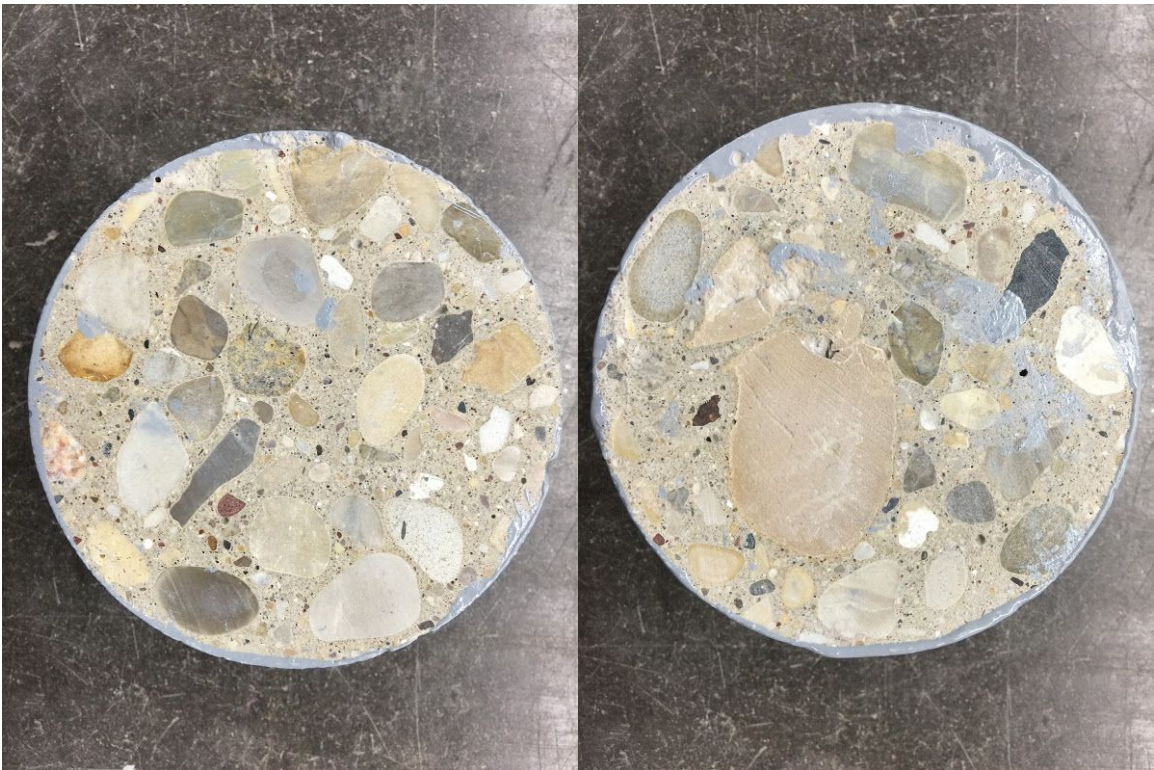


Figure 7-58: D-8F



Figure 7-59: D-9F



Figure 7-60: D-1G



Figure 7-61: D-2G



Figure 7-62: D-4G



Figure 7-63: D-5G



Figure 7-64: D-6G



Figure 7-65: D-7G



Figure 7-66: D-8G



Figure 7-67: D-9G



Figure 7-68: D-1H



Figure 7-69: D-2H

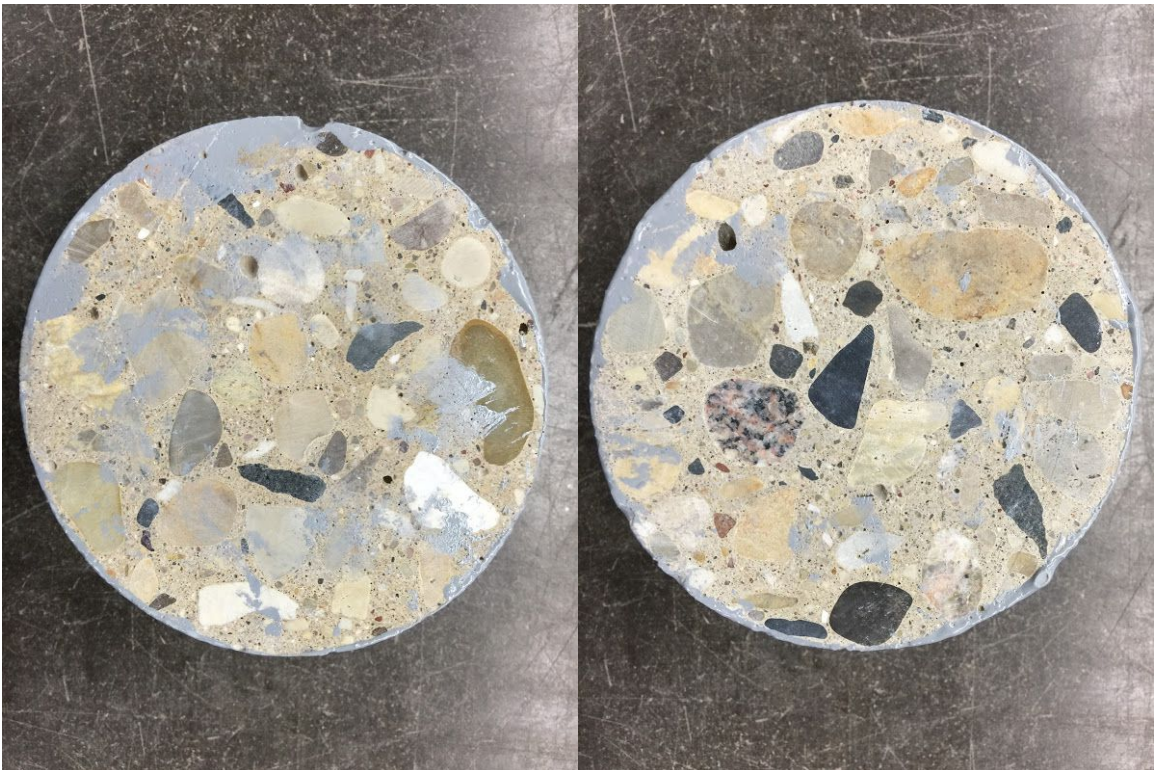


Figure 7-70: D-3H



Figure 7-71: D-4H

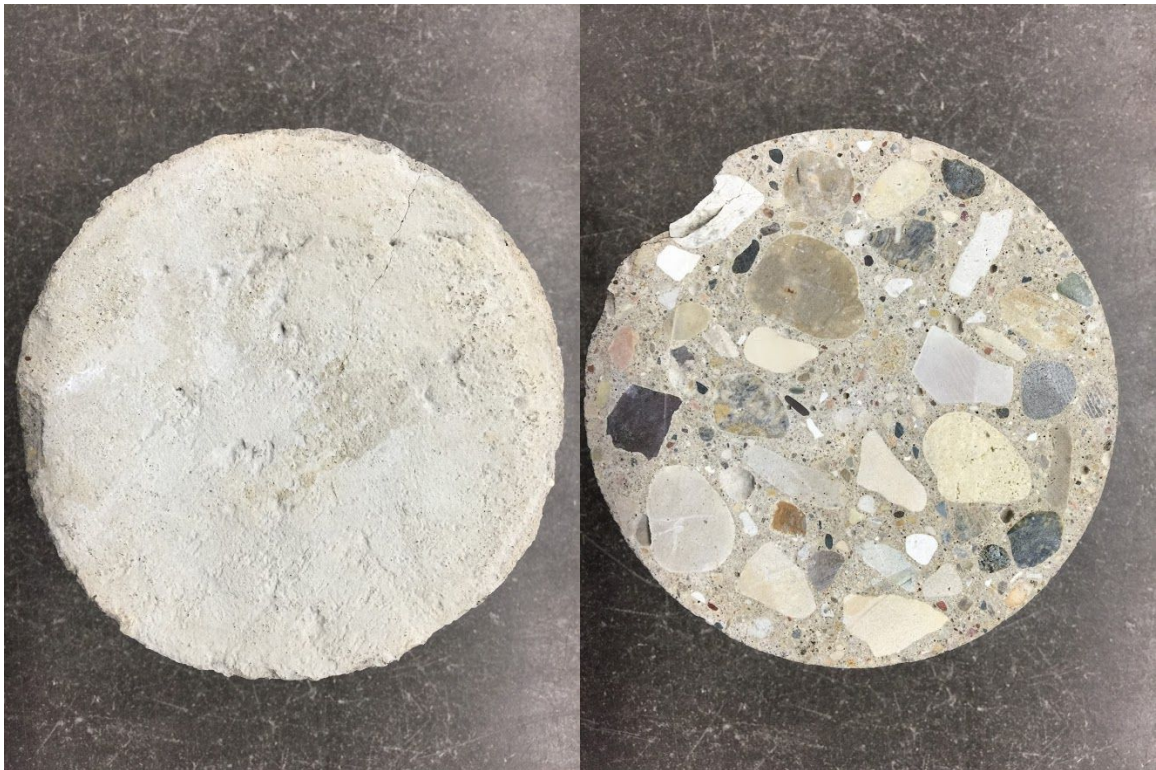


Figure 7-72: D-5H

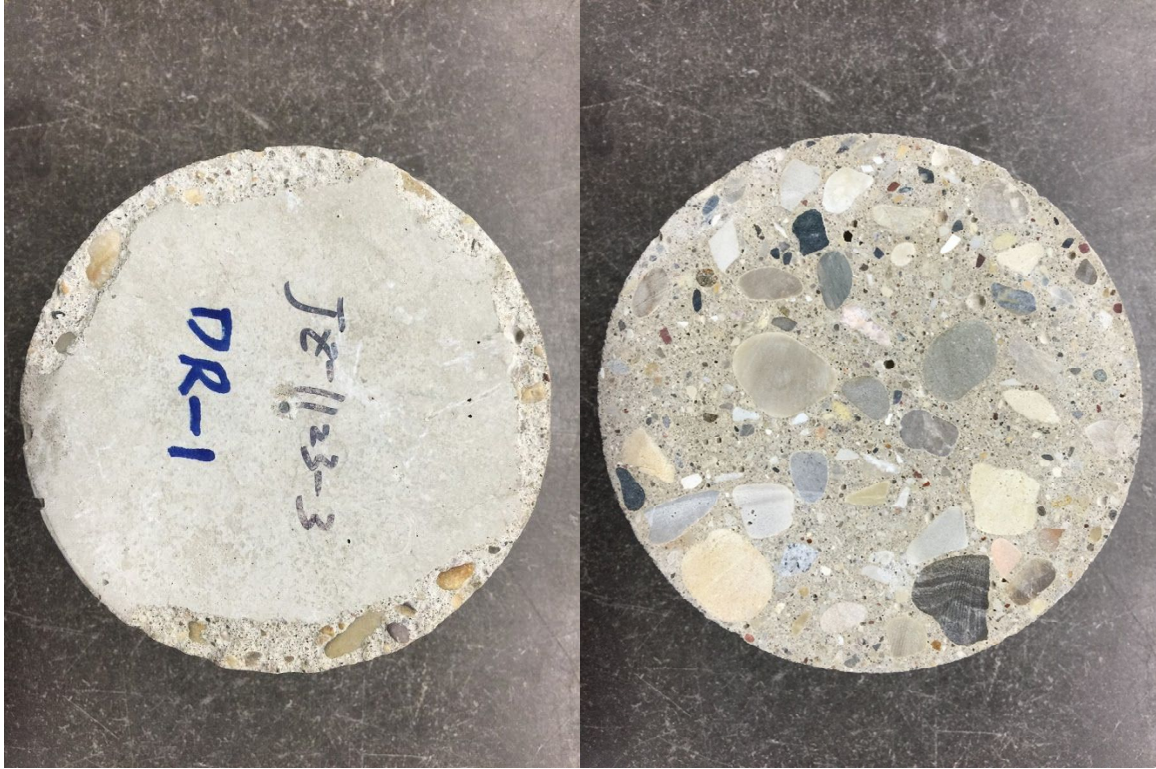


Figure 7-73: D-6H



Figure 7-74: D-7H



Figure 7-75: D-8H

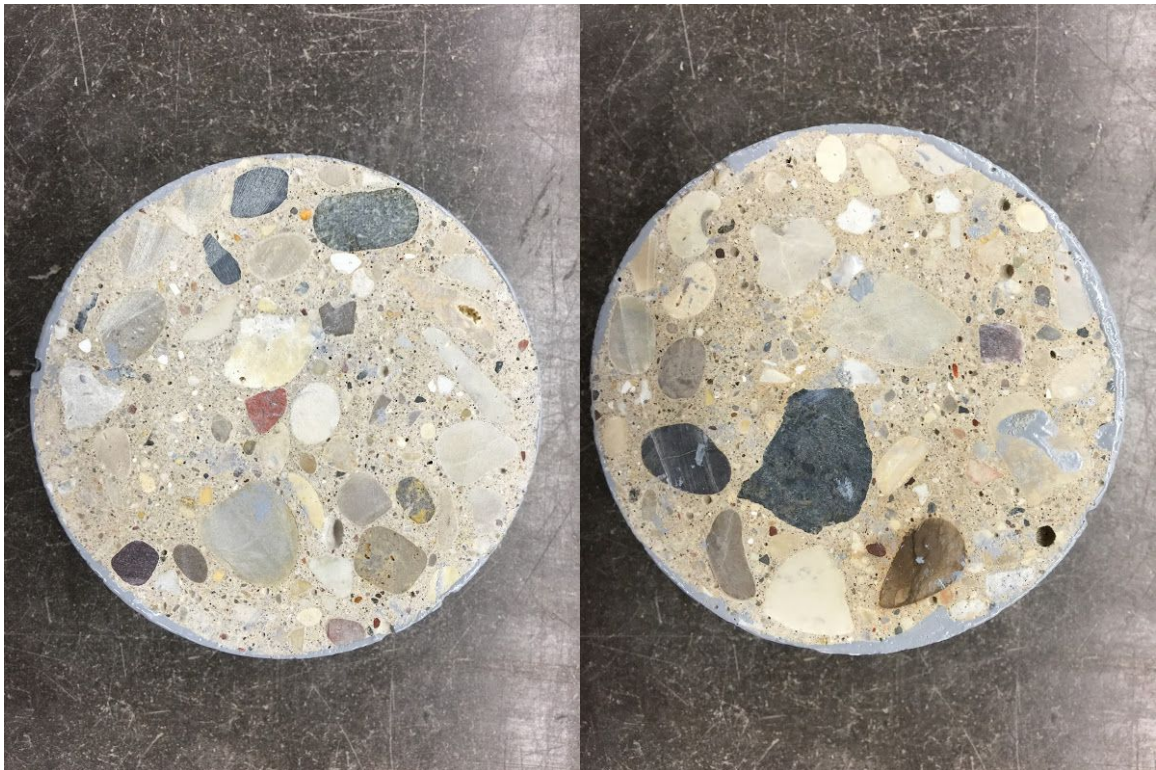


Figure 7-76: D-9H



Figure 7-77: D06-1



Figure 7-78: D06-2

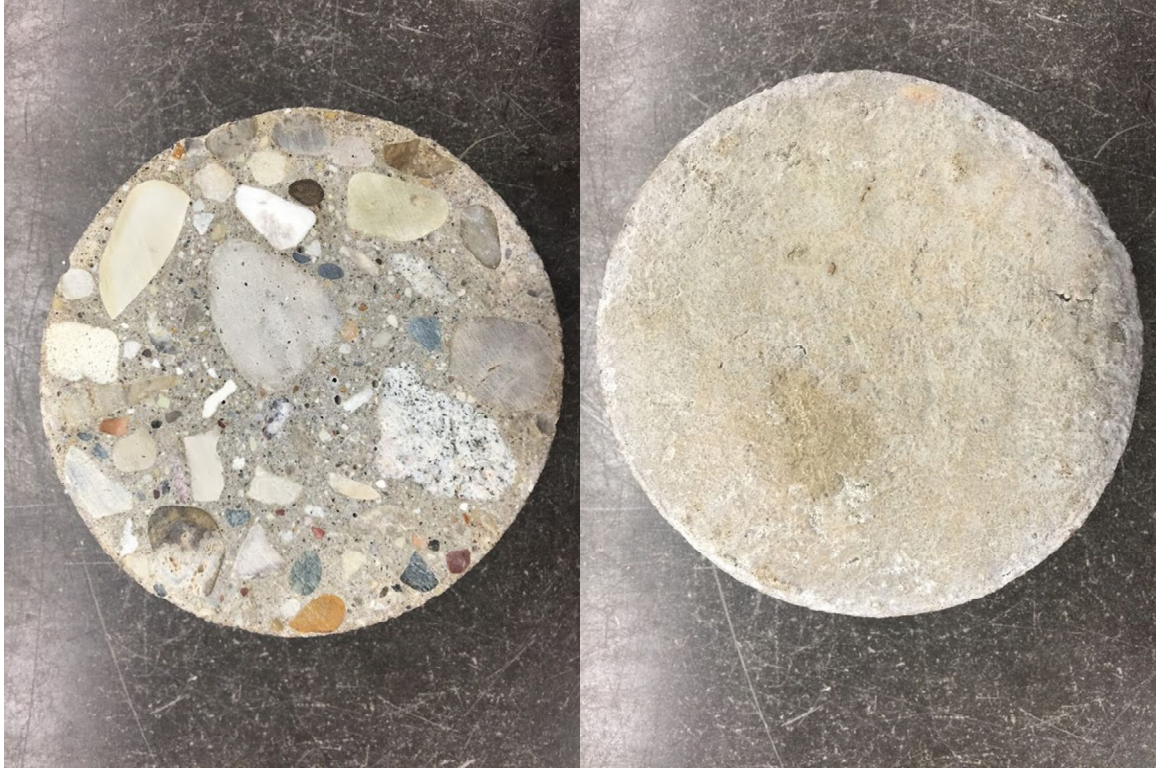


Figure 7-79: D06-3



Figure 7-80: D06-4



Figure 7-81: D11-1

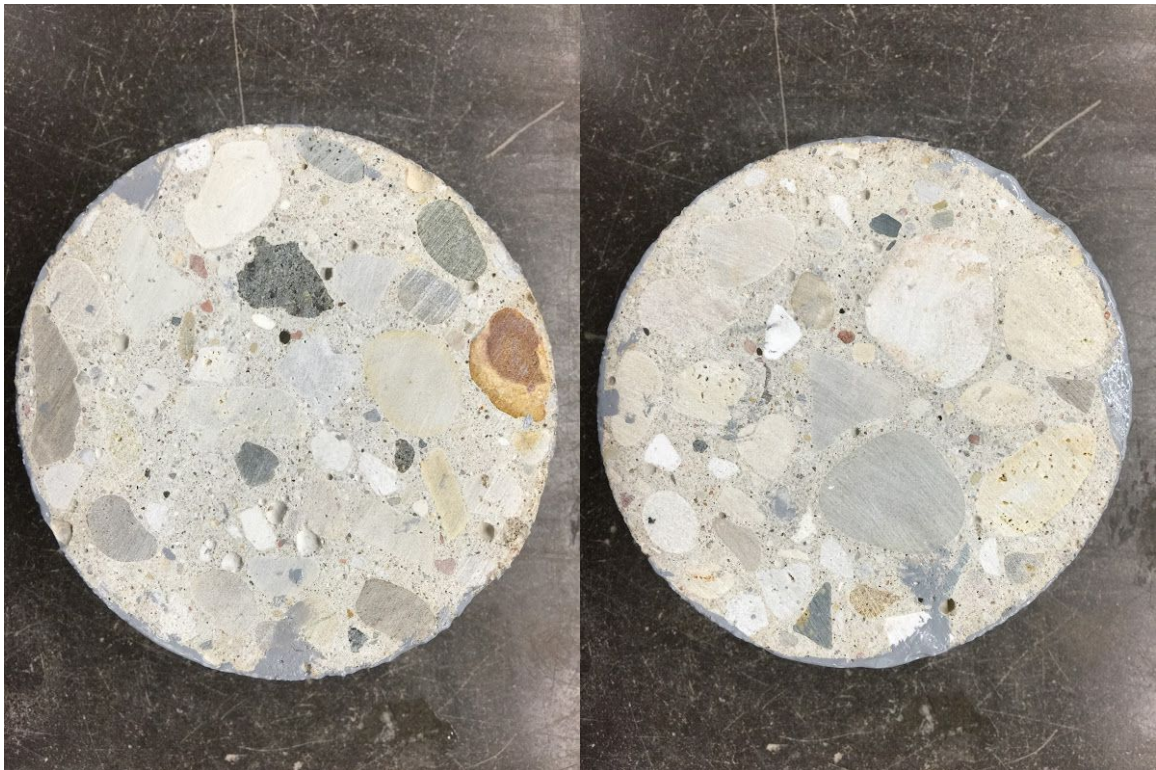


Figure 7-82: D11-2



Figure 7-83: D11-3



Figure 7-84: D11-4



Figure 7-85: D14-1



Figure 7-86: D14-2



Figure 7-87: D14-3



Figure 7-88: D14-4

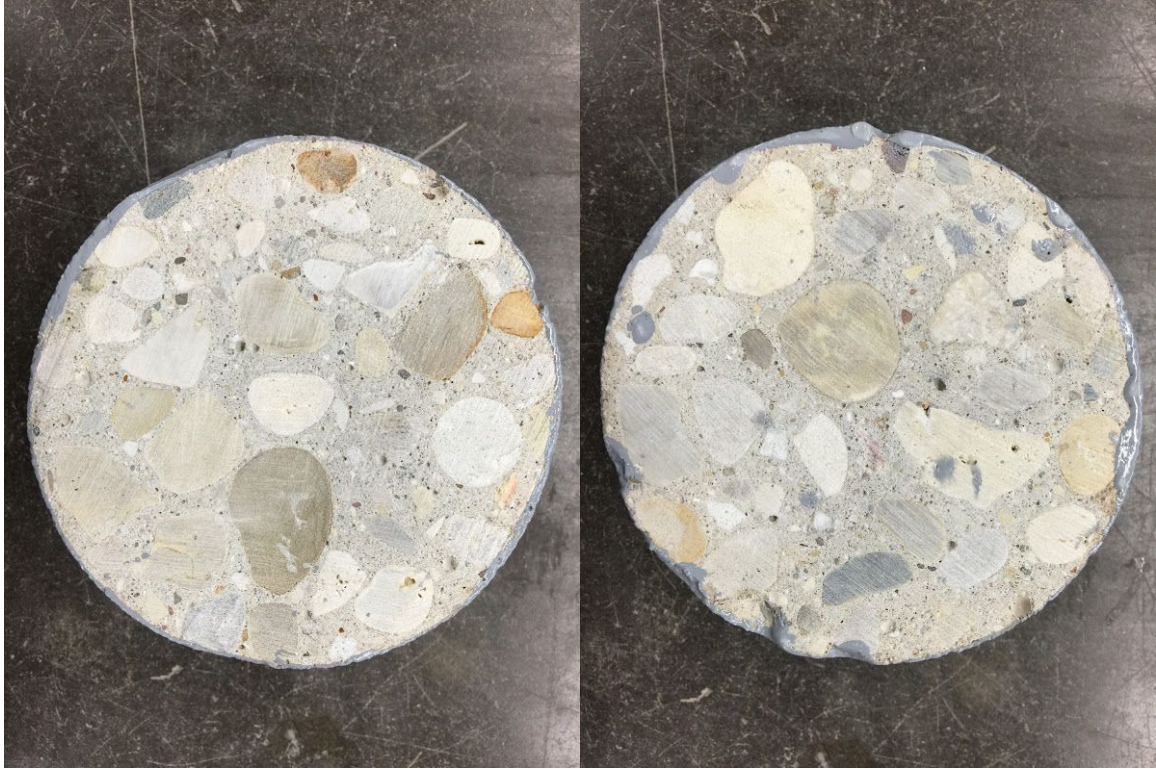


Figure 7-89: D15-1



Figure 7-90: D15-2



Figure 7-91: D15-3



Figure 7-92: D15-4

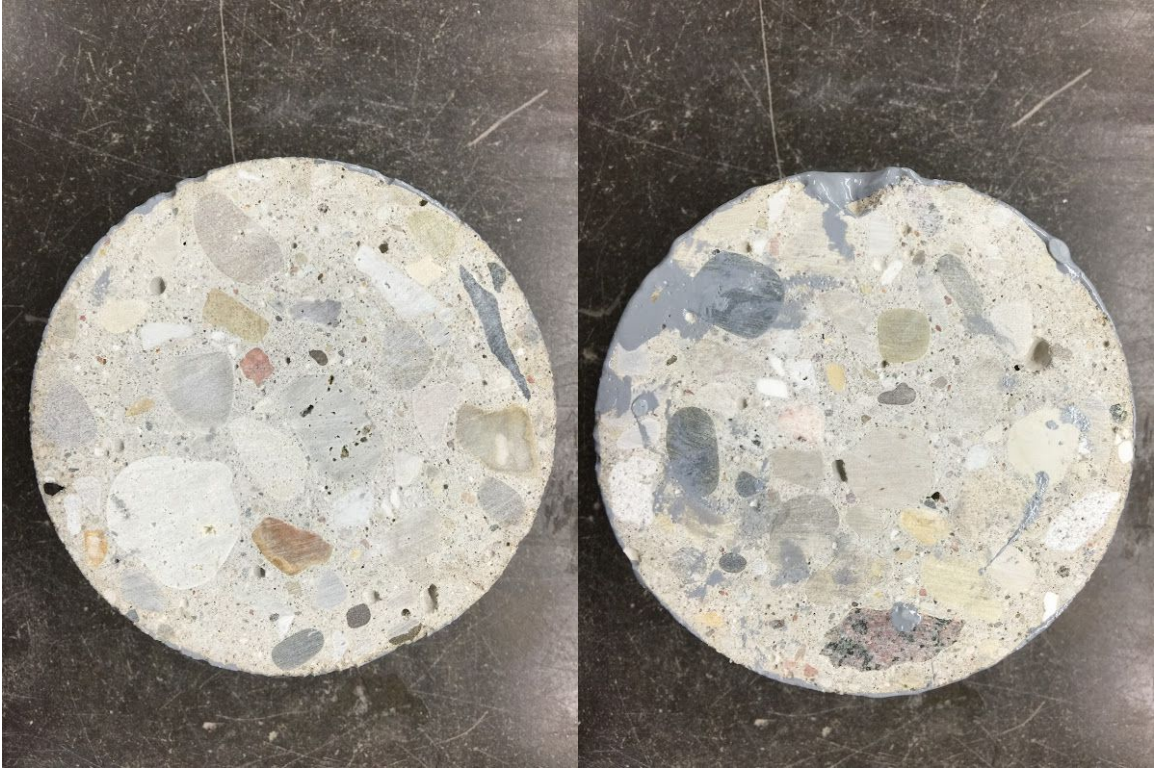


Figure 7-93: D16-1



Figure 7-94: D16-2



Figure 7-95: D16-3



Figure 7-96: D16-4



Figure 7-97: D17-1



Figure 7-98: D17-2



Figure 7-99: D17-3



Figure 7-100: D17-4



Figure 7-101: D21-1



Figure 7-102: D21-2



Figure 7-103: D21-3



Figure 7-104: D21-4



Figure 7-105: D22-1



Figure 7-106: D22-2



Figure 7-107: D22-3



Figure 7-108: D22-4



Figure 7-109: D28-1



Figure 7-110: D28-2



Figure 7-111: D28-3



Figure 7-112: D28-4



Figure 7-113: D29-1



Figure 7-114: D29-2



Figure 7-115: D29-3



Figure 7-116: D29-4



Figure 7-117: D30-1



Figure 7-118: D30-2



Figure 7-119: D30-3



Figure 7-120: D30-4



Figure 7-121: D34-1



Figure 7-122: D34-2



Figure 7-123: D34-3



Figure 7-124: D35-1



Figure 7-125: D35-2



Figure 7-126: D35-3



Figure 7-127: D35-4



Figure 7-128: D40-1



Figure 7-129: D40-2



Figure 7-130: D40-3



Figure 7-131: D40-4



Figure 7-132: D42-1



Figure 7-133: D42-2



Figure 7-134: D42-3



Figure 7-135: D42-4